Optical Response and Control of Molecular Systems

by
Porscha Louise McRobbie

A dissertation submitted in partial fulfillment
of the requirements for the degree of
Doctor of Philosophy
(Physics)
in The University of Michigan
2010

Doctoral Committee:

Professor Eitan Geva, Co-Chair
Professor Roseanne J. Sension, Co-Chair
Associate Professor Luming Duan
Assistant Professor Kevin J. Kubarych
Assistant Professor Jennifer P. Ogilvie

This work is dedicated to my parents, who taught me to dream big and refuse to give up.

ACKNOWLEDGEMENTS

I would like to acknowledge the help of many individuals whom I have been fortunate enough to know during both my undergraduate and graduate studies. Without them, this thesis would not exist.

I would like to thank my undergraduate mentors at Seattle University: Dr. John Meany for his sense of humor and for being the first to nudge me toward graduate studies; Dr. David Boness, for his attempts to explain the precise difference between physical chemistry and chemical physics, and for his generous advice regarding academia and job searches long after I had graduated; and Dr. Michael Morgan who served as my primary undergraduate research advisor, for showing me the beauty of classical mechanics and mathematics, and whose infectious passion for knowledge is unforgettable.

I would like to thank Dr. Jose Alvarez for serving as my surrogate adviser and spending countless hours with me during my first summer of graduate research, and Sung-Kwan Mo for his kindness and cheery disposition, which made our shared office environment quiet and pleasant. I would also like to thank my classmates Kevin Landmark and Damian Khan for keeping it all light while suffering through electrodynamics and condensed matter courses. I would especially like to thank Stephen Reed, who assured me that the world wouldn't crumble if I stopped calculating and ate cookies once in a while, and who became one of my best friends. A special thanks to Anson Cheung, for all of the late night laughs and whose encouragement

and support over the years were much appreciated.

I would like to thank members of the Geva group, past and present, who made the office environment both a colorful and pleasant place to be: Frank Vazquez, Gabriel Hanna, Irina Navrotskaya, and Henry Boateng. I also thank Anne Vazquez for her inspiring teaching insights, and overall positive attitude. Finally, I consider myself unbelievably fortunate to have crossed paths with my thesis adviser, Prof. Eitan Geva. His willingness to offer guidance and advice in matters of research, teaching, and career advancement are truly unparalleled. I will miss the morning espresso tradition, and am grateful for having been taught to argue about phase factors and tensor algebra "Israeli style". I leave his group after five years transformed and inspired both scientifically and personally.

In terms of computing, I am indebted to Todd Raeker and David Braun for their abilities to make computing as painless as possible.

An additional thanks to my fellow Ann Arbor Ashtangis, who have inspired me beyond words both on and off the mat, and who contributed greatly to my overall sanity and peace of mind. Namaste!

And lastly, a special thanks goes to Atsushi Yagi for his endless support at all stages of my graduate tenure. I have learned much from his calm and level-headed approach to both studies and life, and for his patience and kindness toward me I am truly grateful.

TABLE OF CONTENTS

LIST OF FIGURES

Figure

LIST OF APPENDICES

Appendix

ABSTRACT

This thesis is comprised of three major parts and is concerned with the theoretical characterization of condensed phase systems within the framework of nonlinear spectroscopy experiments, using both analytical models and numerical approximation schemes.

The first part focuses on the chirped-pulse mediated coherent control of electronic population transfer, and investigates the plausibility of control in the presence of pure electronic dephasing. The molecular system is described by a *same-frequency* shifted harmonic oscillator model, and population transfer was computed using split-operator and direct diagonalization schemes. Dephasing effects were incorporated using a stochastic model that is able to interpolate between the homogeneous and inhomogeneous limits, and results with and without dephasing were compared as functions of the linear chirp parameter and the field intensity. The numerical findings were compared to and found to be consistent with several experimental studies performed on the laser dye LD690 in liquid methanol.

The second part is a comparative study of several approximation methods used for computing optical response functions, and is illustrated within the context of two-dimensional electronic spectroscopy. A central theme is the development of a benchmark model that can discriminate between different methods, and consists of a *different-frequency* shifted harmonic oscillator model. Optical response spectra were computed using four different approximation schemes, which include two dis-

tinctly different second-order cumulant approximations, a Linearized Semiclassical method, and a Forward-Backward Semiclassical method. Comparing the spectra as a function of temperature and the oscillator frequency ratio assessed the accuracy and robustness of the methods.

The final part concerned a method for computing *ab initio* optical response tensors in the context of two-dimensional infrared spectroscopy, and was a collaborative effort between the Geva and Kubarych groups. An excitonic Hamiltonian was used to model the photo-active modes of a vibrational system, and a direct diagonalization procedure, which utilized inputs from electronic structure calculations, was used to compute the spectra. Preliminary results for the four-mode system $Mn(CO)_5$ are presented, and the methodology developed here was later continued and extended by other members of the collaboration.

CHAPTER I

Prologue

1.1 Introduction

A general way to learn about molecular systems is through their interactions with light. In this thesis, the type of information we hope to extract about the molecular system is divided into two broad classes, depending on whether the electromagnetic field plays a passive or an active role. Here, "passive" describes the case where the light is *not* intended to influence the dynamics nor the response of the system in a direct manner, whereas "active" refers to the deliberate use of light to manipulate the dynamics of the system. A useful way of illustrating these concepts is in the context of nonlinear molecular spectroscopy, since it provides the framework for the studies presented here.

Nonlinear spectroscopy is based on multiple interactions between induced molecular electric dipole moments with the electric field component of the impinging radiation fields, and experimental advances in ultrafast tunable laser sources have made it possible to conduct measurements using carefully timed and tuned laser pulses. In this context, a simple example of the active use of light is a so-called coherent control experiment where a chemical reaction is steered into a pre-selected product channel through the precise control of the time delay between two pulses. A simple

example of the passive use of light is a standard absorption measurement, where a first pulse serves to excite the molecular system which subsequently freely evolves for some time, and then a second pulse is used to probe the resulting final state.

It should be noted, however, that any theoretical descriptions of quantum dynamical systems in condensed phase environments are especially challenging compared with their gas phase counterparts, since they necessarily involve large numbers of different degrees of freedom (DOF), ranging from electronic to local and collective nuclear degrees of freedom. Since the system is constantly interacting with a local environment that changes with time, the transition frequencies of the molecule fluctuate in time. These fluctuations will inevitably influence both the control and response of a molecular system, and must be accounted for to some degree. To treat the system plus its environment fully quantum mechanically is prohibitively expensive due to the exponential scaling with the number of DOF. A common theoretical approach is to separate the degrees of freedom (DOF) into both system and bath contributions, where the influence of the bath is considered to be a source of relaxation in the dynamics of the system DOF. One way to account for the effect of the bath is to perform a statistical averaging process over the bath DOF, which results in a reduced dynamical description of the system. This is the approach taken in this work, to various levels of sophistication.

1.1.1 Coherent Control

The earliest quantum control ideas began with the advent of the laser in the 1960's, when it was considered an ideal tool for controlling chemical reactions. It was thought that by tuning a monochromatic light source to match the local mode frequency of a specific bond, that selective bond cleavage would be possible [1]. Experimentally, however, this goal remained out of reach due to the very rapid

redistribution of intramolecular energy [2]. As laser technologies improved, new types of control schemes based on using the coherence properties of light to manipulate wave function interferences became possible. Such schemes are known as *coherent control*.

In the 1980's, two key coherent control paradigms emerged, one in the frequency domain and another in the time domain [3, 4]. The frequency domain approach, proposed by theoreticians Brumer and Shapiro [5, 6], was based on the principle of quantum interference between two independent pathways leading to the same final result. In this approach, the molecule is irradiated simultaneously with two continuous wave laser beams at different wavelengths. It was found that constructive and destructive interferences of the wave function could be selectively controlled by varying the relative phase of the two beams. Another scenario, formulated in the time domain and proposed by Tannor, Kosloff and Rice [7], was based on optimizing the time delay between two sequential femtosecond pulses[1]. Assuming the bandwidth of the first (pump) pulse is wide enough to cover multiple vibrational states, it creates a vibrational wave packet on the excited state potential energy surface. Since the wavepacket formed on the excited surface is not an eigenfunction of the Hamiltonian for that surface, it propagates in time. At a carefully chosen later time the second (dump) pulse returns the wave packet to a different region on the ground state surface [8].

Both of the above control schemes are based on the optimization of a limited number of parameters, the phase difference between the lasers in the former and the time delay between the pulses in the latter, and were reasonably successful for small molecules in the gas phase [9–12]. However, for the study of complex systems,

[1]The Tannor-Kosloff-Rice scheme is general enough to accommodate multiple pulses. The discussion is restricted to two pulses and a single time delay for clarity.

such as those with many coupled degrees of freedom and in the condensed phase, the relative phases and time delays described above become insufficient as control parameters [1]. A more general type of control became possible with the seminal work of Judson and Rabitz [13], who proposed an optimal control theory [8, 14, 15], that the laser pulse itself should be treated as a parameter and tailored temporally and spectrally to each problem [16]. The algorithm, known as a closed-loop genetic algorithm (GA) [17], forms an ultrashort pulse, uses experimental data as feedback, and iteratively improves the applied field to find the optimal solution given the experimental constraints. An advantage of this method, when compared with theory-based field-design methods that calculate the quantum dynamics as part of the optimization scheme [8, 18, 19], is that knowledge of the full molecular Hamiltonian is no longer required. Instead, the apparatus works as an input-output device capable of measuring directly the action of the field upon the sample [13]. While the use of GAs proved a substantial advancement in coherent control, a disadvantage is that they do not necessarily lead to an understanding of the underlying physics [20].

As pulse-shaping technologies continued to improve with the introduction of devices such as acousto-optical [21] and liquid crystal modulators [22], the field of coherent control was further enhanced by combining shaped pulses with closed-loop GA methods, especially for studies carried out in the condensed phase [4]. The theoretical analysis of such condensed phase experiments is substantially more difficult compared with gas phase experiments, since solution phase experiments are strongly influenced by relaxation processes whereas gas phase dynamics can usually be treated within a relaxation-free framework [23]. The dephasing present in the condensed phase reflects the system's interaction with the surrounding solvent, and it disrupts the coherences that coherent control aims to establish. Thus several the-

oretical studies have focused on analyzing the influence of a solvent on the quantum dynamics of a solute, and determining the conditions under which control is possible.

1.1.2 Multidimensional Spectroscopy

Multidimensional electronic and infrared spectroscopies have been established in recent years as two powerful classes of techniques that are used to study fundamental problems in chemistry, biology and physics. This is largely due to the fact that they possess resolution features that are impossible to achieve with linear spectra [24–27]. More specifically, by correlating electronic or vibrational transition dipoles in two- or three-dimensions, features that would have been congested in the linear spectrum often manifest themselves as off-diagonal peaks which are related to the underlying molecular interaction mechanisms [28–31]. These methods are capable of providing information on molecular structure and dynamics, electronic and vibrational couplings, and energy transfer, and have been applied to a wide range of problems including protein structure and folding, vibrational solvation and relaxation dynamics, energy transfer in photosynthetic proteins, and carrier dynamics in semiconductors [31–35].

The most common applications of multidimensional infrared and electronic spectroscopies are the two-dimensional versions, referred to as 2DIR and 2DE, respectively. Although the interpretation of the 2D spectra is problem specific, the two techniques have many features in common such as using nearly identical sequences of femtosecond pulses and transforming the collected data in the same way [24]. However, there are significant differences in the implementation schemes of the 2DIR and 2DE versions, since achieving the required phase stability of visible lasers is much more difficult than that of infrared lasers [36–38].

The basic pulse sequence for a 2D experiment is shown in Figure 1.1, where

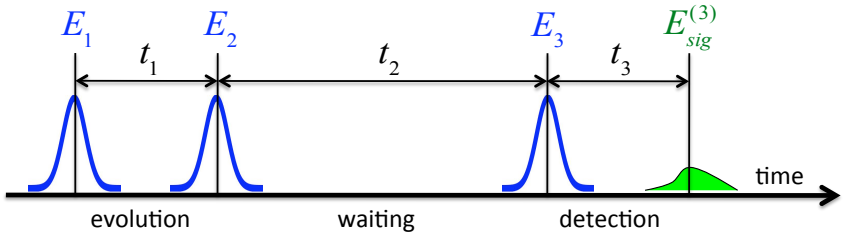

Figure 1.1: A 2D experiment with pulse sequence E_1, E_2 and E_3, which stimulates the emission of the third-order signal field $E^{(3)}_{sig}$. The signal is a function of three time delays, (t_1, t_2, t_3), where t_1 is the time delay between the first and second pulses (evolution), t_2 is the delay between the second and third pulses (evolution), and t_3 is the time delay between the third pulse and detection.

(E_1, E_2, E_3) are the three incident fields, with associated wave vectors $(\mathbf{k}_1, \mathbf{k}_2, \mathbf{k}_3)$ and time delays (t_1, t_2, t_3). The sequence of pulses stimulates the emission of a third-order signal field $E^{(3)}_{sig}$, which is detected in the background-free rephasing and non-rephasing directions defined by $\mathbf{k}_r = -\mathbf{k_1} + \mathbf{k_2} + \mathbf{k_3}$ and $\mathbf{k}_{nr} = \mathbf{k_1} - \mathbf{k_2} + \mathbf{k_3}$. If heterodyne detected by a fully characterized local oscillator field, the amplitude and phase of the signal can be reconstructed [39]. Then, Fourier transforming with respect to t_1 and t_3 produces the frequency axes ω_1 and ω_3 of the 2D spectrum (i.e., frequency correlation map), respectively, which may be studied as a function of the waiting time t_2. The diagonal peaks in the spectrum ($|\omega_1| = \omega_3$) resemble the linear absorption, while the off-diagonal peaks ($|\omega_1| \neq \omega_3$) generally reveal couplings between different transitions [27, 40].

1.2 Model Systems

To model a molecular system subjected to excitation by a laser field, we consider an overall Hamiltonian of the general form

$$\hat{H} = \hat{H}_M + \hat{H}_{int} \tag{1.1}$$

where $\hat{H}_M$ is the molecular (field-free) Hamiltonian and $\hat{H}_{int}$ is a light-matter interaction term. The system and radiation field are assumed to interact through a dipole

coupling of the form

$$\hat{H}_{int} = -\overrightarrow{\hat{\mu}}(\hat{\mathbf{Q}}) \cdot \overrightarrow{\mathcal{E}}(t), \tag{1.2}$$

where $\overrightarrow{\hat{\mu}}$ is the induced transition dipole moment, $\hat{\mathbf{Q}}$ is the set of nuclear coordinates, and $\overrightarrow{\mathcal{E}}(t)$ is the classical electric field. The form of the molecular Hamiltonian $\hat{H}_M$ is application specific, and will be discussed in terms of electronic and vibrational spectroscopies in §1.2.1 and §1.2.2, respectively.

1.2.1 Two-State Model for Electronic Spectroscopy

For the electronic spectroscopy applications presented in chapter 2 and chapter 3, we focus on a single transition between two electronic states, $\{|g\rangle, |e\rangle\}$, where g and e denote the ground and first excited states, respectively, and each is coupled to a corresponding nuclear motion $\hat{H}_{g/e}$. Due to the fact that the nuclei are nearly three orders of magnitude heavier than the electrons, we make the usual Born-Oppenheimer assumption that electronic excitation occurs on a timescale that is rapid enough to exclude any substantial rearrangement in the nuclear geometry [41]. These considerations lead to the following molecular (field-free) Hamiltonian

$$\hat{H}_M = \hat{H}_g |g\rangle \langle g| + \left(\hat{H}_e + \hbar\omega_{eg}^0\right) |e\rangle \langle e|. \tag{1.3}$$

Here, $\hat{H}_{g/e} = T(\hat{\mathbf{P}}) + V_{g/e}(\hat{\mathbf{Q}})$ are the adiabatic Hamiltonians, where $T(\hat{\mathbf{P}})$ is the kinetic energy, $V_{g/e}(\hat{\mathbf{Q}})$ is the Born-Oppenheimer potential surface corresponding to electronic configuration g/e, $\{\hat{\mathbf{Q}}, \hat{\mathbf{P}}\}$ are the set of nuclear coordinates and momenta, and $\hbar\omega_{eg}^0$ is the $0 \rightarrow 0$ transition frequency between the lowest vibrational level on the ground electronic potential and that of the excited electronic potential (see Figure 1.2). It should be noted that (1.3) only accounts for laser-induced couplings between the potentials. i.e., all non-adiabatic surface couplings are ignored[2]. This

[2]The inclusion of non-adiabatic couplings is possible by adding additional terms to $\hat{H}_M$, or by choosing an alternative electronic basis [41].

assumption is justified provided population relaxation is slow relative to dephasing, which is often the case in condensed phase systems.

Throughout this work, the following simplifications and assumptions are made regarding the molecular Hamiltonian:

- For the sake of simplicity, this thesis focuses on a system with a single photo-inactive DOF, whose coordinate and momentum operators are given by $\hat{Q}$ and $\hat{P}$ respectively[3].
- The electronic configuration has no effect on the *shape* of the nuclear potentials, so that electronic excitation results only in a displacement between their minima by an amount Q_d [43, 44]. By further assuming that the nuclear motion is *purely harmonic* with characteristic frequency $\omega_{g/e}$, the Born-Oppenheimer potentials are modeled as quadratic functions of the nuclear coodinate:

$$\begin{aligned} V_g(\hat{Q}) &= \frac{1}{2}m\omega_g^2\hat{Q}^2 \\ V_e(\hat{Q}) &= \frac{1}{2}m\omega_e^2\left(\hat{Q}+Q_d\right)^2 \end{aligned} \tag{1.4}$$

It should be noted that the "bare" transition frequency ω_{eg}^0 in (1.3) is not the same as the vertical transition frequency $\omega_{ver} = \omega_{eg}^0 + \frac{1}{2\hbar}\omega_e^2 Q_d^2$, due to the relative shift between the potential minima.

The transition dipole moment coupling the two electronic states is given by

$$\hat{\mu} = \hat{\mu}_{ge}\left|g\right\rangle\left\langle e\right| + \hat{\mu}_{eg}\left|e\right\rangle\left\langle g\right|, \tag{1.5}$$

and two points should be noted regarding its form:

- The Condon approximation has been made by assuming that the dipole moment is independent of the molecular displacement $\mu(\hat{Q}) \approx \hat{\mu}$.

[3]The extension to the case of multiple photo-inactive DOFs is straightforward[42].

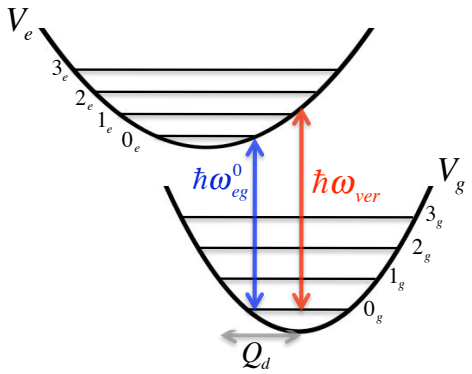

Figure 1.2: Schematic of the two-state model. ω_{eg}^0 and ω_{ver} are the $0-0$ and vertical transition frequencies, respectively. $V_{e/g}$ is the Born-Oppenheimer potential associated with the e/g electronic state, and Q_d is displacement between the minima. Each surface has associated vibrational states labeled by $\{|n, g/e\rangle\}$ for $n = 0, 1, 2, \ldots$.

- $\hat{\mu}$ is a *scalar* since there is only a single electronic transition (which results in optical response *functions* in the context of chapter 3).

It will prove useful in chapters 2 and 3 to express the transition dipole in terms of a vibronic state basis. To this end, we first note that the vibrational (harmonic oscillator) eigenstates $\{j\}$ associated with a given electronic potential $\hat{V}_{g/e}$ obey the following closure and orthogonality conditions

$$\sum_j |j\rangle \langle j| = 1; \;\; \langle j|j'\rangle = \delta_{j,j'} \tag{1.6}$$

and, when inserted into (1.5), leads to

$$\hat{\mu} = \hat{\mu}_{ge} \sum_{gj,ek} |g,j\rangle \langle gj|ek\rangle \langle e,k| + \hat{\mu}_{eg} \sum_{gj,ek} |e,k\rangle \langle ek|gj\rangle \langle g,j| \,. \tag{1.7}$$

The states $\{|\zeta, l\rangle = |\zeta\rangle |l\rangle\}$ $(\zeta = g, e)$ are the vibronic eigenstates of $\hat{H}_{g/e}$ which obey

$$\begin{aligned} \hat{H}_{g/e} |\zeta, l\rangle &= \varepsilon_{\zeta,l} |\zeta, l\rangle \\ \langle \zeta, l|\zeta', l'\rangle &= \delta_{\zeta,\zeta'}\delta_{l,l'} \end{aligned} \tag{1.8}$$

where $\{\varepsilon_{\zeta,l}\}$ are the corresponding vibronic energy levels. Here, the index gj labels vibrational states on the *ground* electronic surface, while the index ek labels vibra-

tional states on the *excited* electronic surface. A similar convention will be used where appropriate in chapters 2 and 3.

Finally, the overlaps $\langle gj|ek\rangle$ are between eigenstates of *different* potentials, so that

$$\langle gj|ek\rangle \equiv S_{gj,ek} \neq 0. \tag{1.9}$$

The $\{S_{gj,ek}\}$ are the Franck-Condon (F-C) factors, where $S_{ek,gj} = S^*_{gj,ek}$. For the same frequency shifted *harmonic* oscillator model considered here, the F-C factors assume a closed-form expression (see Appendix C)[4]

$$S_{j,k} = \frac{1}{\sqrt{j!}}\frac{1}{\sqrt{k!}}\exp\left(-\frac{m\omega}{4\hbar}Q_d^2\right)\left[\sum_{n=0}^{j}\begin{pmatrix} j \\ n \end{pmatrix}\left(-\sqrt{\frac{m\omega}{2\hbar}}Q_d\right)^{j-n}\frac{d^n}{d\lambda^n}\left(\lambda^k\right)\right]_{\lambda=\sqrt{\frac{m\omega}{2\hbar}}Q_d}$$

1.2.2 Multistate Model for Vibrational Spectroscopy

For the vibrational spectroscopy application presented in chapter 4, the system consists of many vibrational states whose energy levels are assumed to be organized into bands as in Figure 4.2. The field-free Hamiltonian for such a system may be characterized by an excitonic Hamiltonian of the form

$$\hat{H}_M = \sum_j \left(\hbar\omega_{10} + \varepsilon_{1j}\right)|1j\rangle\langle 1j| + \sum_k \left(\hbar\omega_{20} + \varepsilon_{2k}\right)|2k\rangle\langle 2k| + \ldots \tag{1.11}$$

where the zero of energy is defined to coincide with the ground state $|00\rangle$ and "..." indicates the third and higher bands above the ground state which are not explicitly shown in the Figure. Here, $\{|1j\rangle\}$ and $\{|2k\rangle\}$ are the first and second band of states, respectively, above the ground state. The ground state "band" consists of only a single, non-degenerate state. The energies $\{\varepsilon_{1j}\}$ and $\{\varepsilon_{2k}\}$ within each band are measured relative to their respective lower band edges (see Figure 1.3), and ω_{10}, ω_{20}

[4]For more complicated potentials, a numerical evaluation of the F-C factors would be required.

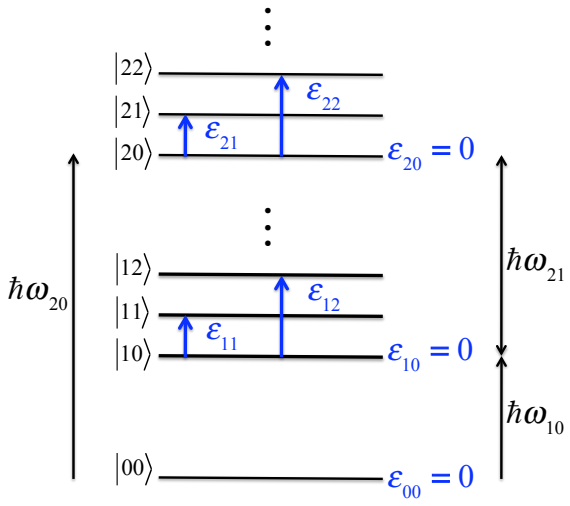

Figure 1.3: Schematic energy level diagram for a multi-state system with eigenstates and energy levels $\{|mj\rangle, \varepsilon_{mj}\}$. The index $m = 0, 1, 2, \ldots$ labels the band, where $m = 0$ corresponds to the ground state, and $j = 0, 1, 2, \ldots$ labels the state within a given band.

and ω_{21} are the transition frequencies between the ground state and those lower band edges.

In contrast to the single electronic transition considered in §1.2.1, there are now multiple vibrational transitions between states within different bands. However, vibrational selection rules restrict the transitions to those between states which differ by a single quantum of energy. This leads to a transition dipole operator of the form

$$\overrightarrow{\mu} = \sum_j \left[\overrightarrow{\mu}_{00,1j} |00\rangle \langle 1j| + \overrightarrow{\mu}_{1j,00} |1j\rangle \langle 00|\right] + \sum_{j,k} \left[\overrightarrow{\mu}_{1j,2k} |1j\rangle \langle 2k| + \overrightarrow{\mu}_{2k,1j} |2k\rangle \langle 1j|\right] + \ldots \tag{1.12}$$

where the indices j and k label states within first and second bands above the ground state, respectively. Thus the first set of terms $\sum_j [\ldots]$ represents transitions between the ground state and the first band of states, while the second set of terms $\sum_{j,k} [\ldots]$ represents transitions between the first and second bands of states.

Two points should be noted regarding the transition dipole operator:

- The Condon approximation in this context amounts to assuming that the $\{\overrightarrow{\mu}_{\alpha i,\beta j}\}$

in (1.12) are constant vectors

- The fact that $\overrightarrow{\mu}$ is a *vector* implies that the multiple allowed transitions have associated directionalities. Consequently, the response of the system requires an optical response *tensor* formalism.

1.3 Overview

This thesis is comprised of three major parts and is concerned with the theoretical characterization of condensed phase systems within the framework of nonlinear spectroscopy experiments, using both analytical models and numerical approximation schemes.

Chapter 2 focuses on assessing the robustness of a coherent control process in the presence of pure electronic dephasing, by examining the role of dephasing under different conditions. The motivation originated with a series of experiments performed by the Sension group on the laser dye molecule LD690 in liquid solution. More specifically, those experiments and others were able to clearly establish that the control of electronic population transfer in LD690 in solution was possible via phase-shaped or "chirped" laser pulses. The efficiency of the transfer was sensitively dependent on both the magnitude and sign of the linear chirp, and also to the pulse intensity. In our theoretical study, the molecular system was described by a two-electronic state model, where each state was coupled to a harmonic potential of the same shape, and the interaction with light was via an electronic dipole interaction. The effects of environmental fluctuations were accounted for by a stochastic model that is able to interpolate between the homogeneous and inhomogenous limits. In the first part of the study, the excited state populations was computed as a function of both the linear chirp parameter and the field intensity without any dephasing. The second

part of the study focused on varying both the amplitude and relaxation rate of the environmental fluctuations, to understand how they affect the transfer efficiency.

Chapter 3 illustrates the development of a benchmark model that can be used to make a systematic comparison of various quantum dynamical approximation schemes. The benchmark model is a two-electronic state model similar to that used in chapter 2, only the electronic states are coupled to harmonic potentials of *different* shapes. The aim was to choose the simplest possible benchmark model for which both an exact solution was known and that could distinguish between the different approximations. Linear and nonlinear response functions in the context of a 2D experiment were computed using four different approximation schemes, and compared as functions of temperature and parameters of the two-state model. The four schemes consisted of two distinctly different second-order cumulant approximations and two semiclassical approximations. The emphasis of this chapter is to assess the accuracy and robustness of the approximations under different conditions, and not on the reproduction of optical spectra for a specific system. Environmental effects were accounted for phenomenologically in the context of Redfield theory in the homogeneous limit, but were not the focus of this study.

Finally, chapter 4 introduces a method for computing the optical response in the context of a 2DIR experiment, where the inputs are obtained from *ab initio* electronic structure calculations. This work was a collaborative effort between the Geva and Kubarych groups, and the specific responsibilities of each member of the collaboration are clearly delineated in §4.1. In this case, the reduced system description is given by an excitonic Hamiltonian which accounts for only a few vibrational modes of interest. In contrast to the previous chapters where there was only a single electronic transition dipole moment, the multistate system considered in this chapter

involves multiple direction-specific transitions and leads to a considerably more complex calculation of the nonlinear response. The ultimate goal was to development the necessary framework needed to study a metal carbonyl compound containing ten coupled CO vibrations. As a first step, the general framework was established and applied to a smaller compound containing five CO groups. Environmental effects were accounted for in the same way as in chapter 3, and were not the focus of this study. The main results presented in this chapter are preliminary in nature, but were foundational to further studies performed by other members in the collaboration.

CHAPTER II

Coherent Control of Population Transfer in the Presence of Dephasing

2.1 Introduction

As discussed in Chapter 1, the theoretical study of condensed phase coherent control is particularly challenging due to environmentally induced relaxation processes. An interesting class of problems which lends itself to the study of the interplay between dephasing and control is the use of phase-modulated femtosecond pulses to control population transfer of molecules in liquid solution. An example of phase modulation is creating a pulse with a time-dependent frequency, or "chirp", which imposes a specific temporal ordering of its frequency components such that different components reach the sample at different times. The parameters which characterize the chirp serve as delicate and sensitive control parameters in the sense that tuning them results in the ability to coherently superpose eigenstates to give constructive or destructive interferences that may maximize or minimize population transfer [4].

For example, a number of studies involving systems that are well described by two-electronic states [44–48] found that the sign of the chirp can be used to control population transfer. In the case of a *linear* chirp, the laser phase is a linear function of time (see Eqn. (2.2)) whose sign determines the temporal ordering of the pulse frequency components: for positive chirp, the low frequency components

reach the sample before the high frequency components whereas for negative chirp the order is reversed. The fact that positively chirped pulses were able to transfer more population than negatively chirped pulses has often been explained as a pump-dump process [49–51]. More specifically, the chirped pulse is described as a single-pulse version of the "pump-dump" scheme of Tannor and Rice described in §1.1.1. Further details regarding the single-pulse version are discussed in §2.6.1.

Since we are interested in control in a condensed phase environment, electronic dephasing effects cannot be ignored. The aim of this work is to understand the efficiency and robustness of chirped-pulse mediated population transfer in a two-electronic state system as a function of the laser intensity and linear chirp, in the presence of pure *electronic* dephasing. We focus on this type of relaxation mechanism since it is assumed to be dominant in condensed phase systems. Importantly, we choose to model the dephasing by a method that is able to interpolate smoothly between the limits of fast and slow fluctuations of the electronic transition frequency (i.e., the limits of homogeneous and inhomogeneous broadening, respectively). In this context, several related theoretical studies of the control of population transfer should be mentioned, the majority of which are based on quantum master equation (QME) approaches with dephasing added in various ways. For example, Mishima et al. [52] and Cao et al. [20] have both studied chirped-pulse control using the same shifted oscillator as that presented in this work. They, too, considered only pure dephasing, but included it in different ways and in the context of a quantum master equation (QME) approach. In the former case, dephasing was incorporated by solving a stochastic Liouville equation and introducing phenomenological dephasing rate constants, while in the latter case it was introduced as a random stochastic phase at the wave function level. However, both cases considered only the limit of

homogeneous broadening where the fluctuations in the transition frequency are small compared with the relaxation rate, making it possible to characterize the dephasing by a single parameter T_2. This scenario corresponds to a special case of the model for dephasing presented in §2.5; the precise connection will be addressed in §2.6. A separate master equation approach applied to a similar shifted oscillator model was put forth by Fainberg and Gorbunov [53], who also studied dissipation effects on population transfer. However, their focus was on modeling solvation effects leading to *vibrational* dephasing, where environmental effects were included as a diffusion on each electronic potential energy surface. While their work contained many interesting results, it neglected electronic dephasing and as such has no direct comparison with our model.

In addition to chirped-pulse control, other studies involving population transfer via stimulated Raman adiabatic passage (STIRAP) in the presence of dephasing have been carried out. Of particular relevance to the work presented here was that by Demirplak and Rice [54], who solved a stochastic Schrödinger equation (SSE). The dephasing was characterized by a Gaussian Markovian model[1] that is able to interpolate between the inhomogeneous and homogeneous limits. This is possible since the fluctuations are characterized in terms of two parameters, the correlation time τ_c and amplitude σ of the fluctuations. To our knowledge, no studies have applied such a Gaussian Markovian and SSE approach to population transfer by way of chirped pulses, which is the focus of the work presented here.

2.2 Chirped Laser Pulses and Control Parameters

Since the control experiments of interest utilize high power laser pulses ($\sim 10^7 - 10^9$ W/cm^2 [45]), quantization of the electric field is unnecessary and the classical de-

[1] Similar to the Kubo theory of lineshapes.

scription $\boldsymbol{\mathcal{E}}(t) = \frac{1}{2}\left[\mathbf{E}(t) + \mathbf{E}^*(t)\right] = \Re\mathbf{E}(t)$ suffices. Further, to good approximation we may assume that the field wavelength is much larger than any molecular dimensions of interest, and ignore the spatial dependence of the field. To model a laser pulse, we assume it has a smooth envelope and is well characterized by

$$\mathbf{E}(t) = \mathbf{E}_0 \exp\left[-\frac{t^2}{2\tau^2}\right] \exp\left[-i\phi(t)\right], \tag{2.1}$$

where $\mathbf{E}_0$ is a complex amplitude, τ is the pulse duration, and $\phi(t)$ is a time-dependent phase. The product $|\mathbf{E}_0| \exp\left[-\frac{t^2}{2\tau^2}\right]$ is known as the "pulse envelope", and will be referred to as such throughout the remaining discussion.

To characterize the chirp of the laser pulse, the phase $\phi(t)$ is expanded in a Taylor series

$$\phi(t) = \phi_0 + \omega_0 t + \frac{1}{2}\alpha t^2 + \frac{1}{3!}\beta t^3 + ... \tag{2.2}$$

where ϕ_0 is a physically irrelevant phase constant[2], ω_0 is the pulse central frequency, and the coefficients α and β are chirp parameters. The instantaneous frequency $\omega_{inst}(t) \equiv \frac{d\phi(t)}{dt}$ is the rate of phase advance. If the series in (2.2) is truncated at second order, then the rate of phase advance is a *quadratic* function of time and the rate of phase advance is linear in time $\omega_{inst}(t) \propto t$. The parameter α, whose sign will be crucial to the analyses presented later in this chapter, is referred to as the linear temporal chirp. It should be noted, however, that although the results presented here incorporate only linear chirp effects, the methodology presented is general enough to allow the inclusion of higher order chirp if desired. (2.2)

To facilitate a frequency domain analysis more in line with experiments, the field in (2.1) may be Fourier transformed to give

$$\tilde{\mathbf{E}}(\omega) = \tilde{\mathbf{E}}_0 \exp\left[-\frac{(\omega-\omega_0)^2}{2\Gamma^2}\right] \exp\left[i\alpha'\frac{(\omega-\omega_0)^2}{2}\right], \tag{2.4}$$

[2]In fact, if $\mathbf{E}(t)$ is chosen as input, then the argument of the complex amplitude $\mathrm{Arg}\{\mathbf{E}_0\}$ may be included with ϕ_0 and subsequently ignored since its presence does not affect populations.

where Γ and α' are the bandwidth and linear spectral chirp, respectively. We take Γ to have a fixed value, since in a realistic experimental situation the spectral chirp is usually adjusted for a fixed power spectrum $P(\omega) = |\tilde{\mathbf{E}}(\omega)|^2 = |\tilde{\mathbf{E}}_0|^2 \left[-(\omega - \omega_0)^2/\Gamma^2\right]$ [20]. The addition of spectral chirp to a pulse increases its duration according to

$$\tau = \tau_0 \sqrt{1 + (\alpha' \Gamma^2)^2}, \tag{2.5}$$

where $\tau_0 = 1/\Gamma$ is the transform limited pulse duration (the shortest its spectral bandwidth permits), and implies the following relations between the chirps and amplitudes

$$\alpha = \alpha' \frac{\Gamma^4}{1 + (\alpha' \Gamma^2)^2} \tag{2.6}$$

$$\tilde{\mathbf{E}}_0 = \mathbf{E}_0 \sqrt{\frac{\tau^2 (1 - i\alpha\tau^2)}{1 + (\alpha\tau^2)^2}}. \tag{2.7}$$

It should also be noted that since the integrated intensity $P_0 = |\mathbf{E}_0|^2 \tau$ is a conserved quantity, chirping a fixed-bandwidth pulse necessarily leads to a decrease in its peak intensity

$$I = I_0 \frac{1}{\sqrt{1 + (\alpha' \Gamma^2)^2}}, \tag{2.8}$$

2.3 Two-State Model in a Rotating Frame and the RWA

In this chapter, the Hamiltonian is that of the two-state model introduced in §1.2.1 (see Eqns. (1.3)-(1.5))

$$\hat{H} = \hat{H}_g \left|g\right\rangle \left\langle g\right| + \left(\hat{H}_e + \hbar\omega_{eg}^0\right) \left|e\right\rangle \left\langle e\right| - \left(\hat{W} \left|g\right\rangle \left\langle e\right| + \hat{W}^* \left|e\right\rangle \left\langle g\right|\right) \tag{2.9}$$

where $\hat{W} \equiv \hat{\mu}_{ge} \mathcal{E}(t)$ and $\hat{H}_{g/e} = T(\hat{P}) + V_{g/e}(\hat{Q})$. In this chapter, we choose the potentials to be *shifted but otherwise identical oscillators*, with $\omega_e = \omega_g \equiv \omega$, so that

(1.4) becomes

$$\begin{aligned} \hat{V}_g &= \frac{1}{2} m\omega^2 \hat{Q}^2 \\ \hat{V}_e &= \frac{1}{2} m\omega^2 \left(\hat{Q} + Q_d\right)^2 \end{aligned} \tag{2.10}$$

In order to implement the numerical methods discussed in §2.4, it is useful to transform the Hamiltonian to a rotating frame. Since the choice of rotating frame is arbitrary[3], we may choose a frame that is tailored to have properties which make the transformed Hamiltonian easier to study. For the two-state model studied here, it proves convenient to define the transformation by

$$\hat{\mathcal{U}} = \exp\left[-i\omega_0 t \left|e\right\rangle \left\langle e\right|\right] \tag{2.11}$$

where ω_0 is the pulse central frequency from (2.2). Following the procedure outlined in Appendix B, (B.6) leads to the Hamiltonian in the rotated frame

$$\begin{aligned} \widetilde{H} &= \hat{\mathcal{U}}^\dagger \hat{H} \hat{\mathcal{U}} - \hbar\omega_0 \left|e\right\rangle \left\langle e\right| \\ &= \hat{H}_g \left|g\right\rangle \left\langle g\right| + \left[\hat{H}_e + \hbar\left(\omega_{eg}^0 - \omega_0\right)\right] \left|e\right\rangle \left\langle e\right| \\ &- \left(\hat{W} e^{-i\omega_0 t} \left|g\right\rangle \left\langle e\right| + \hat{W}^* e^{i\omega_0 t} \left|e\right\rangle \left\langle g\right|\right). \end{aligned} \tag{2.12}$$

In addition to the appearance of the extra phase factors $e^{\pm i\omega_0 t}$ on the off-diagonals, the transformation shifts the energy scale of the excited state potential by one photon of energy $\hbar\omega_0$ and effectively brings the two surfaces into resonance (or nearly so) for some values of $\hat{Q}$. By applying the rotating wave approximation (RWA) to the off-diagonals, we can rewrite $\tilde{H}$ in a form which is more computationally convenient.

[3]Provided the transformation is unitary, which ensures norm conservation of the overall wave function.

For the case of linear chirp, the upper off-diagonal term, for example, becomes

$$\begin{aligned}\hat{W}e^{-i\omega_0 t} &= \frac{1}{2}\hat{\mu}_{ge}\left(E(t)+E^*(t)\right)e^{-i\omega_0 t} \\ &= \frac{1}{2}\hat{\mu}_{ge}e^{-t^2/2\tau^2}\left(E_0 e^{-i\phi(t)}+E_0^* e^{i\phi(t)}\right)e^{-i\omega_0 t} \\ &\approx \frac{1}{2}\hat{\mu}_{ge}E_0 e^{-t^2/2\tau^2}e^{-i\alpha t^2/2}. \end{aligned} \tag{2.13}$$

The last line follows from dropping all terms oscillating at $2\omega_0$ compared with those oscillating at ω_0, since the rapidly oscillating terms would average to zero and thus have no effect on results presented here. Further, since the frequency domain field serves as a program input, it is advantageous in terms of algorithm implementation to recognize that the off-diagonals can be written as the inverse Fourier transform with respect to with respect to $(\omega-\omega_0)$ of the frequency domain field in (2.4) so that

$$E_0 e^{-t^2/2\tau^2}e^{-i\alpha t^2/2} = \mathcal{F}^{-1}\tilde{E}(\omega). \tag{2.14}$$

Thus the rotating frame Hamiltonian becomes

$$\begin{aligned}\widetilde{H} &= \hat{H}_g\left|g\right\rangle\left\langle g\right| + \left[\hat{H}_e+\Delta\right]\left|e\right\rangle\left\langle e\right| \\ &- \left(\widetilde{W}(t)\left|g\right\rangle\left\langle e\right| + \widetilde{W}^*(t)\left|e\right\rangle\left\langle g\right|\right)\end{aligned} \tag{2.15}$$

where $\widetilde{W}(t)\equiv\mathcal{F}^{-1}\tilde{E}(\omega)$. Since the laser central frequency is assumed to be on resonance with the vertical transition frequency $\omega_{ver}\approx\omega_0$, $\Delta\equiv\hbar\left(\omega_{eg}^0-\omega_0\right)=-\frac{1}{2\hbar}\omega^2Q_d^2$ is the so-called Huang-Rhys factor. This particular form for $\widetilde{H}$ is advantageous from a number of standpoints:

- An expression containing the frequency domain field is favorable since the required inputs become the bandwidth Γ and the spectral chirp α', both of which are parameters typically used in spectroscopic experiments. In addition, it renders the inclusion of higher order spectral chirp straightforward by eliminating

the need to compute time-domain fields directly for input, which may be difficult or impossible beyond the linear chirp regime.

- The introduction of the parameter Δ eliminates the need for ω_{ver} and ω_0 as separate inputs. In addition, the definition of Δ could easily be modified to include detuning effects if desired.

2.4 Quantum Mechanical Calculations for Population Transfer

Time-dependent quantum mechanical methods are based on the solution of the time-dependent Schrödinger equation (TDSE)

$$i\hbar\frac{\partial\widetilde{\Psi}(t)}{\partial t} = \widetilde{H}\widetilde{\Psi}(t). \tag{2.16}$$

In the case where the dynamics is governed by the Hamiltonian in (2.15), the TDSE describing evolution on two coupled surfaces assumes a 2×2 matrix form

$$i\hbar\frac{\partial}{\partial t}\begin{pmatrix}\widetilde{\psi}_g(t)\\ \widetilde{\psi}_e(t)\end{pmatrix} = \begin{pmatrix}\hat{H}_g & -\widetilde{W}(t)\\ -\widetilde{W}^*(t) & \hat{H}_e+\Delta\end{pmatrix}\begin{pmatrix}\widetilde{\psi}_g(t)\\ \widetilde{\psi}_e(t)\end{pmatrix}. \tag{2.17}$$

where $\widetilde{\psi}_{g/e}$ is the projection of the wave function onto the g/e electronic surface. The population on the g/e electronic surface[4], is then simply the integral over the square of the probability amplitude

$$p_{g/e}(t) = \int\left|\widetilde{\psi}_{g/e}(Q,t)\right|^2 dQ = \int\left|\psi_{g/e}(Q,t)\right|^2 dQ. \tag{2.18}$$

Probability conservation, which is equivalent to norm conservation of the overall wave function $\widetilde{\Psi}(t)$, then requires that the total population at any time must sum to unity

$$p_g(t) + p_e(t) = 1. \tag{2.19}$$

[4]Synonymous with the probability for the molecule to be in the g/e electronic state.

It should be noted that (2.18) implies that the populations are invariant under the transformation to the rotating frame. Consequently, it is not necessary to transform back to the original frame since the excited state population is the desired quantity in this study.

To initiate our simulations, we assume that prior to the arrival of the pulse, the molecular system is in the ground vibrational level of ground electronic state with no amplitude in the excited state: $p_g = 1, p_e = 0$. After some time, the pulse envelope becomes appreciable and electronic excitation occurs, followed by an amount of amplitude transfer between electronic states. When the pulse envelope is nearly zero, the transfer process ceases and the populations return to constant values. All population maps presented in this chapter refer to the populations after the pulse.

Below, two different computational frameworks for solving the TDSE are presented, where a key difference between them is the choice of representation. In the Fourier Grid Method, the quantum dynamics are captured by discretizing a wave packet and propagating it on a set of lattice points [41]. Importantly, grid methods contain the Franck-Condon overlap factors, which play an imperative role in understanding the efficiency of population transfer, *implicitly*. Thus grid methods can be particularly advantageous for problems with more complicated potentials where the computation of the vibrational eigenstates, and hence the F-C overlaps, becomes difficult. In contrast to grid methods is the Energy Eigenstate method, where the wave function is expanded in a basis of eigenstates of the Born-Oppenheimer potentials with time-dependent coefficients. In this case, the F-C factors appear as *explicit* inputs, which have a simple closed-form expression for the shifted oscillator model presented in §2.3. Thus the energy representation facilitates an understanding of

population transfer in terms of the interplay between the F-C factors and laser pulse characteristics such as intensity and chirp.

2.4.1 Wavepacket Propagation via Fourier Grid Methods

The first numerical method of solution for the TDSE is one in which the calculations are performed in a representation based on the time evolution of wave packets. This representation will herein be referred to as the *grid representation*. The key advantage of such methods is that they avoid explicit diagonalization [7]. We begin with a general discussion of Fourier grid methods, followed by a more detailed discussion of how to adapt such methods to study population transfer processes in molecules using chirped laser pulses.

Due to the fundamentally nonlocal character of quantum mechanical (QM) systems, a major computational difficulty arises in how to construct a discrete Hilbert space that can faithfully represent both the state of the system and the operators associated with physical observables. As it turns out, this Hilbert space is intimately connected with the QM representation of phase space and has important implications in terms of numerical accuracy and efficiency [55]. A common approach is to represent the wave function and operators pointwise on a grid, along with an interpolation scheme for finding the values between grid points. In Fourier methods [56], a set of complex exponentials are selected for use as interpolating functions, which have the desirable properties of being both global and orthogonal. Further, the interpolation is performed by way of an orthogonal collocation method, which results in a highly accurate representation possessing exponential convergence properties [55]. For example, to represent the wave function, we choose the basis of interpolating functions

as

$$\exp\left(2\pi i k x_j/L\right), \qquad k = -(N/2-1), \ldots, 0, \ldots, N \tag{2.20}$$

where L is range of the spatial dimension and N is the number of equally spaced sampling points $x_j = (j-1)\Delta x$. The wave function is then constructed as a linear combination of the interpolating functions

$$\Psi(x_j) \approx \sum_{k=-(N/2-1)}^{N/2} c_k \exp\left(2\pi i k x_j/L\right), \tag{2.21}$$

where $k = p/\hbar$ is the wavevector and the Fourier expansion coefficients c_k are interpreted as the amplitudes of the momentum space wave functions. To estimate the minimum volume such a Fourier representation covers in phase space, we multiply spatial range L by the range in momentum extending from $-p_{max}$ to $+p_{max}$ to give a volume of $2p_{max}L$. On the other hand, it is well known that any discrete representation of phase space in QM requires that each point occupy a minimum volume equal to Planck's constant h [55], so that a grid of N points is has a volume of Nh. Putting together these estimates for the minimum volume $V = hk_{max}L/\pi = Nh$ leads to the Whittaker−Nyquist−Kotelnikov−Shannon sampling theorem [57–59]

$$k_{max} = \pi/\Delta x. \tag{2.22}$$

This theorem is of paramount significance since it implies that interpolation between sampling points may be carried out to any level of accuracy, and in turn guarantees an accurate representation of the wave function. Another notable advantage of Fourier methods is that they utilize a Fast Fourier Transform (FFT) algorithm [60–62], which results in $O(N \log N)$ scaling properties.

With the above formalism in place, we must next consider how to numerically propagate wave functions on a grid. We begin with the general solution to the

TDSE (see Appendix E)

$$\widetilde{\Psi}(t) = \hat{U}(t, t_0)\widetilde{\Psi}(t_0) = \hat{\mathcal{T}} \exp\left[-\frac{i}{\hbar}\int_{t_0}^{t} \widetilde{H}(t')\, dt'\right] \widetilde{\Psi}(t_0) \tag{2.23}$$

where $\hat{U}(t, t_0)$ and $\hat{\mathcal{T}}$ are the time-evolution and time-ordering operators, respectively. Direct numerical implementation of this formula is hindered by the facts that $\widetilde{H}$ appears in an exponential and the construction of $\hat{\mathcal{T}}$ is often cumbersome.

To circumvent the time-ordering difficulty[5], our strategy is to discretize the evolution time interval into N points separated by $\Delta t = t/N$, and assume that $\widetilde{H}$ does not change appreciably within a given segment so that the time ordering in (2.23) may be ignored. This leads to a simpler evolution operator for each time step

$$\hat{U}\left((n+1)\Delta t, n\Delta t\right) \approx \exp\left(-\frac{i}{\hbar}\widetilde{H}\Delta t\right) \tag{2.24}$$

as well as a factorization of the overall evolution operator

$$\hat{U}(t) \approx \prod_{n=0}^{N-1} \hat{U}\left((n+1)\Delta t, n\Delta t\right). \tag{2.25}$$

To derive the basic formula underlying the split-operator propagation scheme, we assume that $\widetilde{H}$ is free from any coordinate-momentum coupling terms and decompose it into a sum of two two terms $\widetilde{H} = T(\hat{P}) + \mathcal{V}(\hat{Q})$, where the first is a function only of the momentum and the second is a function only of the coordinate[6].

Applying the Baker-Hausdorff formula to (2.24) leads to

$$e^{-\frac{i}{\hbar}\widetilde{H}\Delta t} = e^{\bar{T}} \cdot e^{\bar{\mathcal{V}}} \cdot e^{-\frac{1}{2}\left[\bar{T}, \bar{\mathcal{V}}\right] + \mathcal{O}(\Delta t^3)} \tag{2.26}$$

where $\bar{T} \equiv -\frac{i}{\hbar}T(\hat{P})\Delta t$ and $\bar{\mathcal{V}} \equiv -\frac{i}{\hbar}\mathcal{V}(\hat{Q})\Delta t$. It can be shown [55] that by neglecting the last factor in (2.26), the expression

$$e^{-\frac{i}{\hbar}\widetilde{H}\Delta t} \approx e^{\bar{T}} \cdot e^{\bar{\mathcal{V}}} = e^{\bar{T}/2} \cdot e^{\bar{\mathcal{V}}} \cdot e^{\bar{T}/2} \tag{2.27}$$

[5]The difficulty of having $\widetilde{H}$ appearing in an exponential is addressed later in this sub-section.

[6]$\mathcal{V}(\hat{Q})$ contains both the potential energies from the molecular Hamiltonian *and* the dipole coupling terms.

contains errors $\mathcal{O}(\Delta t^3)$. The errors can be minimized by choosing Δt sufficiently small such that it is both a fraction of the smallest timescale inherent to the physical problem and achieves converged results with respect to the population transfer maps presented in §2.6.

The utility of this splitting is manifest in that each of the propagators appearing on the right side of (2.27) may be performed in a *local* representation where they are diagonal. Operating with such local operators on a wave function, then, amounts to a simple multiplication by a complex number and a substantial gain in computational efficiency. The propagation of the wave function by a single time step can be summarized as follows (momentum space and $k-$space are used interchangeably):

1. Fourier transform the coordinate space $\Psi(Q, t = 0)$ to k space
2. Multiply pointwise by the diagonal matrix $\exp\left(-i\frac{P^2}{2m}\frac{\Delta t}{2\hbar}\right)$
3. Inverse Fourier transform $\Psi(P)$ back to coordinate space
4. Multiply pointwise by the diagonal matrix $\exp\left(-i\mathcal{V}(Q)\frac{\Delta t}{\hbar}\right)$
5. Fourier transform to k space
6. Multiply pointwise by the diagonal matrix $\exp\left(-i\frac{P^2}{2m}\frac{\Delta t}{2\hbar}\right)$
7. Inverse Fourier transform to coordinate space

It should be noted that although each propagation step requires multiple calls to an FFT routine, the favorable $\mathcal{O}(N \log N)$ scaling of such routines does not compromise the gain in efficiency described above.

To adapt this methodology to the model Hamiltonian $\widetilde{H}$ introduced in (2.15), we write the overall wave function as a linear combination of wave packets on the two electronic surfaces,

$$\widetilde{\Psi}(Q, t) = \widetilde{\psi}_g \left|g\right\rangle + \widetilde{\psi}_e \left|e\right\rangle \tag{2.28}$$

The states $\widetilde{\psi}_{g/e}(Q,t)$ are the vibrational wave packets on the ground and excited potential surfaces $\hat{V}_{g/e}$, and are composed of a superposition of eigenstates of $\hat{H}_{g/e}$. For brevity, the Q dependence will be suppressed in what follows. For the case of two electronic states considered here, the propagator in (2.27) becomes

$$\exp\left[-\frac{i\Delta t}{\hbar}\begin{pmatrix}\hat{H}_g & -\widetilde{W}\\ -\widetilde{W}^* & \hat{H}_e+\Delta\end{pmatrix}\right] = \exp\left[-\tfrac{i\Delta t}{2\hbar}\begin{pmatrix}\hat{T} & 0\\ 0 & \hat{T}\end{pmatrix}\right]\exp\left[-\tfrac{i\Delta t}{\hbar}\begin{pmatrix}\hat{V}_g & -\widetilde{W}\\ -\widetilde{W}^* & \hat{V}_e+\Delta\end{pmatrix}\right]\exp\left[-\tfrac{i\Delta t}{2\hbar}\begin{pmatrix}\hat{T} & 0\\ 0 & \hat{T}\end{pmatrix}\right] \quad (2.29)$$

Note that for a spatial grid $\{Q_1,\ldots,Q_N\}$ and its associated Fourier (k space) grid $\{k_1,\ldots,k_N\}$, each of the operators $\hat{T}, \hat{V}_{g/e}$ and $\widetilde{W}$ are diagonal in a local representation. e.g., $\hat{V}_{g/e}$ is diagonal in coordinate space while $\hat{T}$ is diagonal in k space:

$$\hat{V}_{g/e} = \begin{pmatrix} V_{g/e}(Q_1) & 0 & \ldots & 0\\ 0 & V_{g/e}(Q_2) & \ldots & 0\\ \vdots & \vdots & \ddots & \vdots\\ 0 & 0 & \ldots & V_{g/e}(Q_N)\end{pmatrix},\quad \hat{T} = \begin{pmatrix} T(k_1) & 0 & \ldots & 0\\ 0 & T(k_2) & \ldots & 0\\ \vdots & \vdots & \ddots & \vdots\\ 0 & 0 & \ldots & T(k_N)\end{pmatrix} \quad (2.30)$$

Since it involves the exponentiation of a diagonal matrix, the kinetic energy propagator appearing in (2.29) is also diagonal. Consequently, only storage of the diagonal elements $\exp\left(-\frac{i\Delta t}{2\hbar}T(k_j)\right), j=1,N$ is required, and the kinetic energy propagation reduces to a simple point-wise multiplication on the wave function. The potential energy propagator, however, contains the exponential of a matrix that is not diagonal but consists of four diagonal blocks. This block structure makes the matrix exponential amenable to the formal diagonalization procedure[7] outlined in Appendix

[7]Expanding the matrix exponential in a power series for small Δt is possible, but would compromise accuracy [41].

A. Thus the matrix exponential may be recast as simple and more computationally efficient product of matrices:

$$\exp\left[-i\frac{\Delta t}{\hbar}\begin{pmatrix}\hat{V}_g & -\widetilde{W}\\ -\widetilde{W}^* & \hat{V}_e+\Delta\end{pmatrix}\right]= \exp\left[-i\tfrac{\Delta t}{4\hbar}V_+\right]\hat{1}\begin{pmatrix}\cos\beta+i\frac{\sin\beta}{2r}V_- & i\frac{\mu_{ge}\sin\beta}{r}\widetilde{W}\\ i\frac{\mu_{ge}\sin\beta}{r}\widetilde{W}^* & \cos\beta-i\frac{\sin\beta}{2r}V_-\end{pmatrix} \tag{2.31}$$

where $V_\pm \equiv \left(\hat{V}_e+\Delta\right)\pm\hat{V}_g$, $r=\frac{1}{2}\sqrt{V_-^2+4|\widetilde{W}|^2}$ and $\beta\equiv\frac{rt}{2\hbar}$. It should be noted that the block structure described above, where *each* block is diagonal, is a direct consequence of working in a spatial representation. Consequently, the same procedure for rewriting the matrix exponential cannot be used when working in an energy eigenstate basis, as described in the next section.

2.4.2 Energy Representation

An alternative method by which to solve the TDSE is to find an expression for the overall propagator $e^{-i\widetilde{H}t/\hbar}$ in a vibronic basis of states. This basis was introduced in §1.2.1, where it was shown how the Franck-Condon (F-C) factors, $S_{j,k}$ arise. Following an analogous procedure leads to the rotating frame Hamiltonian expressed in the vibronic basis

$$\begin{aligned}\widetilde{H} &= \sum_{j=0}^{N_g}\varepsilon_{g,j}\left|g,j\right\rangle\left\langle g,j\right| + \sum_{k=0}^{N_e}\left(\varepsilon_{e,k}+\Delta\right)\left|e,k\right\rangle\left\langle e,k\right| \\ &- \sum_{j=0}^{N_g}\sum_{k=0}^{N_e}\left(\widetilde{W}S_{j,k}\left|g,j\right\rangle\left\langle e,k\right| + \widetilde{W}^*S_{j,k}^*\left|e,k\right\rangle\left\langle g,j\right|\right)\end{aligned} \tag{2.32}$$

where $N_{g/e}$ is an integer related to the number of vibrational states on a given electronic surface to consider when constructing a finite representation of $\widetilde{H}$. In practice, few states play a role in population transfer, due to the modulation of the transition frequencies by the F-C factors. For simplicity, we assume that an

equal number of states on each surface are involved in the population transfer, so that $N_e = N_g$. To assign a value to N_e, we first identify the excited vibronic state which lies nearest to the vertical transition, and add a band of vibrational states symmetrically around it. The width of the band is sensitively dependent upon the displacement Q_d, and the correct choice is dictated by convergence of the excited state population maps. We choose to measure the energy levels $\left\{\varepsilon_{g/e,l}\right\}$ relative to the ground state of the g/e electronic surface, so that in the case of harmonic potentials, $\varepsilon_{g/e,l} = l\hbar\omega$. The appearance of the F-C factors as explicit inputs in (2.32) is one of the main advantages of working in the energy representation, as it helps elucidate their importance in the population transfer process, in addition to chirp parameters and field intensity.

It should be noted that the magnitude of $S_{j,k}$ depends on the displacement Q_d of the oscillator minima, and is closely linked to which terms in (2.32) contribute appreciably to $\widetilde{H}$. In general, higher lying vibrational states on the excited state potential become important for increasing values of Q_d, since larger displacements result in a larger vertical transition frequency.

In order to form the propagator in the vibronic basis, we must exponentiate the

matrix

$$\widetilde{H} = \begin{pmatrix} \varepsilon_{g,0} & 0 & 0 & \cdots & \widetilde{W}S_{00} & \widetilde{W}S_{01} & \widetilde{W}S_{02} & \cdots \\ 0 & \varepsilon_{g,1} & 0 & \cdots & \widetilde{W}S_{10} & \widetilde{W}S_{11} & \widetilde{W}S_{12} & \cdots \\ 0 & 0 & \varepsilon_{g,2} & \cdots & \widetilde{W}S_{20} & \widetilde{W}S_{21} & \widetilde{W}S_{22} & \cdots \\ \vdots & \vdots & \vdots & \ddots & \vdots & \vdots & \vdots & \vdots \\ \widetilde{W}^*S^*_{00} & \widetilde{W}^*S^*_{01} & \widetilde{W}^*S^*_{02} & \cdots & \varepsilon_{e,0}+\Delta & 0 & 0 & \cdots \\ \widetilde{W}^*S^*_{10} & \widetilde{W}^*S^*_{11} & \widetilde{W}^*S^*_{12} & \cdots & 0 & \varepsilon_{e,1}+\Delta & 0 & \cdots \\ \widetilde{W}^*S^*_{20} & \widetilde{W}^*S^*_{21} & \widetilde{W}^*S^*_{22} & \cdots & 0 & 0 & \varepsilon_{e,2}+\Delta & \cdots \\ \vdots & \vdots & \vdots & \cdots & \vdots & \vdots & \vdots & \ddots \end{pmatrix} \tag{2.33}$$

which has a block form similar to the potential energy propagator in (2.29), except the off-diagaonal blocks are *no longer diagonal*. As before, we wish to rewrite the matrix exponential as a product of matrices, but in the vibronic basis a numerical diagonalization scheme will be required.

We begin by noting that since $\widetilde{H}$ is Hermitian, it may be diagonalized by a unitary transformation $\hat{\mathcal{U}}$ according to

$$\hat{\mathcal{U}}\widetilde{H}\hat{\mathcal{U}}^\dagger = \hat{D} \tag{2.34}$$

where the columns of $\hat{\mathcal{U}}$ are the eigenvectors of $\widetilde{H}$, and $\hat{D}$ is a diagonal matrix whose elements are the eigenvalues of $\widetilde{H}$, $\{\lambda_j\}$. Using the Hermiticity property $\hat{\mathcal{U}}\hat{\mathcal{U}}^\dagger = \hat{1}$ and using the results from Appendix D leads to

$$\begin{aligned} \exp\left[-i\frac{\Delta t}{\hbar}\widetilde{H}\right] &= \hat{\mathcal{U}}\exp\left[-i\frac{\Delta t}{\hbar}\hat{D}\right]\hat{\mathcal{U}}^\dagger \\ &= \hat{\mathcal{U}}\begin{pmatrix} e^{-i\frac{\Delta t}{\hbar}\lambda_1} & & & 0 \\ & e^{-i\frac{\Delta t}{\hbar}\lambda_2} & & \\ & & e^{-i\frac{\Delta t}{\hbar}\lambda_3} & \\ 0 & & & \ddots \end{pmatrix}\hat{\mathcal{U}}^\dagger. \end{aligned} \tag{2.35}$$

Thus the propagator reduces to a simple product of three matrices, drastically simplifying its computation. To summarize, the propagation of the wave function by a single time step is as follows:

1. Construct the matrix representation of $\widetilde{H}$ according to (2.33), where the F-C factors are obtained from (1.10).
2. Numerically diagonalize $\widetilde{H}$ to find its eigenvectors and eigenvalues, and from them construct the transformation $\hat{\mathcal{U}}$ and the diagonal matrix $\hat{D}$.
3. Compute the matrix propagator in (2.35), and multiply pointwise by it to advance the wave function by a single time step

It should be noted that to achieve converged results, the integers N_g, N_e in (2.32) are chosen to have values between 12 and 22, which results in matrices of size 44×44 and smaller. Despite the fact that the diagonalization must be performed at each time step, it does not create a computational bottleneck since a highly optimized Fortran90 LAPACK routine is used[8]. Thus the generalization of the above procedure to systems that require the inclusion of a greater number of states, which in turn leads to larger matrices, is not problematic.

2.5 Dephasing Effects

The theoretical developments presented thus far in this chapter have essentially described the dynamics of a molecule interacting with a laser field, but have not accounted for any variation in the transition frequency. Such variations are unavoidable in real transitions, whether in the gas or condensed phase, and always involve line broadening[9]. If a solvent is present, fluctuations in the solvent environment induce fluctuations in the instantaneous transition frequency of the solute molecule [63].

[8] For details, see *zheev.f90* available at http://www.netlib.org/lapack.

[9] Even if Doppler broadening was absent in the gas-phase, lifetime broadening would necessarily be present since the time-energy uncertainty relation implies that all radiation-induced excited states have a finite lifetime.

To account for this, we take a phenomenological approach and describe the fluctuations by a stochastic model analogous to that used in the Kubo theory of line shapes [64]. Implicit to our method of implementation is the assumption that *pure electronic dephasing* is the dominant relaxation mechanism, since it is typically the fastest relaxation process in a condensed phase environment [20, 23, 54]. This leads to a Stochastic Schrodinger Equation (SSE), whose solution will be discussed further below. Of key importance to the analysis of the results will be the interplay between the different timescales associated with the chirp rate, the system oscillator frequency, and those inherent to the stochastic model.

2.5.1 Stochastic model for fluctuating energy levels

Since fluctuations in a real system possess a characteristic timescale which may be fast or slow compared with any inherent system timescales, the choice of computational scheme requires a statistical description general enough to include it. A particularly advantageous choice is that of exponentially correlated Gaussian noise, also known as Ornstein-Uhlenbeck noise [65–68], which is not only straightforward to implement computationally but is also able to capture effects to help elucidate the conditions under which dephasing is compatible with coherent control of population transfer.

A Gaussian noise model is characterized by the properties outlined below, and illustrated graphically in Figure 2.1:

- The initial random values $\xi(t=0)=\xi_0$ are sampled from a normal distribution of width σ

$$P(\xi_0)=\frac{1}{\sqrt{2\pi\sigma^2}}\exp\left(-\frac{\xi_0^2}{2\sigma^2}\right) \tag{2.36}$$

- The first statistical moment is finite, and can always be redefined to be zero

$$\langle \xi(t) \rangle = 0 \tag{2.37}$$

- The correlation function decays exponentially[10] with a correlation time τ_c, and depends only on the time difference $|t - t'|$ as opposed to t, t' individually

$$C(t - t') \equiv \{\langle \xi(t)\xi(t') \rangle\} = \sigma^2 \exp\left(-|t - t'|/\tau_c\right) \tag{2.38}$$

  where $\{\ldots\}$ denotes averaging over the initial distribution in (2.36).

From a physical standpoint, the magnitude of the frequency (energy) fluctuations σ relative to the rate of relaxation $1/\tau_c$ is of crucial importance since it gives rise to distinct dynamical regimes.

As mentioned in the introduction, for an isolated molecule the transition frequency is unique, and in terms of a lineshape this would lead to an infinitely narrow line. In the presence of a solvent, however, the modulation of the transition frequency reflects interactions with the solvent DOF, and leads to a broadening of the spectral lines. In particular, we are interested in the following cases:

- The limit of *slow fluctuations*, or inhomogeneous broadening. The transition frequency is modulated on a timescale longer than τ_c, which implies that the energy fluctuations are large relative to the relaxation rate $\sigma \gg 1/\tau_c$. This represents a static inhomogeneity in the solvent environment so that each solute molecule in an ensemble experiences a different but constant transition frequency, and leads to a broad spectral line.

- The limit of *fast fluctuations*, or homogeneous broadening. The transition frequency is modulated on a timescale shorter than τ_c, which implies that the energy fluctuations are small relative to the relaxation rate $\sigma \ll 1/\tau_c$. In this case,

[10] Guaranteed by the Doob theorem for any Gaussian distribution of fluctuations that generates a Markov process [69].

the spectrum of solute states becomes very narrow, since each solute molecule in an ensemble essentially experiences an averaged transition frequency, with little variation between different solute molecules. This also leads to a broadening of the spectral line with respect to the solvent-free case, but to a lesser extent. Since the line is narrowed with respect to the inhomogeneously broadened case and the fluctuations in the solvent are very rapid, this case is also referred to as *motional narrowing*.

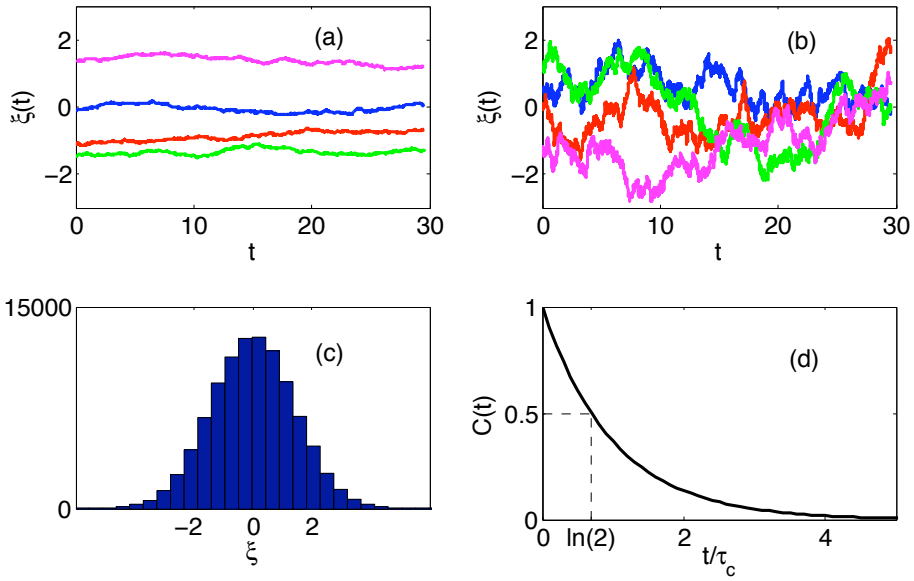

Figure 2.1: Energy fluctuation statistics for $\sigma = 1$. Sample noise trajectories for correlation times (a) $\tau_c = 10^3 \times \tau_0$ and (b) $\tau_c = 10 \times \tau_0$, corresponding histogram (c) with FWHM is $2\sqrt{2\log 2}\sigma$, and (d) the noise correlation function $C(t) = \langle \xi(t)\xi(0) \rangle$ from (2.38).

2.5.2 Solving the Stochastic Schrödinger Equation

In this section, we follow an approach based on representing the state of the system in terms of a wave function, whose dynamics is governed by a stochastic Scrhrödinger equation (SSE). Since electronic pure dephasing is assumed to be the main relaxation process, the energy levels within a given electronic surface are assumed to be fixed relative to one another, while the electronic transition frequency fluctuates randomly in time. As such, we consider the ground electronic manifold of states to be fixed, and

allow the entire excited state manifold to fluctuate[11]. In order to incorporate such effects into the vibronic Hamiltonian of (2.33), we first generate a noise trajectory $\xi(t)$ and subsequently modify the energy levels that appear on the diagonal [67]. Since only the *relative* fluctuations between the ground and excited surfaces are of interest, we assume without any loss of generality that the ground state surface remains fixed while only the excited state surface fluctuates:

$$\begin{aligned} \varepsilon_{g,l} &\rightarrow \varepsilon_{g,l} \\ \varepsilon_{e,l} + \Delta &\rightarrow \varepsilon_{e,l} + \Delta + \xi(t) \end{aligned} \tag{2.39}$$

With this modified Hamiltonian, the TDSE is solved for *each* trajectory as described in §2.4.2. In order to realize the proper statistical properties of the noise, the procedure must be repeated for many distinct trajectories and the results averaged [54].

2.6 Results and Discussion

2.6.1 Dephasing-Free Population Transfer

This section presents an overview of dephasing-free population transfer by chirped pulses, in order to provide a wave packet interpretation of the transfer mechanism and to clearly establish our choice of parameters. In addition, the dephasing-free case will serve as an important basis for comparison for the results in §2.6.2 and §2.6.3 which include dephasing effects. It should be noted that the aim of this work is to understand population transfer by way of high-power chirped pulses, ignoring population relaxation effects. This should be contrasted to low-power excitation used to study the vibrational coherences created by chirped pulses on both the ground and excited states [45, 49].

The main results presented in this chapter are in terms of contour maps of the

[11] This is without any loss of generality, since we are only interested in the relative energy difference.

excited state population transfer as a function of two control parameters. More specifically, the height corresponds to the amount of population remaining in the excited electronic state after the chirped pulse has been turned off, and the axes are the spectral chirp α' and the frequency domain field amplitude $\tilde{E}_0$. Throughout the following discussion, these will be referred to as "population maps".

Dimensionless variables, denoted by an overbar, are used throughout this work such that time, length, energy, and frequency are scaled as follows: $\bar{t} = \omega t$, $\bar{Q} = \sqrt{m\omega/\hbar}Q$, $\bar{\epsilon} = \epsilon/\hbar\omega$, $\bar{\Omega} = \Omega/\omega$, where m and ω are the reduced mass and frequency, respectively[12]. From here on, the overbars are dropped and all variables are assumed dimensionless unless given explicitly with units. Throughout this work, a relatively small value for the horizontal displacement was fixed at $Q_d = 1$.

The calculations were performed using the energy representation method of §2.4.2, since the inclusion of dephasing effects was more straightforward than in the grid method of §2.4.1[13]. The number of vibronic states used to construct the matrix representation of the $\tilde{H}$ in (2.32) was chosen by convergence of the population maps. In practice, this means that the minimum value of N_e is found by starting with a small N_e value and repeating the calculation for successively larger values until the results cease to change. For the value $Q_d = 1$ used here, $N_g = N_e = 10$ is sufficient and leads to a typical matrix size of $(2N_e + 1) \times (2N_e + 1) = 22 \times 22$. The bandwidth is fixed at $\Gamma = 1.27$, and the transform limited pulse duration is defined as $\tau_0 = 1/\Gamma$.

The two variable inputs are the linear spectral chirp α' ranging from -2 to 2, and the frequency domain field amplitude $\tilde{E}_0$ ranging from 0 to 10. In our calculations, each variable was chosen to be a vector of N_{map} points. The maps are generated on a grid of $N_{map} \times N_{map}$ points, and as such require N_{map}^2 separate solutions of the

[12] For two oscillators with different frequencies, $\omega_e \neq \omega_g$, variables are scaled with respect to one of the oscillators.

[13] The dephasing-free results were verified using the grid method. Also, the grid method may be more advantageous for other applications, such as anharmonic potentials.

Schrödinger equation. For the maps presented in this chapter, sufficient resolution was achieved for $N_{map} = 33$. Since the pulse duration increases with chirp according to (2.5), the range of α' studied here implies a maximum pulse duration of $\tau = 3.4 \times \tau_0$. The time-step was chosen to be a sufficiently small fraction of the smallest timescale relevant to the problem. In the energy representation, the relevant timescales[14] are the pulse duration τ_0 and noise correlation time τ_c, and the time-step was chosen as $\Delta t = \min(\tau_0, \tau_c)/200$. The time-step was not adapted for different values of τ, since it did not lead to a substatial savings in the number of required time-steps. For the dephasing-free case, τ_c is irrelevant and the time step is based only on τ_0. The initial state was chosen to be the ground vibrational state on the ground electronic surface. The excited state population $p_e(t_f)$ was calculated according to (2.18), where t_f is a time after the pulse is turned off, and is long enough such that p_e has reached a constant, asymptotic value.

Figure 2.2 shows a contour map of the final excited state population as a function $\tilde{E}_0$ and α', where red and blue correspond to 100% and 0% transfer, respectively. For

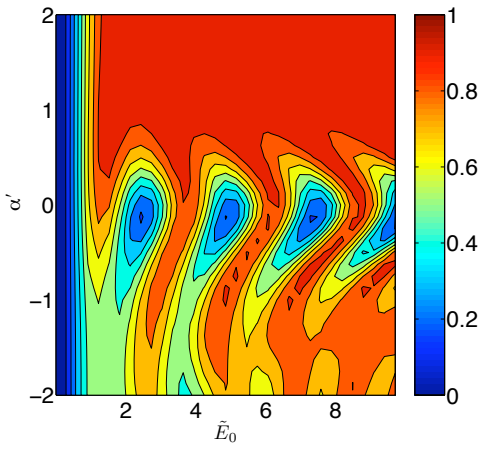

Figure 2.2: Final excited state population contour as a function of the frequency domain field amplitude $\tilde{E}_0$ and the linear spectral chirp α', for an isolated molecule at 0K.

a large range of field amplitudes, there is an overall transfer asymmetry between the

[14] In a grid representation, however, the period of the wave packet motion must also be considered.

positively chirped (PC) and negatively chirped (NC) regions. To understand this as well as some of the finer map features, the interplay between the F-C factors and resonance must be considered. In general, for a vibronic transition to occur between

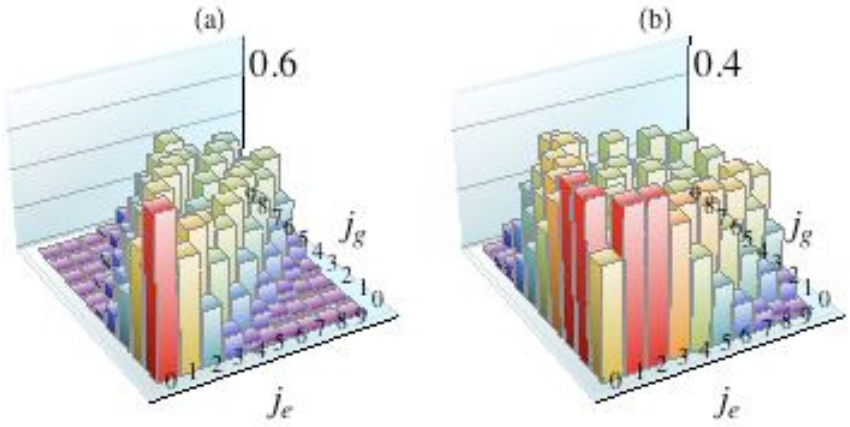

Figure 2.3: Franck-Condon overlap factors (absolute value) for horizontal displacement (a) $Q_d = 1$ used for the population maps presented in this chapter, and (b) $Q_d = 2$ for comparison. Integers j_g and j_e label the ten lowest vibrational eigenstates of the ground and excited electronic states, respectively, and the height of the bar corresponds to the absolute value of the overlap.

the electronic surfaces, the laser pulse must contain a frequency resonant with it. Although necessary, this condition alone is not sufficient due to the appearance of the F-C factors in the off-diagonal matrix elements of the Hamiltonian, $\widetilde{W}S_{jk}$. The F-C factors thus modulate the transition amplitudes, so that small overlaps result in ineffective population transfer between a given pair of vibronic states. It should be noted that the F-C factors are sensitive to the choice of Q_d since the number of vibronic states with appreciable overlaps changes with its value, as illustrated in Figure 2.3. Thus in addition to chirp sign, both intensity and F-C factors will play a role in the interpretation of the population map, as discussed below.

For small field amplitudes $\tilde{E}_0 \lesssim 1.0$, there is no asymmetry with respect chirp sign. This is consistent with early experimental studies, which have shown that population transfer is independent of the chirp in the weak field limit [73, 74]. In

addition, for $\tilde{E}_0 \lesssim 0.5$, the field is so weak that there is negligable coupling between the vibronic states, resulting in minimal population transfer.

For field amplitudes above $\tilde{E}_0 \gtrsim 1.0$, there is a large plateau of nearly perfect transfer for positive chirp but not for negative chirp. This feature may be explained at the gross level by an intuitive intrapulse pump-dump mechanism, which is a single pulse version of the Tannor-Rice "pump-dump" scheme referred to in §2.6.

When the leading edge of a chirped pulse is incident upon the sample, excitation is initiated by transferring probability amplitude from the ground electronic state V_g to the excited state V_e [53]. This results in the creation of a wave packet on the excited state surface by coherently superposing a set of vibrational eigenstates[15]. The wave packet composition is determined by the vibronic transitions that have both a frequency that lies within the pulse bandwidth and an appreciable F-C factor. The largest F-C factor corresponds to the vertical transition, according to the Franck-Condon Principle. Since this wave packet is not an eigenstate of the excited surface, it begins to evolve in time, moving from a region of higher ω_{high} to lower ω_{low} transition frequency (see Figure 2.4). Since the mechanism described here does not rely on the inclusion of dissipative effects, the overall energy of the the wave packet is considered *constant*. Thus higher/lower frequency in this context refer to the instantaneous energy gap between the ground and excited potentials, based on the instantaneous position of the wave packet center[16].

If the pulse is negatively chirped as in Figure 2.4, the blue edge containing the high frequency components leads the red edge temporally, and as such may "follow" the motion of the wave packet by transferring amplitude sequentially back to the

[15]The ordering of the frequency components in the case of the pump pulse is inconsequential for purposes of creating the initial wave packet.

[16]For harmonic potentials the shape of the wave packet remains unchanged as it evolves, but the width may change if the two potentials are of different frequencies. The qualitative picture is expected to be the similar for anharmonic potentials.

ground state via stimulated emission [44]. As a result, the amount of amplitude

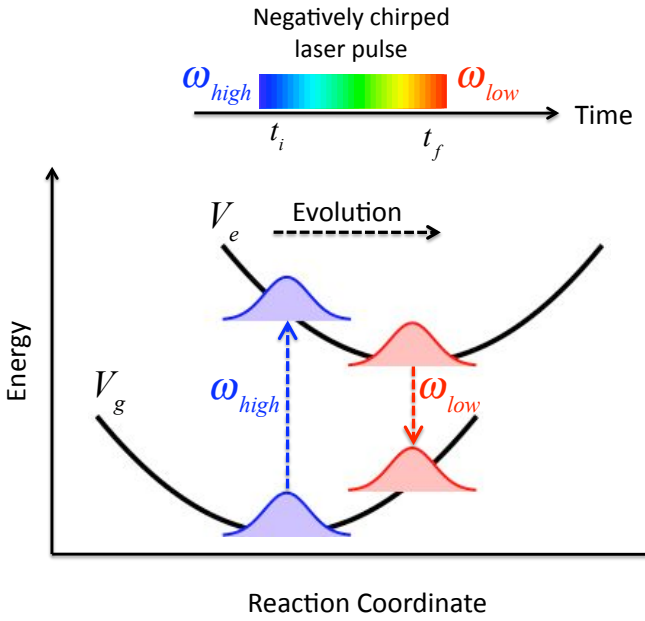

Figure 2.4: Intrapulse "pump-dump" mechanism between two electronic states V_g and V_e. The top part of the figure represents a negatively chirped pulse, where the high frequency components arrive earlier in time than the low frequency ones. Population is first transferred upward by the blue edge of the pulse, followed by time evolution of the wavepacket for a time on the order of the pulse duration $\sim t_f - t_q i$, and finally population is tranferred downward by the red edge of the pulse.

in the excited state is minimized and little overall population transfer results. If, however, the second pulse is positively chirped so that the red edge leads the blue edge, by the time the wave packet moves into the region of ω_{low}, the blue edge is incident upon it but is out of resonance. Thus more amplitude remains trapped on the excited state, resulting in enhanced population transfer.

This description should be contrasted with the widely used "sliding wave packet" picture presented in many earlier papers [45, 50]. There, the motion of the excited state wave packet is described as sliding down the potential surface from higher to lower energies, resulting in a dynamic Stokes shift. Such a picture implies that the asymmetry in the efficiency of population transfer with respect to chirp sign is necessarily linked to dissipative effects, even though the theoretical description is

dissipation-free. In fact, other theoretical studies have shown a marked asymmetry with respect to chirp sign even when dephasing was absent [46, 75].

Although the portion of the map $1 \lesssim \tilde{E}_0 \lesssim 4.5$ clearly shows regions where PC is more effective than NC, it becomes much less pronounced at higher intensities. This fact may be ascribed to the form of the off-diagonal matrix elements, $\widetilde{W}S_{jk}$, since $\widetilde{W} = \mathcal{F}^{-1}\tilde{E}(\omega)$ is a monotonically increasing function of $\tilde{E}_0$. For a given vibronic transition, then, it is possible for a strong enough field to overwhelm even an unfavorable F-C factor[17].

The central portion of the map along the $\alpha' = 0$ line also deserves attention. All points along this line correspond to transform limited pulses, since by (2.5) zero spectral chirp implies that $\tau = \tau_0$. In this limit, the pulse duration is much shorter than the timescale of the vibrational motion, and the displaced harmonic system responds to the laser pulse as a two-level system [20, 43, 76]. The laser pulse acts in a manner analogous to a π pulse for a two-level system, where population is cycled between the two vibronic states involved in the vertical transition (or very close to it). This behavior is clearly seen in Figure 2.2, where minima occur at equally spaced intervals of 2π.

To further understand the analogy to Rabi flopping in a two-level system, we consider the two points in Figure 2.2 where $|\tilde{E}_0| = 3.7$ and $|\tilde{E}_0| = 4.8$, both for $\alpha' = 0$, which correspond to a maximum and minimum in the population transfer, respectively. Prior to arrival of the pulse, all population is in the ground electronic state, so that $p_g = 1, p_e = 0$, and the probability density is that of the $j_g = 0$ harmonic oscillator ground state. Figures 2.5(a) and 2.5(b) show that during the pulse both populations exhibit oscillations at the Rabi frequency $\mu_{ge}|\tilde{E}_0| = 3.7$, and

[17] Provided it is not identically zero.

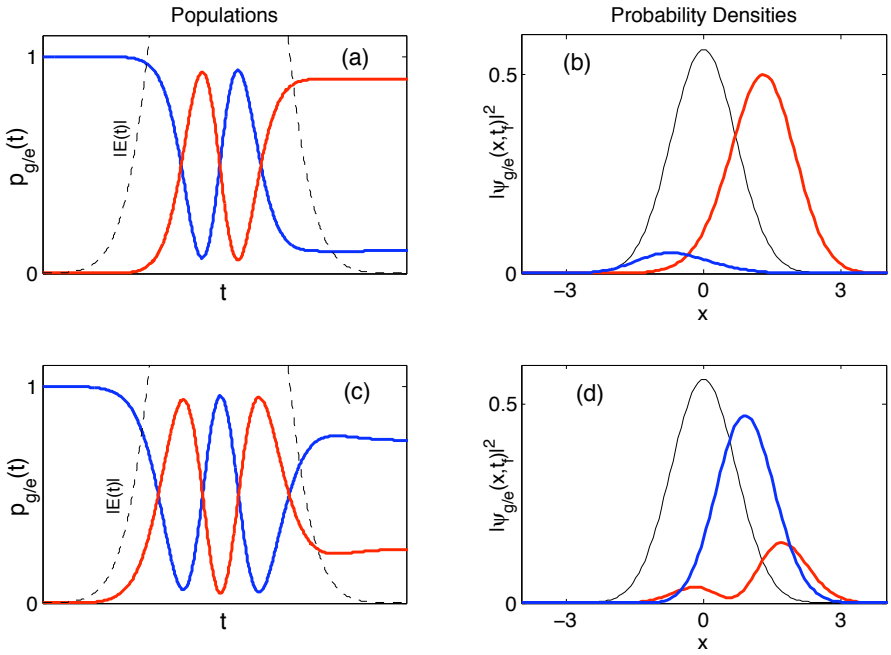

Figure 2.5: Ground and excited state populations and wave function probability densities for zero chirp $\alpha' = 0$. Left panels: The pulse envelope $|E(t)|$ (black dashed), ground state population $p_g(t)$ (blue) and excited state population $p_e(t)$ (red). Right panels: Probability densities of the ground state before the pulse (black), the ground state after the pulse at t_f (blue) and the excited state after the pulse at t_f (red). Lower intensity $|\tilde{E}_0| = 3.7$ is shown in (a) and (b), while higher intensity $|\tilde{E}_0| = 4.8$ is shown in (c) and (d).

after the pulse most of the population is left in the excited state. This fact is reflected in the probability densities after the pulse as well, where the excited state density is much larger than that of the ground state, indicating a large amount of transfer. Figures 2.5(c) and 2.5(d) also exhibit oscillations at $\mu_{ge}|\tilde{E}_0| = 4.8$, only now the period is such that more population is left in the ground state. The probability densities also reflect this.

2.6.2 The Limit of Slow Fluctuations

To place the discussion in a physical context, we first consider an ensemble of solute molecules embedded in a solvent. At a given instant of time each solute will have its own transition frequency, indicative of differences in its local environment [77]. Further, the dynamics of that local environment causes the transition frequency to

fluctuate in time. If the timescale of these fluctuations is slow enough such that the environment looks static over the experimental timescale, then the line shape of the ensemble will reflect the distribution of frequencies [78]. This is referred to as the slow modulation limit, and implies that the relaxation rate of the fluctuating solvent is much smaller than the width of the distribution of frequencies visited by the ensemble of solutes. In terms of the Gaussian Markovian noise model introduced in §2.5.1, this situation amounts to choosing $\sigma \gg 1/\tau_c$. It is this limit which is the focus of the first part of this study.

The problem is essentially characterized by three timescales: τ_c and σ^{-1}, which describe the solvent dynamics, and τ_0, the transform-limited pulse duration. In the inhomogeneous limit, τ_c is very large, so we first focus on the interplay between τ_0 and σ^{-1}. To this end, we chose the numerical equivalent of the $\tau_c \to \infty$ limit, which means that it was chosen large enough such that further increases had no effect on the population map, and computed the population map for increasing values of σ. The main results are presented in Figure 2.6.

As discussed in §2.6.1, successful control of population transfer is intimately linked to resonance. In the presence of a solvent, the resulting shift in transition frequency essentially acts as a detuning away from resonance, so that the laser central frequency is no longer directly on resonance with the vertical transition. As a result, the initial wave packet created on the excited state will be a different superposition of vibrational states for each realization of the stochastic process, and consequently will exhibit different dynamics. This will inevitably lead to variations in the population transfer, by either enhancing or diminishing it. By averaging over many such variations, the contributions tend to cancel one another, and as a result an overall decrease in transfer efficiency is expected. Here, "overall" refers to the fact that, for

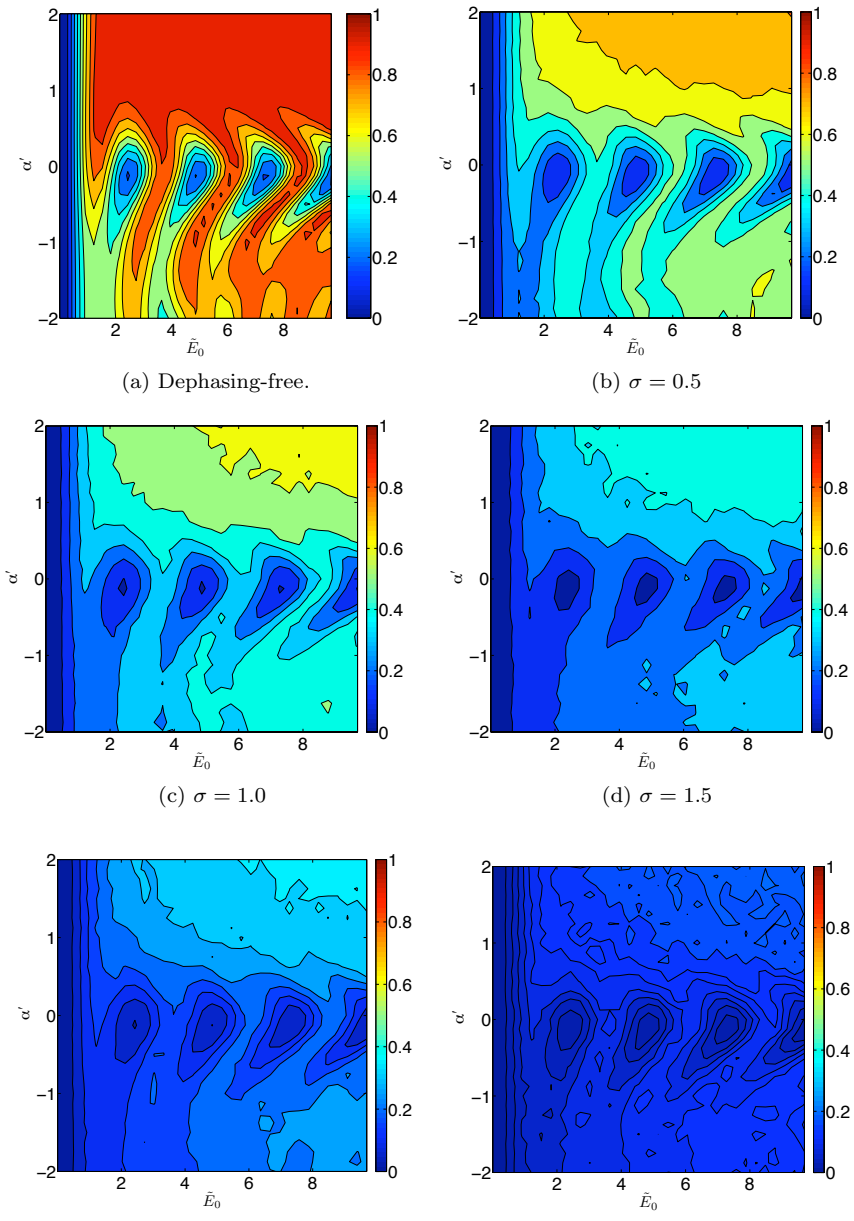

(a) Dephasing-free.

(b) $\sigma = 0.5$

(c) $\sigma = 1.0$

(d) $\sigma = 1.5$

(e) $\sigma = 2.0$

(f) $\sigma = 4.0$

Figure 2.6: Population maps showing the approach to the inhomogeneously broadened limit. The correlation time is $\tau_c = 10^4 \times \tau_0$, where $\tau_0 = 0.79$ is the transform limited pulse duration, and increasing values of the fluctuation amplitude are shown in subfigures (a)-(f). All maps were averaged over 2000 realizations of the stochastic process to ensure convergence.

a given σ, there is no reason to expect some portions of the map to be more affected by the noise than others.

Since increasing σ increases the width of the distribution from which the detunings are sampled, we expect the overall decrease in transfer efficiency to become more pronounced as σ increases. This is indeed seen in Figure 2.6, where less population transfer occurs the as the limit $\sigma \gg 1/\tau_c$ is realized more fully (the dephasing-free case is included for comparison). From this, we conclude that in the inhomogeneously broadened limit, the presence of pure dephasing disrupts the ability to selectively control population transfer for $\sigma \gtrsim 2$.

To assess the validity of this result in terms of a real physical system, we compared this result to a series of experiments performed on the oxazine dye LD690 in various alcohol solvents. Bardeen and Shank [79] made a systematic comparison of the effect of different solvents on the absorption spectrum, in order characterize both the fast and slow solute-solvent interactions. They found that the fastest interactions depended sensitively on the solvent[18], and modeled them by a solvent correlation function using the formalism developed by Mukamel [81]. The solvation mode parameters, including $\sigma \approx 200\text{cm}^{-1}$ and $\tau_c = 20\text{fs}$ for LD690 in methanol, were determined by fitting experimental data to their model in the homogenously broadened limit.

A separate experiment by Cerullo et al. [45] looked at the chirped pulse excitation of LD690 in methanol, and observed a strong linear chirp dependence of the population transfer. Since Raman data for LD690 shows at least 18 intramolecular modes coupled to the lowest electronic transition as well as several solvent modes, modeling each mode explicitly would be cumbersome if not impossible. Consequently, they

[18]MD simulations suggested that solvation occurs via rapid, librational-type motions of the -OH groups [80].

chose an oscillator model with a single, highly displaced low-frequency (170cm^{-1}) mode, which was meant to qualitatively capture the multimode dynamics. Although their model was *purely* quantum mechanical, their interpretation was not. The results were explained in terms of an intrapulse pump-dump mechanism similar to that described in §2.6.1, except that it included relaxation effects (i.e., dephasing) by assuming that wave packet loses energy as it evolves on or "slides down" the excited state potential surface.

To make contact with these experiments, we took our shifted oscillator model to coincide with the low-frequency oscillator model of Cerrullo et al., and used $\omega = 170\text{cm}^{-1}$ as the frequency scale to convert our parameters into dimensionful quantities. This leads to a pulse duration and frequency distribution width of $\tau_0 = 25\text{fs}$ and $\sigma = 340\text{cm}^{-1}$, respectively. These values are roughly on the order of those used by Bardeen and Shank, $\tau_0 = 10\text{fs}$ and $\sigma = 200\text{cm}^{-1}$, and leads to a comparison of time scales: In our case, $\sigma/2\pi c \approx 0.26 \times 1/\tau_0$, whereas in their case $\sigma/2\pi c \approx 0.12 \times 1/\tau_0$.

Although the numbers are close, this leads to an apparent inconsistency. Their dephasing-free model suggests that control is possible, whereas using the same parameters in our model does not. Seeking to resolve this was our motivation for the second part of this study, where we chose to explore the interplay between a different pair of timescales, namely σ^{-1} and τ_c. These results are discussed in the next section.

2.6.3 The Limit of Fast Fluctuations

In contrast to the inhomogeneously broadened (slow modulation) limit, we now discuss the case where the solvent fluctuations are sufficiently fast such that their dynamics play a role on an experimental timescale. In this case, the lineshape reflects not only the distribution of frequencies due to local solvent environments, but

also their time-dependent fluctuations [78]. In fact, the fluctuations are so rapid that each solute experiences only an averaged transition frequency [77]. Furthermore, the averaged frequency does not change much from solute to solute, since the fluctuations are statistically the same for each one[19]. This situation leads to a line shape that is narrower than the distribution of frequencies, a phenomenon known as "motional narrowing" [82, 83]. Thus the limit of homogeneous broadening, implies that the relaxation rate of the fluctuating solvent is much larger than the width of the distribution of frequencies visited by the ensemble of solutes, and corresponds to $1/\tau_c \gg \sigma$.

The line narrowing discussed above suggests that control may still be possible under certain conditions. More specifically, as the solvent fluctuations become increasingly more rapid, the solute has less time to sample different transition frequencies, and the more narrow the line becomes. In the limiting case of infinitely rapid fluctuations, the line shape would be infinitely narrow[20], since all solutes would experience the same unique transition frequency. Consequently, the underlying physics would be identical to the dephasing-free case discussed in §2.6.1, where control was possible over a wide region of the $(\alpha', \tilde{E}_0)$ parameter space. Within the context of our model, we chose as our starting point Figure 2.6e, where σ was clearly large enough to appreciably diminish control. The aim was to then systematically decrease the correlation time τ_c and to look for evidence of the motional narrowing limit and hence a regaining of control. The main results are displayed in Figure 2.7.

For large correlation times, $79 \lesssim \tau_c \lesssim 7900$, the population maps continue to resemble the inhomogeneously broadened case (Figure 2.6e) and can be understood in terms of the detuning arguments given in §2.6.2. For $\tau_c = 7.9$, both the transfer

[19] This is the origin of the term "homogeneous".

[20] Assuming no additional broadening mechanisms were at play.

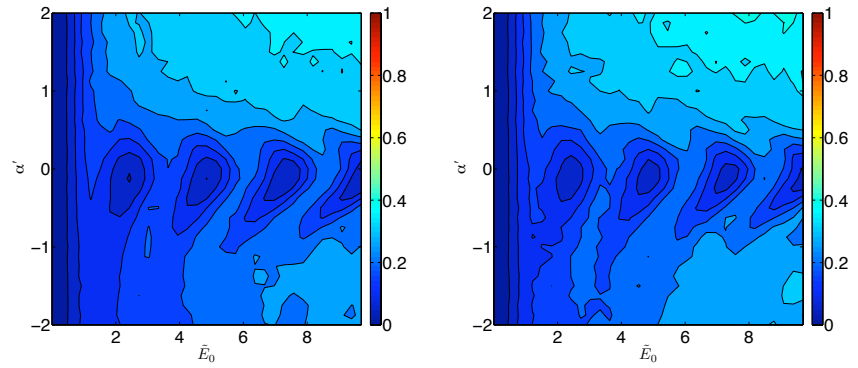

(a) $\tau_c = 7900$

(b) $\tau_c = 79$

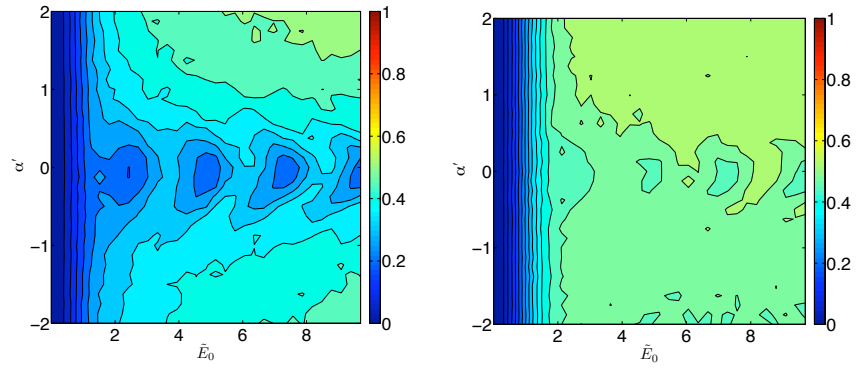

(c) $\tau_c = 7.9$

(d) $\tau_c = 0.79$

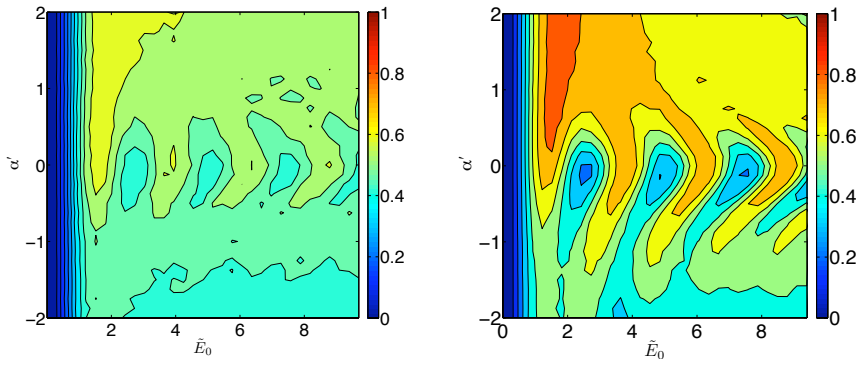

(e) $\tau_c = 0.079$

(f) $\tau_c = 0.016$

Figure 2.7: Population maps showing the approach to the homogeneously broadened (motional narrowing) limit. The fluctuation amplitude is $\sigma = 2$, and decreasing values of the solvent correlation time are shown in subfigures (a)-(f). All maps were averaged over 2000 realizations of the stochastic process to ensure convergence.

efficiency and the asymmetry between the positive chirp and negative chirp regimes begin to increase. For smaller values $0.79 \lesssim \tau_c \lesssim 0.016$, the asymmetry becomes increasingly more pronounced as the transfer efficiency increases, clearly illustrating the approach to the motional narrowing limit and thereby restoring the ability to control. It should be noted that this conclusion is not limited to the choice of $\sigma = 2$. The same effect is seen for larger values of σ as well, only τ_c must be decreased to a smaller value to see the emergence of the motional narrowing limit due to the criterion $1/\tau_c \gg \sigma$.

Since Figure 2.7d is where control appears to re-emerge, we can check the homogeneous limit $\sigma \ll 1/\tau_c$ and compare it with the experimentally measured values of Bardeen and Shank. The parameters in Figure 2.7d corresponds to $\tau_c = 25$fs and $\sigma = 200\text{cm}^{-1}$, and lead to a weak version of the homogenous limit, since $\sigma \approx 0.26 \times (1/\tau_c)$. The experimentally values $\tau_c = 20$fs and $\sigma = 200\text{cm}^{-1}$ also lead to a weak version of the homogeneous limit, since $\sigma \approx 0.12 \times (1/\tau_c)$. Although there were slight differences in our calculation compared to those in Cerullo, such as a longer pulse and a less shifted oscillator, the fact that the numbers above are similar gives gives credence to the claim that at least some control of LD690 is possible, even in the presence of dephasing. Also, our model has shown that the ability to control improves as τ_c is decreased. However, whether such small values are realizable experimentally is expected to be highly sensitive to the nature of the solute-solvent system under study.

2.7 Summary and Future Outlook

This chapter considered the coherent control of population transfer in the presence of pure dephasing in both the inhomogeneous and homogeneous limits. In the inho-

mogeneously broadened limit, $\sigma \gg 1/\tau_c$, it was found that the solvent-induced shift in transition frequency acted as a detuning of the laser from the vertical transition frequency of the chromophore. As σ was increased, the effect became pronounced and resulted in an overall decrease in the population transfer across the $(\alpha', \tilde{E}_0)$ parameter space. In the homogeneous limit, where $\sigma \ll 1/\tau_c$, it was found that, even for a relatively large value of σ, control could be regained provided the solvent correlation time τ_c was made small enough. This result suggested that at least some control should be possible in the presence of dephasing. Importantly, these claims were substantiated by comparison with experimentally measured values of σ and τ_c for the oxazine dye LD690.

Although the two-state model used in this study involved harmonic potentials, the methodology developed is general and easily lends itself to several future studies. For example, the extension to anharmonic potentials, and higher order chirp are straightforward, and would be useful for comparing to specific experimental systems. Also, the solvent effects could be incorporated in an alternative manner by using data attained by molecular dynamics simulations. Finally, the response function formalism could be extended to include an additional laser pulse, in order to study triggered 2DE experiments.

CHAPTER III

Methods for Calculating One- and Two-Dimensional Optical Spectra

3.1 Introduction

Multi-dimensional optical spectroscopy has established itself over the last decade as an extremely powerful and uniquely detailed probe of the structure and dynamics of molecular systems [25, 84–86]. It is also widely accepted that molecularly detailed and dynamically accurate models are necessary in order to take full advantage of these capabilities. However, accomplishing this objective requires overcoming a number of nontrivial theoretical and computational challenges, including the development of self-consistent dynamical methodologies for calculating spectra in complex systems which are both feasible and reliable.

Linear and nonlinear spectra are often expressed in terms of optical response functions (ORFs) [84]. However, a quantum-mechanically exact calculation of these ORFs is not feasible in most cases of practical interest. One approach for bypassing this problem is based on a cumulant expansion of the ORFs which is truncated at second order. Within this approach, one may cast the ORFs in terms of *equilibrium* frequency-frequency correlation functions which are presumably easier to calculate, either fully quantum-mechanically, semiclassically or classically.

Mixed quantum-classical methods, which are based on treating a small subset of

the degrees of freedom (DOF) quantum-mechanically while the rest are treated in a classical-like manner, represent another attractive strategy. However, as is well known, taking the classical limit of the ORFs with respect to a subset of DOF in a direct manner can lead to expressions which are not unique [42, 87–92]. Several approaches have been proposed in the past for obtaining self-consistent mixed quantum-classical expressions for the ORFs. One such approach is based on linearizing the path-integral forward-backward action associated with the photo-inactive DOF with respect to the difference between the forward and backward paths [42, 91, 93–97]. Within this approach, one calculates the ORFs by propagating the classical DOF *forward* in time along a classical trajectory that hops between potential surfaces corresponding to various quantum states of the chromophore, as dictated by the Liouville pathway associated with each ORF [42]. In what follows, we will refer to this approach as the *linearized semiclassical (LSC)* method. Another approach is based on replacing the product of quantum propagators that appears in the expressions for the ORFs by a *single* forward-backward semiclassical propagator [42, 91, 93, 98–103]. The partial cancellation of the forward and backward actions usually results in only mildly oscillatory integrands, which makes the calculation of the ORFs more manageable. In what follows, we will refer to this approach as the *forward-backward initial-value-representation (FB-IVR)* method.

The main goal of this chapter is to provide a meaningful benchmarking of these methods that will aid in assessing their robustness and reliability. To this end, we employ a benchmark model that consists of a two-state chromophore with shifted harmonic potential surfaces. For the sake of concreteness, we will assume that the transition between the two states is electronic. All four approximate methods can be shown to reproduce the exact results when the frequencies of the ground and

excited harmonic surfaces are identical. However, allowing for the ground and excited surfaces to differ in frequency leads to a more meaningful benchmark model for which none of the four approximate methods is exact.

We present comparisons of one- and two-dimensional spectra calculated via the above mentioned approximate methods to the corresponding exact spectra, as a function of various parameters, including the ratio of excited state to ground state frequencies, temperature, the displacement of the excited state potential relative to the ground state potential and the waiting time (see Figure 1.1) between the coherence periods in the case of two-dimensional spectra.

The remainder of this chapter is organized as follows. In §3.2, the theory of one- and two-dimensional optical spectra is presented, and §3.3 presents the benchmark model and its exact solution. In §3.4 and §3.5, two semiclassical approximations are presented, and in §3.6 and §3.7, two distinctly different types of second-order cumulant approximations are given. The results are presented and discussed in §3.8, and a summary and future outlook are provided in §3.9.

3.2 Theory of Optical Response for a Two-State System

3.2.1 Linear Response

The measurement of one-dimensional (1D) spectra is based on detecting the time-resolved linear response of the system to a single impulsive pulse at time $t = 0$. The signal can be shown to be proportional to the following linear ORF involving two-point time correlation functions of the transition dipole operator [84]:

$$\begin{aligned} J(t_1) &= \mathrm{Tr}\left[\hat{\mu}\left(t_1\right)\hat{V}\hat{\rho}_{eq}\right] \\ &= |\hat{\mu}_{ge}|^2 \mathrm{Tr}\left[e^{i\hat{H}_g t_1/\hbar} e^{-i\hat{H}_e t_1/\hbar}\hat{\rho}_g\right], \end{aligned} \tag{3.1}$$

where the second equality follows from the assumption that the system is in its ground equilibrium state prior to the arrival of the pulse, and by making the Condon approximation. Here, the trace is over the photo-inactive DOF, $\hat{\mu}_{ge}$ is the transition dipole moment (a constant within the Condon approximation), and $\hat{\rho}_g = e^{-\beta \hat{H}_g}/\mathrm{Tr}\left[e^{-\beta \hat{H}_g}\right]$ is the equilibrium ground state density operator, with $\beta = 1/k_B T$. The linear absorption spectrum is then defined as the frequency-domain analogue of $J(t_1)$ [84]:

$$I(\omega_1) = \mathrm{Re} \int_0^\infty dt_1 e^{-i\omega t_1} J(t_1) \ . \tag{3.2}$$

3.2.2 Nonlinear Response

The measurement of two-dimensional (2D) spectra is often based on detecting the time-resolved nonlinear response of the system to three sequential impulsive pulses with wave vectors $\mathbf{k}_a$, $\mathbf{k}_b$ and $\mathbf{k}_c$. The time delay between pulses a and b is denoted t_1, while that between pulses b and c is denoted t_2. The signal field is detected at a time interval t_3 after pulse c, in the background-free directions $\mathbf{k}_r = -\mathbf{k}_a + \mathbf{k}_b + \mathbf{k}_c$ and $\mathbf{k}_{nr} = \mathbf{k}_a - \mathbf{k}_b + \mathbf{k}_c$, corresponding to the *rephasing* and *nonrephasing* signals, respectively [86]. Assuming once again that the system is in its ground equilibrium state prior to the arrival of the first pulse and making the Condon approximation, the nonrephasing and rephasing signals can be shown to be proportional to the following third-order ORFs [84]:

$$\begin{aligned} R_{nr}(t_3, t_2, t_1) &= R_1(t_3, t_2, t_1) + R_4(t_3, t_2, t_1) \\ R_r(t_3, t_2, t_1) &= R_2(t_3, t_2, t_1) + R_3(t_3, t_2, t_1) \end{aligned} \tag{3.3}$$

respectively. The third-order ORFs $\{R_1, R_2, R_3, R_4\}$ are explicitly given by [84]:

$$\begin{aligned} R_1(t_3,t_2,t_1) &= \mathrm{Tr}\left[\hat{\mu}\left(t_1\right)\hat{\mu}\left(t_2+t_1\right)\hat{\mu}\left(t_3+t_2+t_1\right)\hat{\mu}\left(0\right)\hat{\rho}_{eq}\right] \\ &= |\hat{\mu}_{ge}|^4 \mathrm{Tr}\left[e^{i\hat{H}_g t_1/\hbar} e^{i\hat{H}_e t_2/\hbar} e^{i\hat{H}_g t_3/\hbar} e^{-i\hat{H}_e(t_1+t_2+t_3)/\hbar}\hat{\rho}_g\right] \\ &\equiv |\hat{\mu}_{ge}|^4 F(t_1, t_1+t_2, t_1+t_2+t_3, 0)\ , \end{aligned} \tag{3.4}$$

$$\begin{aligned} R_2(t_3,t_2,t_1) &= \mathrm{Tr}\left[\hat{\mu}\left(0\right)\hat{\mu}\left(t_2+t_1\right)\hat{\mu}\left(t_3+t_2+t_1\right)\hat{\mu}\left(t_1\right)\hat{\rho}_{eq}\right] \\ &= \hat{\mu}_{ge}|^4 \mathrm{Tr}\left[e^{i\hat{H}_e(t_1+t_2)/\hbar} e^{i\hat{H}_g t_3/\hbar} e^{-i\hat{H}_e(t_2+t_3)/\hbar} e^{-i\hat{H}_g t_1/\hbar}\hat{\rho}_g\right] \\ &\equiv |\hat{\mu}_{ge}|^4 F(0, t_1+t_2, t_1+t_2+t_3, t_1)\ , \end{aligned} \tag{3.5}$$

$$\begin{aligned} R_3(t_3,t_2,t_1) &= \mathrm{Tr}\left[\hat{\mu}\left(0\right)\hat{\mu}\left(t_1\right)\hat{\mu}\left(t_3+t_2+t_1\right)\hat{\mu}\left(t_2+t_1\right)\hat{\rho}_{eq}\right] \\ &= \hat{\mu}_{ge}|^4 \mathrm{Tr}\left[e^{i\hat{H}_e t_1/\hbar} e^{i\hat{H}_g(t_2+t_3)/\hbar} e^{-i\hat{H}_e t_3/\hbar} e^{-i\hat{H}_g(t_1+t_2)/\hbar}\hat{\rho}_g\right] \\ &\equiv |\hat{\mu}_{ge}|^4 F(0, t_1, t_1+t_2+t_3, t_1+t_2)\ , \end{aligned} \tag{3.6}$$

$$\begin{aligned} R_4(t_3,t_2,t_1) &= \mathrm{Tr}\left[\hat{\mu}\left(t_3+t_2+t_1\right)\hat{\mu}\left(t_2+t_1\right)\hat{\mu}\left(t_1\right)\hat{\mu}\left(0\right)\hat{\rho}_{eq}\right] \\ &= \hat{\mu}_{ge}|^4 \mathrm{Tr}\left[e^{i\hat{H}_g(t_1+t_2+t_3)/\hbar} e^{-i\hat{H}_e t_3/\hbar} e^{-i\hat{H}_g t_2/\hbar} e^{-i\hat{H}_e t_1/\hbar}\hat{\rho}_g\right] \\ &\equiv |\hat{\mu}_{ge}|^4 F(t_1+t_2+t_3, t_1+t_2, t_1, 0)\ , \end{aligned} \tag{3.7}$$

where,

$$F(\tau_1,\tau_2,\tau_3,\tau_4) = Tr\left[e^{-i\hat{H}_e(\tau_1-\tau_2)/\hbar} e^{-i\hat{H}_g(\tau_2-\tau_3)/\hbar} e^{-i\hat{H}_e(\tau_3-\tau_4)/\hbar} e^{-i\hat{H}_g(\tau_4-\tau_1)/\hbar}\hat{\rho}_g\right]\ . \tag{3.8}$$

Finally, the 2D spectrum at a given value of t_2 is defined as the absorptive part of the frequency-domain analogue, with respect to t_1 and t_3, of $R_{nr}(t_3,t_2,t_1)$ and $R_r(t_3,t_2,t_1)$ [86, 104, 105]:

$$I\left(\omega_3,t_2,\omega_1\right) \equiv \mathrm{Re}\int_0^\infty dt_1 \int_0^\infty dt_3 \left\{e^{i(\omega_1 t_1+\omega_3 t_3)} R_{nr}(t_3,t_2,t_1) + e^{i(-\omega_1 t_1+\omega_3 t_3)} R_r(t_3,t_2,t_1)\right\} \tag{3.9}$$

3.3 Benchmark Model and Exact Solutions

The main goal of this chapter is to provide a systematic analysis of the accuracy of the approximate methods discussed above. To be meaningful, the analysis has to be performed in the context of a benchmark model for which the exact quantum-mechanical ORFs are known and do not coincide with any of the approximations under discussion. A model that satisfies these requirements consists of a two-state chromophore where the ground and excited surfaces are harmonic *but differ in frequency*:

$$V_g(\hat{Q}) = \frac{1}{2}\omega_g^2\hat{Q}^2 \ ; \ V_e(\hat{Q}) = \hbar\omega_{eg} + \frac{1}{2}\omega_e^2(\hat{Q} + Q_d)^2 \ . \tag{3.10}$$

Here, ω_g and ω_e are the harmonic frequencies that correspond to the ground and excited surfaces, respectively, Q_d is the horizontal displacement of the excited state surface relative to the ground state surface and ω_{eg} is the minimum to minimum transition frequency between the ground state and excited state.

We first consider the special case where $\omega_e = \omega_g$, which corresponds to the one-dimensional version of the popular Brownian oscillator model [84]. As it turns out, this case does not lend itself as a benchmark for the problem at hand. This is because the ground and excited potential surfaces have the exact same shape and therefore induce the same dynamics. As a result, *the linear and third-order ORFs produced via all four approximations (FB-IVR, LSC, 2OC and 2OCa) can be shown to coincide with the exact ones when $\omega_e = \omega_g$, regardless of the values of the temperature and horizontal displacement* (see Appendix H). Thus, choosing a model system with $\omega_e \neq \omega_g$ is essential for obtaining a meaningful benchmark. It is important to note that the ORFs in the case $\omega_e \neq \omega_g$ differ from those in the case $\omega_e = \omega_g$ in two respects:

- The transition frequency is a quadratic rather than linear function of the coor-

dinate of the photo-inactive mode:

$$\hat{U} = \hbar\omega_{eg} + \frac{1}{2}\omega_e^2 Q_d^2 + \omega_e^2 Q_d \hat{Q} + \frac{1}{2}\left[\omega_e^2 - \omega_g^2\right]\hat{Q}^2 \ . \tag{3.11}$$

- The temporal behavior of $\hat{U}(t)$ is sensitive to whether it is governed by the ground or excited state potential surface, since the potentials in (3.10) lead to

$$\begin{aligned} \hat{Q}_g(t) &= \cos(\omega_g t)\hat{Q} + \frac{\sin(\omega_g t)}{m\omega_g}\hat{P} \\ \hat{Q}_e(t) &= Q_d\left[1 - \cos\left(\omega_e t\right)\right] + \cos(\omega_e t)\hat{Q} + \frac{\sin(\omega_e t)}{m\omega_e}\hat{P}. \end{aligned} \tag{3.12}$$

The exact quantum-mechanical ORFs when $\omega_e \neq \omega_g$ can be obtained in a variety of ways. Rather than working with the expressions given in §3.2.1 and 3.2.2, in this section we instead present the derivation in terms of an equivalent quantum Liouville space formulation. For example, the linear response function given in (3.2) is related to a more general response function by

$$S^{(1)}\left(t_1\right) \equiv \frac{i}{\hbar}\theta\left(t_1\right)\left\{J\left(t_1\right) - J^*\left(t_1\right)\right\} = \frac{i}{\hbar}\langle\langle\hat{\mu}|\,\mathbf{G}\left(t_1\right)\boldsymbol{\mu}\,|\hat{\rho}_{eq}\rangle\rangle \tag{3.13}$$

where bold symbols denote superoperators in the Liouville space, and capped symbols represent operators in the corresponding Hilbert space. Here, $\mathbf{G}$ and $\boldsymbol{\mu}$ are the field-free retarded Green's function and dipole superoperators[1], respectively, and $\hat{\mu}$ is the Hilbert space dipole operator defined as $\hat{\mu} = \sum_{j\neq k}\mu_{jk}\,|j\rangle\,\langle k|$. While the derivation below focuses on the exact linear ORF, the generalization to nonlinear ORFs is straightforward.

Using the Liouville space closure relation $\sum_{m,n}|m,n\rangle\rangle\langle\langle m,n| = 1$, where $|m,n\rangle\rangle \equiv |m\rangle\,\langle n|$ and $\{|j\rangle\}$ are energy eigenstates, the right side of (3.13) may be written as

$$\langle\langle\hat{\mu}|\,\mathbf{G}\left(t_1\right)\boldsymbol{V}\,|\hat{\rho}_{eq}\rangle\rangle = \sum_{j,k,m,n}\langle\langle\hat{\mu}|m,n\rangle\rangle\langle\langle m,n|\,\mathbf{G}\left(t_1\right)|j,k\rangle\rangle\langle\langle j,k|\,\boldsymbol{\mu}\,|\hat{\rho}_{eq}\rangle\rangle.$$

[1]Superoperators in Liouville space may equivalently thought of in term of their Hilbert space analogues. For example, $\mu \leftrightarrow [\hat{\mu},\cdot]$

(3.14)

Each of the three factors on the right side may be separately computed by way of Liouville space algebra as detailed in Appendix J. Using the equilibrium density operator $e^{-\beta\hat{H}}/Z$ and expressing the Hamiltonian in its eigenstate basis as $\hat{H} = \sum_j \varepsilon_j |j\rangle\langle j|$ leads to

$$\begin{aligned} \langle\langle \hat{\mu} | m,n \rangle\rangle &= \mu_{n,m} \\ \langle\langle j,k | \boldsymbol{\mu} | \hat{\rho}_{eq} \rangle\rangle &= \sum_m \frac{e^{-\beta\varepsilon_m}}{Z} \left(\mu_{jm}\delta_{k,m} - \mu_{mk}\delta_{j,m}\right), \end{aligned} \tag{3.15}$$

while using the fact that $\mathbf{G}(t_1) = \exp(-i\mathbf{L}t_1)$, where $\mathbf{L}$ is the Liouville superoperator, leads to

$$\langle\langle m,n | \mathbf{G}(t_1) | j,k \rangle\rangle = \exp\left[-i\left(\varepsilon_j - \varepsilon_k\right)t_1\right]\delta_{m,j}\delta_{n,k}. \tag{3.16}$$

Thus (3.14) becomes

$$\begin{aligned} \langle\langle \hat{\mu} | \mathbf{G}(t_1) \boldsymbol{\mu} | \hat{\rho}_{eq} \rangle\rangle &= \sum_{m,n,j,k} \mu_{nm} e^{-i\omega_{j,k}t_1}\delta_{m,j}\delta_{n,k} \sum_{m'} \frac{e^{-\beta\varepsilon_{m'}}}{Z}\left(\mu_{jm'}\delta_{k,m'} - \mu_{m'k}\delta_{j,m'}\right) \\ &= \sum_{j,k} \frac{e^{-\beta\varepsilon_k}}{Z}\mu_{kj}\mu_{jk}\left(e^{-i\omega_{j,k}t_1} - e^{i\omega_{j,k}t_1}\right) \\ &= J(t_1) - J^*(t_1) \end{aligned} \tag{3.17}$$

where $\omega_{j,k} \equiv (\varepsilon_j - \varepsilon_k)/\hbar$ are the transition frequencies and

$$J(t_1) = \sum_{j,k} \frac{e^{-\beta\varepsilon_k}}{Z}\mu_{kj}\mu_{jk}\exp\left(-i\omega_{j,k}t_1\right). \tag{3.18}$$

To adapt this expression to the benchmark model considered here, we must specify the form of $\hat{\rho_{eq}}$ and interpret the energy eigenstates as vibronic states. The two-state dipole operator in the vibronic basis defined in (1.7) was

$$\hat{\mu} = \hat{\mu}_{ge}\sum_{gj,ek} |gj\rangle\langle ek| S_{gj,ek} + \hat{\mu}_{eg}\sum_{gj,ek} |ek\rangle\langle gj| S_{ek,gj} \tag{3.19}$$

Further, for harmonic potentials and the assumption that the initial state is the lowest vibrational state on the ground electronic surface, the energy levels and partition function are given by $\varepsilon_j = \hbar\omega_g\,(j+1/2)$ and $Z^{-1} = 2\sinh\left(\beta\hbar\omega_g/2\right)$, respectively, so that the equilibrium density operator becomes

$$\begin{aligned}\frac{e^{-\beta\varepsilon_j}}{Z} &= 2\sinh\left(\beta\hbar\omega_g/2\right)\exp\left[-\beta\hbar\omega_g\,(j+1/2)\right] \\ &= \exp\left(-\beta\hbar\omega_g j\right)\left[1-\exp\left(-\beta\hbar\omega_g\right)\right] \end{aligned} \tag{3.20}$$

With these considerations, the exact linear ORF has the form

$$J(t_1) = |\hat{\mu}_{ge}|^2 \sum_{j_0,j_1} P^{eq}_{gj_0} S_{gj_0,ej_1} S_{ej_1,gj_0} \exp\left[-i\omega_{ej_1,gj_0} t_1\right] \tag{3.21}$$

where $P^{eq}_{gj} = [1-\exp(-\hbar\omega_g/k_BT)]\exp(-j\hbar\omega_g/k_BT)$ is the equilibrium probability for being in state $|gj\rangle$, and $\omega_{aj,bk} = \omega_{eg}[\delta(a,e)-\delta(b,e)] + [(j+1/2)\omega_a - (k+1/2)\omega_b]$ are the vibronic transition frequencies.

Similarly, the expression for the exact nonlinear ORFs may obtained from the general response function

$$\begin{aligned} S^{(3)}\left(t_3,t_2,t_1\right) &\equiv \left(\frac{i}{\hbar}\right)^3 \theta\left(t_1\right)\theta\left(t_2\right)\theta\left(t_3\right) \sum_{\alpha=1}^{4} \left\{R_\alpha\left(t_3,t_2,t_1\right) - R^*_\alpha\left(t_3,t_2,t_1\right)\right\} \\ &= \left(\frac{i}{\hbar}\right)^3 \left\langle\left\langle \hat{\mu}\right|\mathbf{G}\left(t_3\right)\boldsymbol{\mu}\mathbf{G}\left(t_2\right)\boldsymbol{\mu}\mathbf{G}\left(t_1\right)\boldsymbol{\mu}\left|\rho_{eq}\right\rangle\right\rangle, \end{aligned} \tag{3.22}$$

and leads to

$$R_1(t_3,t_2,t_1) = |\hat{\mu}_{ge}|^4 \sum_{j_0,j_1,j_2,j_3} P^{eq}_{gj_0} S_{gj_3,ej_1} S_{ej_1,gj_0} S_{gj_0,ej_2} S_{ej_2,gj_3} \times \tag{3.23}$$

$$\exp\left[-i\omega_{ej_1,gj_3}t_3 - i\omega_{ej_1,ej_2}t_2 - i\omega_{ej_1,gj_0}t_1\right]$$

$$R_2(t_3,t_2,t_1) = |\hat{\mu}_{ge}|^4 \sum_{j_0,j_1,j_2,j_3} P^{eq}_{gj_0} S_{gj_3,ej_2} S_{ej_2,gj_0} S_{gj_0,ej_1} S_{ej_1,gj_3} \times \tag{3.24}$$

$$\exp\left[-i\omega_{ej_2,gj_3}t_3 - i\omega_{ej_2,ej_1}t_2 + i\omega_{ej_1,gj_0}t_1\right]$$

$$R_3(t_3,t_2,t_1) = |\hat{\mu}_{ge}|^4 \sum_{j_0,j_1,j_2,j_3} P^{eq}_{gj_0} S_{ej_3,gj_0} S_{gj_0,ej_1} S_{ej_1,gj_2} S_{gj_2,ej_3} \times \tag{3.25}$$

$$\exp\left[-i\omega_{ej_3,gj_2}t_3 - i\omega_{gj_0,gj_2}t_2 + i\omega_{ej_1,gj_0}t_1\right] \ ,$$

$$R_4(t_3,t_2,t_1) = |\hat{\mu}_{ge}|^4 \sum_{j_0,j_1,j_2,j_3} P^{eq}_{gj_0} S_{ej_3,gj_2} S_{gj_2,ej_1} S_{ej_1,gj_0} S_{gj_0,ej_3} \times \tag{3.26}$$

$$\exp\left[-i\omega_{ej_3,gj_0}t_3 - i\omega_{gj_2,gj_0}t_2 + i\omega_{ej_3,gj_0}t_1\right]$$

It should be noted that the ORFs above are *purely oscillatory*. However, in reality, these ORFs are damped by processes such as electronic dephasing. In order to account for pure electronic dephasing, we assume that ω_{eg} is a stochastic quantity whose dynamics is uncorrelated with that of the photo-inactive mode and can be described as a Gaussian process in the limit of motional narrowing. Within these assumptions,

$$\begin{aligned} J(t_1) &\rightarrow \exp\left(-\Gamma t_1\right) J(t_1) \qquad (3.27)\\ R_j(t_1,t_2,t_3) &\rightarrow \exp[-\Gamma(t_1-t_3)] R_j(t_1,t_2,t_3) \quad (j=2,3)\\ R_j(t_1,t_2,t_3) &\rightarrow \exp[-\Gamma(t_1+t_3)] R_j(t_1,t_2,t_3) \quad (j=1,4) \end{aligned}$$

where Γ is the electronic dephasing rate constant. Numerical implementation of the above ORFs is straightforward, where the number of terms included in each summation is determined by convergence of the corresponding spectra. Convergence was typically obtained by allowing each index to range from 0 to 10.

The fact the dephasing rate constant enters as a multiplicative damped exponential can be substantiated on more mathematical grounds, and will be illustrated in the context of linear response for the sake of clarity. Rather than starting with (3.13), we begin the equivalent form of the linear response of a two-state system in (3.2)

$$J(t_1) = |\mu_{ge}|^2 \langle \hat{U}_g^\dagger(t_1) \hat{U}_e(t_1) \rangle, \tag{3.28}$$

where $\hat{U}_{g/e}(t_1) = e^{-i\hat{H}_{g/e}t_1/\hbar}$ are the time evolution operators corresponding to the time-independent Hamiltonians $\hat{H}_{g/e}$ in (1.3). If the energy gap between the electronic surfaces begins to fluctuate in time due to the interaction with the environments, then $\omega_{eg} \rightarrow \omega_{eg}(t) = \langle \omega_{eg} \rangle + \delta\omega_{eg}(t)$, where $\langle \ldots \rangle$ corresponds to an average over the distribution of $\delta\omega_{eg}$. Assuming the stochastic process is stationary implies that the average $\langle \omega_{eg} \rangle$ is time independent, and without loss of generality may be chosen as $\langle \omega_{eg} \rangle = 0$. Thus the Hamiltonian becomes explicitly time-dependent:

$$\hat{H} = \hat{H}_g \left| g \right\rangle \left\langle g \right| + \left(\hat{H}_e + \langle \omega_{eg} \rangle + \delta\omega_{eg}(t) \right) \left| e \right\rangle \left\langle e \right| \ . \tag{3.29}$$

The linear response still has the form of (3.28) with $\hat{U}_g(t_1) = e^{-i\hat{H}_g t_1/\hbar}$, but now

$$\hat{U}_e(t_1) = \exp\left[-\frac{i}{\hbar} \int_0^{t'} dt' \left(\hat{H}_e + \langle \omega_{eg} \rangle + \delta\omega_{eg}(t') \right) \right] \tag{3.30}$$

(see (E.7) of Appendix E) so that

$$\overline{J}(t_1) = e^{-i\int_0^{t_1} dt' \delta\omega_{eg}(t')} J(t_1) \tag{3.31}$$

Since $\delta\omega_{eg}(t)$ is a stochastic process, we must average over its realizations. Making use of the second-order cumulant expansion in Appendix F leads to

$$\langle e^{-i\int_0^{t_1} dt' \delta\omega_{eg}(t')} \rangle = e^{-g(t_1)} \tag{3.32}$$

where $g(t_1) = \int_0^{t_1} d\tau\,(t-\tau)\,\langle \delta\omega_{eg}(\tau)\,\delta\omega_{eg}\rangle$. In the case where the fluctuations are exponentially correlated, $\langle \delta\omega_{eg}(t)\,\delta\omega_{eg}\rangle = \sigma^2 e^{-t/\tau_c}$, where τ_c and σ are the correlation time and fluctuation amplitude, respectively, and

$$g(t) = \sigma^2\tau_c^2\left[t/\tau_c - \left(1-e^{-t/\tau_c}\right)\right]. \tag{3.33}$$

For timescales that are long relative to τ_c,

$$\overline{J}(t_1) = e^{-g(t_1)}J(t_1) \overset{t/\tau_c\gg 1}{\longrightarrow} e^{-\sigma^2\tau_c t_1}J(t_1) \tag{3.34}$$

so that $\overline{J}(t_1)$ decays exponentially with a time constant $\sigma^2\tau_c$. Thus the long time behavior will dominate $\overline{J}(t_1)$ when $1/\sigma^2\tau_c \gg \tau_c$, or $\sigma \ll 1/\tau_c$ and corresponds to the limit of *homogenous broadening* (see §2.5.1).

Finally,

$$\overline{J}(t_1) = e^{-\Gamma t_1}J(t_1) \tag{3.35}$$

where the dephasing rate constant[2] is defined as $\Gamma \equiv \sigma^2\tau_c$. A similar procedure may be applied for the nonlinear response functions, and leads to (3.27).

3.4 Forward-Backward Initial-Value Representation Method (FB-IVR)

Within the FB-IVR approximation, one assumes that the overall forward-backward time propagators in Eqs. (3.2) and (3.4)-(3.7) can be replaced by the corresponding *single* semiclassical Herman-Kluk propagator [106, 107], so that:

$$J^{FB-IVR}(t_1) = |\mu_{ge}|^2\frac{1}{2\pi\hbar}\int dQ_0 dP_0\, D(P_0,Q_0)\langle g_{P_0,Q_0}|\hat{\rho}_g|g_{P_f,Q_f}\rangle e^{\frac{i}{\hbar}S_J(P_0,Q_0)}\ , \tag{3.37}$$

[2]The relation $\Gamma \equiv \sigma^2\tau_c$ may be derived using Redfield theory in the homogeneously broadened limit.

and

$$R_j^{FB-IVR}(t_3,t_2,t_1) = |\mu_{ge}|^4 \frac{1}{2\pi\hbar}\int dQ_0 dP_0\, D(P_0,Q_0)\langle g_{P_0,Q_0}|\hat{\rho}_g|g_{P_f,Q_f}\rangle e^{\frac{i}{\hbar}S_{R_j}(P_0,Q_0)}\ ,\ j=1,2,3,4\ . \tag{3.38}$$

where $\{Q_f, P_f\}$ denote the position and momenta at the final time. Here, $|g_{P_jQ_j}\rangle$ is a coherent state of width γ which is centered at (P_j, Q_j) and corresponds to the wave function

$$\langle Q|g_{P_j,Q_j}\rangle = \left(\frac{\gamma}{\pi}\right)^{1/4}\exp\left(-\frac{1}{2}\gamma(Q-Q_j)^2 + \frac{i}{\hbar}P_j(Q-Q_j)\right)\ , \tag{3.39}$$

$D(P_0,Q_0)$ is the Herman-Kluk prefactor,

$$D(P_0,Q_0) = \frac{1}{\sqrt{2}}\left(\frac{\partial P_f}{\partial P_0} + \frac{\partial Q_f}{\partial Q_0} - i\hbar\gamma\frac{\partial Q_f}{\partial P_0} + i(\hbar\gamma)^{-1}\frac{\partial P_f}{\partial Q_0}\right)^{\frac{1}{2}}\ , \tag{3.40}$$

and $\{S_J(P_0,Q_0), S_{R_j}(P_0,Q_0)\}$ are the forward-backward actions which are explicitly given by:

$$S_J(Q_0,P_0) = \int_0^{t_1} d\tau L_e(Q_\tau,P_\tau) + \int_{t_1}^0 d\tau L_g(Q_\tau,P_\tau)\ , \tag{3.41}$$

$$\begin{aligned}
S_{R_1}(Q_0,P_0) &= \int_0^{t_1+t_2+t_3} d\tau L_e(Q_\tau,P_\tau) + \int_{t_1+t_2+t_3}^{t_1+t_2} d\tau L_g(Q_\tau,P_\tau) \\
&\quad + \int_{t_1+t_2}^{t_1} d\tau L_e(Q_\tau,P_\tau) + \int_{t_1}^0 d\tau L_g(Q_\tau,P_\tau)\ , \\
S_{R_2}(Q_0,P_0) &= \int_0^{t_1} d\tau L_g(Q_\tau,P_\tau) + \int_{t_1}^{t_1+t_2+t_3} d\tau L_e(Q_\tau,P_\tau) \\
&\quad + \int_{t_1+t_2+t_3}^{t_1+t_2} d\tau L_g(Q_\tau,P_\tau) + \int_{t_1+t_2}^0 d\tau L_e(Q_\tau,P_\tau)\ , \\
S_{R_3}(Q_0,P_0) &= \int_0^{t_1+t_2} d\tau L_g(Q_\tau,P_\tau) + \int_{t_1+t_2}^{t_1+t_2+t_3} d\tau L_e(Q_\tau,P_\tau) \\
&\quad + \int_{t_1+t_2+t_3}^{t_1} d\tau L_g(Q_\tau,P_\tau) + \int_{t_1}^0 d\tau L_e(Q_\tau,P_\tau)\ , \\
S_{R_4}(Q_0,P_0) &= \int_0^{t_1} d\tau L_e(Q_\tau,P_\tau) + \int_{t_1}^{t_1+t_2} d\tau L_g(Q_\tau,P_\tau) \\
&\quad + \int_{t_1+t_2}^{t_1+t_2+t_3} d\tau L_e(Q_\tau,P_\tau) + \int_{t_1+t_2+t_3}^0 d\tau L_g(Q_\tau,P_\tau)\ ,
\end{aligned} \tag{3.42}$$

where $L_{g/e}(Q,P) = T(P) - V_{g/e}$ is the classical Lagrangian and $T(P)$ is the kinetic energy. In the case of the linear ORF, Q_τ and P_τ are calculated along a classical trajectory that starts at Q_0 and P_0 at $\tau = 0$, is propagated forward in time from $\tau = 0$ to $\tau = t_1$ on the excited state potential, and then backward in time from $\tau = t_1$ to $\tau = 0$ on the ground state potential (see Eq. (3.2)). In the case of the third-order ORFs, Q_τ and P_τ are calculated along classical trajectories that start at Q_0 and P_0 at $\tau = 0$, and are propagated forward in time from $\tau = 0$ to $\tau = t_1 + t_2 + t_3$ followed by backward propagation from $\tau = t_1 + t_2 + t_3$ to $\tau = 0$. Importantly, the system hops between the ground and excited potential surfaces throughout this forward-backward time evolution in a manner implied by Eqs. (3.4-3.7). Since it is well known that semiclassical propagators have rapidly oscillating phases [108–111], a key advantage of the FB-IVR method is that the backward propagation step results in extensive cancellation which leads to an action that is generally small. This results in a semiclassical phase which is slowly varying and much more amenable to efficient numerical calculation [112].

Obtaining expressions for J^{FB-IVR} and R_j^{FB-IVR} required the use of a computer algebra system[3], since the three factors appearing in the integrands of Eqns. (3.38) and (3.37) are algebraically cumbersome to compute.

To illustrate the procedure, the calculation of each factor is outlined below, focusing on R_2^{FB-IVR} for the sake of concreteness. Computing the *total* forward-backward action appearing in the factor $e^{\frac{i}{\hbar}S_{R_2}(P_0,Q_0)}$ requires propagating the classical trajectories in four stages, as illustrated in Figure 3.1. For each stage, the propagation is carried out on either the ground or excited state potentials, according to the appro-

[3]Wolfram Research, Inc., Mathematica, version 7.0, Champaign, IL (2009).

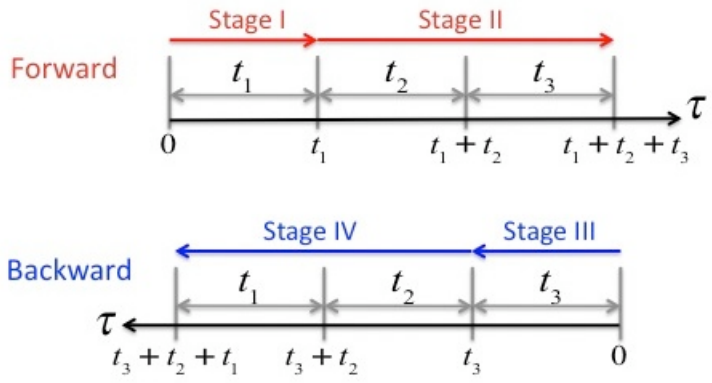

Figure 3.1: Propagation pathway for classical trajectories of R_2 in the FB-IVR method. For Stages I and II, the trajectories are propagated forward in time, while for Stages III and IV they are propagated backward in time. Stages I and III on on the ground state potential, while Stages II and IV are on the excited potential.

priate solutions to Hamilton's equations of motion, given by

$$\begin{aligned} Q(t) &= \cos(\omega_g t)Q_0 + \frac{\sin(\omega_g t)}{m\omega_g}P_0 \\ P(t) &= -m\omega_g \sin(\omega_g t)Q_0 + \cos(\omega_g t)P_0, \end{aligned} \tag{3.43}$$

for propagation on the ground state V_g, and

$$\begin{aligned} Q(t) &= -Q_d + (Q_d + Q_0)\cos(\omega_e t) + \frac{\sin(\omega_e t)}{m\omega_e}P_0 \\ P(t) &= -m\omega_e (Q_d + Q_0)\sin(\omega_e t) + \cos(\omega_e t)P_0. \end{aligned} \tag{3.44}$$

for propagation on the excited state V_e. The sequential propagation implies that the initial conditions for stages II-IV come from the position and momenta at the end of the previous stage. It should also be noted that the time origin for the backward propagation is chosen as in Figure 3.1, and consequently the equations of motion for the backward stages are the same as those in (3.43) and (3.44) except $t \to -t$. Propagation of each classical trajectory proceeds as follows:

1. Stage I: Propagate forward on V_g during the interval $(0, t_1)$

$$Q_I(\tau) = \cos(\omega_g \tau) Q_0 + \frac{\sin(\omega_g \tau)}{m\omega_g} P_0 \tag{3.45}$$

$$P_I(\tau) = -m\omega_g \sin(\omega_g \tau) Q_0 + \cos(\omega_g \tau) P_0$$

$$L_g\left(Q_I(\tau), P_I(\tau)\right) = T\left(P_I(\tau)\right) - V_g\left(Q_I(\tau)\right)$$

where $Q_I(\tau)|_{\tau=t_1}$ and $P_I(\tau)|_{\tau=t_1}$ serve as initial conditions for Stage II.

2. Stage II: Propagate forward on V_e during the interval $(t_1, t_1 + t_2 + t_3)$

$$Q_{II}(\tau) = -Q_d + \left(Q_d + Q_I(t_1)\right) \cos\left[\omega_e(\tau - t_1)\right] + \frac{\sin\left[\omega_e(\tau - t_1)\right]}{m\omega_e} P_I(t_1) \tag{3.46}$$

$$P_{II}(\tau) = -m\omega_e \left(Q_d + Q_I(t_1)\right) \sin\left[\omega_e(\tau - t_1)\right] + \cos\left[\omega_e(\tau - t_1)\right] P_I(t_1)$$

$$L_e\left(Q_{II}(\tau), P_{II}(\tau)\right) = T\left(P_{II}(\tau)\right) - V_e\left(Q_{II}(\tau)\right)$$

where $Q_{II(\tau)|_{\tau=t_1+t_2+t_3}}$ and $P_{II}(\tau)|_{\tau=t_1+t_2+t_3}$ serve as initial conditions for Stage III.

3. Stage III: Propagate backward on V_g during the interval $(0, t_3)$

$$Q_{III}(\tau) = \cos(\omega_g \tau) Q_{II}(t_1 + t_2 + t_3) - \frac{\sin(\omega_g \tau)}{m\omega_g} P_{II}(t_1 + t_2 + t_3) \tag{3.47}$$

$$P_{III}(\tau) = m\omega_g \sin(\omega_g \tau) Q_{II}(t_1 + t_2 + t_3) + \cos(\omega_g \tau) P_{II}(t_1 + t_2 + t_3)$$

$$L_g\left(Q_{III}(\tau), P_{III}(\tau)\right) = T\left(P_{III}(\tau)\right) - V_g\left(Q_{III}(\tau)\right)$$

where $Q_{III}(\tau)|_{\tau=t_3}$ and $P_{III}(\tau)|_{\tau=t_3}$ serve as initial conditions for Stage IV.

4. Stage IV: Propagate backward on V_e during the interval $(t_3, t_3 + t_2 + t_1)$

$$Q_{IV}(\tau) = -Q_d + \left(Q_d + Q_{III}(t_3)\right) \cos\left[\omega_e(\tau - t_3)\right] - \frac{\sin\left[\omega_e(\tau - t_3)\right.}{m\omega_e} P_{III}(t_3) \tag{3.48}$$

$$P_{IV}(\tau) = m\omega_e \left(Q_d + Q_{III}(t_3)\right) \sin\left[\omega_e(\tau - t_3) + \cos\left[\omega_e(\tau - t_3) P_{III}(t_3)\right.\right.\right.$$

$$L_e\left(Q_{IV}(\tau), P_{IV}(\tau)\right) = T\left(P_{IV}(\tau)\right) - V_e\left(Q_{IV}(\tau)\right)$$

Once the Lagrangians for each stage are known, the total action $S_{R_2}(Q_0, P_0)$ from (3.41) may be written as[4]

$$S_{R_2}(Q_0,P_0) = \int_0^{t_1} d\tau L_g\left(Q_I(\tau), P_I(\tau)\right) + \int_{t_1}^{t_1+t_2+t_3} d\tau L_e\left(Q_{II}(\tau), P_{II}(\tau)\right)$$
$$- \int_0^{t_3} d\tau L_g\left(Q_{III}(\tau), P_{III}(\tau)\right) - \int_{t_3}^{t_3+t_2+t_1} d\tau L_e\left(Q_{IV}(\tau), P_{IV}(\tau)\right) \tag{3.49}$$

The fact that $V_{g/e}$ are harmonic potentials implies that $S_{R_2}(Q_0, P_0)$ is a *quadratic* function of the initial conditions $\{Q_0, P_0\}$, making $e^{\frac{i}{\hbar}S_{R_2}(P_0,Q_0)}$ a Gaussian function of those variables.

The Herman-Kluk prefactor is computed according to (3.40), using the position and momenta at the end of the forward-backward propagation

$$D(P_0,Q_0) = \frac{1}{\sqrt{2}}\left(\frac{\partial P_{IV}(t_3+t_2+t_1)}{\partial P_0} + \frac{\partial Q_{IV}(t_3+t_2+t_1)}{\partial Q_0}\right. \tag{3.50}$$
$$\left. - i\hbar\gamma\frac{\partial Q_{IV}(t_3+t_2+t_1)}{\partial P_0} + i(\hbar\gamma)^{-1}\frac{\partial P_{IV}(t_3+t_2+t_1)}{\partial Q_0}\right)^{\frac{1}{2}}$$

The appearance of the complex square root in (3.50) deserves attention, since care must be taken to ensure that the appropriate branch is chosen [113]. In our application, it is sufficient to require the phase of the prefactor to be a continuous function of the initial conditions $\{Q_0, P_0\}$ [114]. The resulting function is quadratic in those variables, so that multiplication by the prefactor amounts to multiplying by a complex Gaussian. It should also be noted that since the benchmark model considered here includes only a single photoinactive DOF, the resulting phase space is two-dimensional. As a result, the prefactor does not create a substantial computational bottleneck. However, for systems with more degrees of freedom, the prefactor has a more general form involving the determinant of a stability matrix, $D(\mathbf{P}_0, \mathbf{Q}_0) = \sqrt{\det\mathbf{M}}$. Computation of the prefactor can become prohibitively expensive, especially when the DOF are coupled [99].

[4]The minus signs and integration limits of the last two terms differ from those in (3.41) due to the choice of time origin for the backward propagation. The two expressions are equivalent.

The last step in forming the integrand in (3.37) is to find the matrix element of the density operator between two coherent states. To this end, we use the coordinate closure relation $\int |Q\rangle \langle Q| = 1$ to write

$$\langle g_{P_0,Q_0}|\hat{\rho}_g|g_{P_f,Q_f}\rangle = \int dQdQ' \langle g_{P_0,Q_0}|Q\rangle \langle Q|\, \hat{\rho}_g\, |Q'\rangle \langle Q'|\, g_{P_f,Q_f}\rangle. \tag{3.51}$$

Using the definition of the coherent state wavefunctions in (3.39), and the following identity for the density operator matrix element [115]

$$\langle Q|\, \hat{\rho}_g\, |Q'\rangle = \exp\left[-A\left(Q^2 + Q'^2\right) + BQQ'\right], \tag{3.52}$$

where $A \equiv \frac{m\omega_g}{2\hbar}\coth\left(\beta\hbar\omega_g\right)$, $B \equiv \frac{m\omega_g}{\hbar}\sinh\left(\beta\hbar\omega_g\right)^{-1}$, and $\beta = \left(k_B T\right)^{-1}$ is the inverse temperature, leads to

$$\langle g_{P_0,Q_0}|\hat{\rho}_g|g_{P_f,Q_f}\rangle = \tag{3.53}$$
$$\sqrt{\frac{\gamma}{\pi}}\int dQdQ' e^{-\frac{1}{2}\gamma(Q-Q_0)^2 - \frac{i}{\hbar}P_0(Q-Q_0)} e^{-A\left(Q^2+Q'^2\right)+BQQ'} e^{-\frac{1}{2}\gamma(Q'-Q_f)^2 + \frac{i}{\hbar}P_f(Q'-Q_f)}.$$

The integration is over Gaussian functions of Q and Q', and results in another Gaussian function of $\{Q_0, P_0\}$.

Thus, each of the factors in the integrand in (3.38) is a Gaussian function of the initial conditions, rendering the phase space integrals analytically computable[5].

3.5 Linearized Semiclassical Method (LSC)

The LSC approximation is based on writing the ORFs in a path integral form and linearizing the path-integral forward-backward action with respect to the difference between the forward and backward paths [42, 91, 94–97, 116–119]. It should be noted that the same approximation has been previously derived via a variety of other semiclassical approaches [88, 110, 111, 120–127]. This section provides an

[5]Numerical integration would be required in the case for anharmonic potentials.

overview of the main features of the method, while Appendix I provides a more detailed mathematical derivation.

Within this approximation, the linear and third-order ORFs are given by the following expressions involving integrals over a classical-like phase space:

$$J^{LSC}(t_1) = |\mu_{ge}|^2 \frac{1}{2\pi\hbar} \int dQ_0 dP_0 \, \hat{\rho}_{g,W}(Q_0, P_0) \exp\left\{ i \int_0^{t_1} d\tau U(Q_\tau)/\hbar \right\} \ , \tag{3.54}$$

and

$$R_j^{LSC}(t_3, t_2, t_1) = |\mu_{ge}|^4 \frac{1}{2\pi\hbar} \int dQ_0 dP_0 \hat{\rho}_{g,W}(Q_0, P_0) e^{-i\int_0^{t_1} d\tau U(Q_\tau)/\hbar} e^{\mp i \int_{t_1+t_2}^{t_1+t_2+t_3} d\tau U(Q_\tau)/\hbar} \tag{3.55}$$

Here, + and − correspond to rephasing ORFs (R_2, R_3) and nonrephasing ORFs (R_1, R_4), respectively, $\hat{\rho}_{g,W}(Q, P)$ is an operator in the electronic Hilbert space obtained by the partial Wigner transform [128, 129] of $\hat{\rho}_g$ with respect to the nuclear DOF

$$\hat{\rho}_{g,W}(Q, P) = \int d\Delta e^{-iP\Delta/\hbar} \langle Q + \frac{\Delta}{2} | \hat{\rho}_g | Q - \frac{\Delta}{2} \rangle \ , \tag{3.56}$$

and $U(Q_\tau)/\hbar$ is the instantaneous value of the transition frequency,

$$U(Q_\tau) = V_e(Q_\tau) - V_g(Q_\tau) = \omega_e^2 Q_d Q(\tau) + \frac{1}{2}\left(\omega_e^2 - \omega_g^2\right) Q^2(\tau) \tag{3.57}$$

Importantly, $\{Q_\tau\}$ are classical trajectories whose initial conditions $\{Q_0, P_0\}$ are sampled from the ground state distribution $\hat{\rho}_{g,W}(Q_0, P_0)$, and which "hop" between potential surfaces as dictated by the Liouville pathway associated with each ORF. This hopping reflects *nonequilibrium dynamics on multiple potential surfaces* [97], and should be contrasted with several other methods which were limited to equilibrium ground state dynamics [42, 84, 88, 91, 101, 102, 130, 131].

In the LSC method, the trajectories are propagated *forward* in time from $\tau = 0$ to $\tau = t_{1+}t_2 + t_3$, where the choice of potential surface used during a given time

interval is determined by the desired ORF. This is llustrated schematically in Figure 3.2, and outlined in the following prescription:

- In the case of J, the propagation takes place on the average potential surface, $V_{ge} = (V_g + V_e)/2$, during the interval $(0, t_1)$.
- In the case of R_1 and R_2, the propagation takes place on V_{ge} during $(0, t_1)$, on the *excited* state potential surface, V_e, during $(t_1, t_1 + t_2)$, and again on V_{ge} during $(t_1 + t_2, t_1 + t_2 + t_3)$.
- In the case of R_3 and R_4, the propagation takes place on V_{ge} during $(0, t_1)$, on the *ground* state potential surface, V_g, during $(t_1, t_1 + t_2)$, and again on V_{ge} during $(t_1 + t_2, t_1 + t_2 + t_3)$.

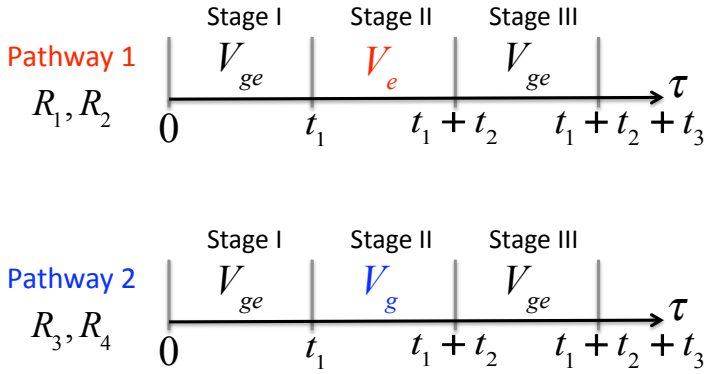

Figure 3.2: Propagation (Liouville) pathways for classical trajectories in the LSC method, where Stages I,II,III refer to the time intervals $(0, t_1)$, $(t_1, t_1 + t_2)$ and $(t_1 + t_2, t_1 + t_2 + t_3)$, respectively. The pathways differ only in Stage II: Pathway 1 propagates trajectories on the excited state potential, whereas pathway 2 propagates them on the ground state potential.

Obtaining specific expressions for J^{LSC} and R_j^{LSC} required the use of a computer algebra system[6], and involved solutions to Hamilton's classical equations of motion on each of the three surfaces. For propagation on the ground state V_g,

$$\begin{aligned} Q(t) &= \cos(\omega_g t) Q_0 + \frac{\sin(\omega_g t)}{m\omega_g} P_0 \\ P(t) &= -m\omega_g \sin(\omega_g t) Q_0 + \cos(\omega_g t) P_0, \end{aligned} \tag{3.58}$$

[6]Wolfram Research, Inc., Mathematica, version 7.0, Champaign, IL (2009).

for propagation on the excited state V_e,

$$\begin{aligned} Q(t) &= -Q_d + (Q_d + Q_0)\cos(\omega_e t) + \frac{\sin(\omega_e t)}{m\omega_e} P_0 \\ P(t) &= -m\omega_e (Q_d + Q_0)\sin(\omega_e t) + \cos(\omega_e t) P_0, \end{aligned} \tag{3.59}$$

and for propagation on the average potential V_{ge},

$$\begin{aligned} Q(t) &= -D_d + (D_d + Q_0)\cos(\Omega t) + \frac{\sin(\Omega t)}{m\Omega} P_0 \\ P(t) &= -m\Omega (D_d + Q_0)\sin(\Omega t) + \cos(\Omega t) P_0, \end{aligned} \tag{3.60}$$

where $D_d \equiv \omega_e^2 Q_d / \left(\omega_e^2 + \omega_g^2\right)$ and $\Omega^2 = \left(\omega_e^2 + \omega_g^2\right)/2$. The numerical evaluation steps may be summarized as follows:

1. Using the equilibrium ground state density operator for a harmonic oscillator, $\hat{\rho}_g = Z_g^{-1} e^{-\beta \hat{H}_g} = 2\sinh(\beta\hbar\omega_g/2)\, e^{-\beta \hat{H}_g}$, compute its Wigner transform:

$$\begin{aligned} \hat{\rho}_{g,W}(Q_0, P_0) &= \frac{1}{2\pi\hbar} Z_g^{-1} \int_{-\infty}^{\infty} d\Delta e^{-iP\Delta/\hbar} \langle Q_0 + \frac{\Delta}{2} | e^{-\beta \hat{H}_g(Q_0, P_0)} | Q_0 - \frac{\Delta}{2} \rangle \\ &= \frac{1}{\pi\hbar} \tanh(\beta\hbar\omega_g/2)\, e^{-\alpha P_0^2 - \gamma Q_0^2} \end{aligned} \tag{3.61}$$

   where $\alpha \equiv \frac{1}{m\hbar\omega_g} \tanh(\beta\hbar\omega_g/2)$ and $\gamma \equiv \frac{m\omega_g}{\hbar} \tanh(\beta\hbar\omega_g/2)$.

2. Stage I: Propagate for time interval $(0, t_1)$ on V_{ge}

$$\begin{aligned} Q_I(\tau) &= -D_d + (D_d + Q_0)\cos(\Omega\tau) + \frac{\sin(\Omega\tau)}{m\Omega} P_0 \\ P_I(\tau) &= -m\Omega (D_d + Q_0)\sin(\Omega\tau) + \cos(\Omega\tau) P_0, \end{aligned} \tag{3.62}$$

   where $Q_I(\tau)|_{\tau=t_1}$ and $P_I(\tau)|_{\tau=t_1}$ serve as initial conditions for Stage II.

3. Stage II (pathway 1): Propagate for time interval $(t_1, t_1 + t_2)$ on V_e

$$\begin{aligned} Q_{II}^{(1)}(\tau) &= -Q_d + [Q_d + Q_I(t_1)]\cos[\omega_e(\tau - t_1)] + \frac{\sin[\omega_e(\tau - t_1)]}{m\omega_e} P_I(t_1) \\ P_{II}^{(1)}(\tau) &= -m\omega_e [Q_d + Q_I(t_1)]\sin[\omega_e(\tau - t_1)] + \cos[\omega_e(\tau - t_1)] P_I(t_1), \end{aligned} \tag{3.63}$$

Stage II (pathway 2): Propagate for time interval (t_1, t_1+t_2) on V_g

$$\begin{aligned} Q_{II}^{(2)}(\tau) &= \cos\left[\omega_g(\tau-t_1)\right] Q_I(t_1) + \frac{\sin\left[\omega_g(\tau-t_1)\right]}{m\omega_g} P_I(t_1) \\ P_{II}^{(2)}(\tau) &= -m\omega_g \sin\left[\omega_g(\tau-t_1)\right] Q_I(t_1) + \cos\left[\omega_g(\tau-t_1)\right] P_I(t_1) \end{aligned} \tag{3.64}$$

where $Q_{II}^{(1/2)}(\tau)|_{\tau=t_1+t_2}$ and $P_{II}^{(1/2)}(\tau)|_{\tau=t_1+t_2}$ serve as initial conditions for Stage III.

4. Stage III: Propagate for time interval $(t_1+t_2, t_1+t_2+t_3)$ on V_{ge}

$$\begin{aligned} Q_{III}^{(1/2)}(\tau) &= -D_d + \left[D_d + Q_{II}^{(1/2)}(t_1+t_2)\right] \cos\left[\Omega(\tau-t_1-t_2)\right] \\ &+ \frac{\sin\left[\Omega(\tau-t_1-t_2)\right]}{m\Omega} P_{II}^{(1/2)}(t_1+t_2) \end{aligned} \tag{3.65}$$

Using the path-dependent transition frequency $U(Q_\tau)$ from (3.57), the integrand in (3.54) becomes

$$e^{-\alpha P_0^2 - \gamma Q_0^2} \exp\left[-\frac{i}{\hbar}\int_0^{t_1} d\tau U\left(Q_I(\tau)\right)\right] \exp\left[\mp\frac{i}{\hbar}\int_{t_1+t_2}^{t_1+t_2+t_3} d\tau U\left(Q_{III}^{(1/2)}(\tau)\right)\right] \tag{3.66}$$

Since the argument of each exponential in (3.66) is a quadratic function of the initial conditions $\{Q_0, P_0\}$, integration of their product over $\{Q_0, P_0\}$ amounts to evaluating Gaussian integrals, which can be computed analytically.

Thus appropriate choice of sign $\mp$ and pathway (1/2) in the right factor leads to explicit expressions for the ORFs.

It should be noted that in the absence of nonadiabatic coupling, as in the benchmark model studied here, the LSC method is equivalent to a formulation of optical response based on Mixed Quantum-Classical Liouville (MQCL) dynamics [132]. To this end, let the state of the system be described by a density operator, $\hat{\rho}(t)$, whose time evolution is dictated by the quantum Liouville equation:

$$\frac{d}{dt}\hat{\rho}(t) = -\frac{i}{\hbar}\left[\hat{H}(t), \hat{\rho}(t)\right] \ . \tag{3.67}$$

Without any loss of generality, this equation may be recast in a Wigner representation by describing the state of the system as in (3.56), Wigner transforming the Hamiltonian by

$$\hat{H}_W(Q,P) = \int d\Delta e^{-iP\Delta/\hbar} \langle Q + \frac{\Delta}{2} | \hat{H}(t) | Q - \frac{\Delta}{2} \rangle \ . \tag{3.68}$$

This leads to the MQCL equation describing the dynamics of $\hat{\rho}_{g,W}(Q_0, P_0; t)$

$$\begin{aligned} \frac{\partial}{\partial t}\hat{\rho}_W(Q_0,P_0;t) &= -\frac{i}{\hbar}\left[\hat{H}_W\left(Q_0,P_0;t\right), \hat{\rho}_W\left(Q_0,P_0;t\right)\right] \\ &+ \frac{1}{2}\left(\left\{\hat{H}_W\left(Q_0,P_0;t\right), \hat{\rho}_W\left(Q_0,P_0;t\right)\right\} - \left\{\hat{\rho}_W\left(Q_0,P_0;t\right), \hat{H}_W\left(Q_0,P_0;t\right)\right\}\right), \end{aligned} \tag{3.69}$$

where $\{f, g\}$ denotes the Poisson bracket of the functions $f\left(Q,P,t\right)$ and $g\left(Q,P,t\right)$. Further, we may project this equation onto a basis $\{|\alpha\left(Q_0\right)\rangle\}$ where the electronic states follow the nuclear DOF adiabatically, so that the matrix elements are given by

$$\rho_W^{\alpha,\alpha'}\left(Q_0,P_0;t\right) = \langle \alpha\left(Q_0\right)| \hat{\rho}_W\left(Q_0,P_0;t\right) |\alpha\left(Q_0\right)\rangle \tag{3.70}$$

The resulting equations of motion [133–139] dictate that the phase space densities $\rho_{g,W}^{\alpha,\alpha'}\left(Q_0,P_0;t\right)$ associated with the the density matrix elements $\rho_{\alpha,\alpha'}$ are to be propagated classically and independently from one another on the corresponding potential surfaces. More specifically, for a two-electronic state system, the phase space densities associated with ρ_{ge} and ρ_{eg} are to be propagated on the *average* potential, $V_{ge} = (V_g + V_e)/2$. This method is advantageous in the sense that it provides a rigorous route for deriving mixed quantum-classical expressions for the ORFs that are able to capture the effects of nonequilibrium dynamics.

3.6 Standard Second Order Cumulant Method (2OC)

The 2OC approximation can be derived by taking advantage of the following identity [84]:

$$\exp\left[i\hat{H}_g t/\hbar\right]\exp\left[-i\hat{H}_e t/\hbar\right] = \exp_+\left[-\frac{i}{\hbar}\int_0^t dt'\hat{U}_g(t')\right] \ . \tag{3.71}$$

Here, $\exp_+$ corresponds to a positively time-ordered exponential and

$$\hat{U}_g(t) = \exp\left[i\hat{H}_g t/\hbar\right]\hat{U}\exp\left[-i\hat{H}_g t/\hbar\right] \tag{3.72}$$

where $\hat{U}/\hbar =$ is the transition frequency operator from (3.11).

Substituting (I.12) into (3.2) yields the following expression for the linear ORF:

$$J(t_1) = |\mu_{ge}|^2 \mathrm{Tr}\left\{\exp_+\left[-\frac{i}{\hbar}\int_0^{t_1} dt'\hat{U}_g(t')\right]\hat{\rho}_g\right\} \equiv |\mu_{ge}|^2\langle\exp_+\left[-\frac{i}{\hbar}\int_0^{t_1} dt'\hat{U}_g(t')\right]\rangle_g \ . \tag{3.73}$$

Importantly, the initial equilibrium state, $\hat{\rho}_g$, and the dynamics of $\hat{U}_g(t)$ are both governed by the *same* Hamiltonian, $\hat{H}_g$. Finding the 2OC approximation then amounts to replacing the average on the right side of (3.73) by its corresponding second-order cumulant expansion and truncating at second order.

To find the approximation, we begin by expanding the right side of (3.73) according to the procedure outlined in Appendix F

$$\begin{aligned}
&\langle\exp_+\left[-\lambda\frac{i}{\hbar}\int_0^t dt'\hat{U}_g(t')\right]\rangle_g \\
&\quad = 1 - \lambda\frac{i}{\hbar}\int_0^{t_1} d\tau_1\langle\hat{U}_g(\tau_1)\rangle_g - \lambda^2\frac{1}{\hbar^2}\int_0^{t_1} d\tau_2\int_0^{\tau_2} d\tau_1\left\langle U_g(\tau_2)U_g(\tau_1)\right\rangle_g + \ldots \\
&\quad = 1 + \lambda C_1 + \lambda^2\left(C_2 + \frac{1}{2}C_1^2\right) + \ldots
\end{aligned} \tag{3.74}$$

Equating powers of λ up to second order and using the fact that the equilibrium

average $\langle \ldots \rangle_g$ implies $\left[e^{\pm i\hat{H}_g t/\hbar}, \hat{\rho}_g\right] = 0$ leads to[7]

$$C_1 = \frac{i}{\hbar}\int_0^{t_1} d\tau_1 \langle \hat{U}_g(\tau_1)\rangle_g = \frac{i}{\hbar}\langle \hat{U}\rangle_g t_1 \tag{3.75}$$

and

$$\begin{aligned} C_2 + \frac{1}{2}C_1^2 &= -\frac{1}{\hbar^2}\int_0^{t_1} d\tau_2 \int_0^{\tau_2} d\tau_1 \left\langle U_g(\tau_2)U_g(\tau_1)\right\rangle_g \\ &= -\frac{1}{\hbar^2}\int_0^{t_1} d\tau_2 \int_0^{\tau_2} d\tau_1 \left\langle U_g(\tau_2-\tau_1)U_g\right\rangle_g \\ &= -\frac{1}{\hbar^2}\int_0^{t_1} d\tau \left(t_1-\tau\right)\left\langle U_g\left(\tau\right)U_g\right\rangle_g \end{aligned} \tag{3.76}$$

where the last line follows from a change of variables $(\tau_1, \tau_2) \rightarrow (\tau_1 - \tau_2, \tau_2)$. Thus the expression for the linear ORF is

$$J^{2OC}(t_1) = |\mu_{ge}|^2 \exp\left[-i\langle \hat{U}\rangle_g t_1/\hbar - g(t_1)\right] \ . \tag{3.77}$$

Here

$$g(t_1) = \int_0^{t_1} d\tau (t_1-\tau) C_g(\tau) \ , \tag{3.78}$$

and $C_g(\tau)$ is the quantum-mechanical equilibrium ground-state frequency-frequency correlation function:

$$C_g(\tau) = \frac{1}{\hbar^2}\left[\langle \hat{U}_g(\tau)\hat{U}\rangle_g - \langle \hat{U}\rangle_g^2\right] \ . \tag{3.79}$$

The fact that $C_g\left(\tau\right)$ is the only required input for computing $J^{2OC}(t_1)$ implies that the temporal behavior of the linear ORF within the 2OC approximation reflects *equilibrium fluctuations on the ground state surface*. This behavior should be contrasted with the exact expression for $J(t_1)$ in (3.2), as well as the corresponding FB-IVR and LSC approximations (Eq. (3.37) and (3.54), respectively), which are clearly affected by nonequilibrium dynamics on the excited state surface. The discrepancy can be traced back to the choice of Eq. (3.71) as the starting point for

[7] More generally, $\left[f\left(\hat{H}_g\right), \hat{\rho}_g\right] = 0$ where f is any analytic function of $\hat{H}_g$.

the second-order cumulant approximation. As will be shown in §3.7, an alternative and equally valid identity may be used which leads to an alternative second-order cumulant approximation that is sensitive to nonequilibrium excited state dynamics.

The 2OC approximations for the third-order ORFs can be obtained in a similar manner. They can be conveniently expressed in terms of $F(\tau_1, \tau_2, \tau_3, \tau_4)$, Eq. (3.8), whose 2OC approximation is given by:[84]

$$F^{2OC}(\tau_1, \tau_2, \tau_3, \tau_4) = e^{i\langle\hat{U}\rangle_g(-\tau_1+\tau_2-\tau_3+\tau_4)/\hbar}\times \tag{3.80}$$
$$\exp\left\{-\frac{1}{\hbar^2}\left[g(\tau_1-\tau_2)-g(\tau_1-\tau_3)+g(\tau_1-\tau_4)+g(\tau_2-\tau_3)-g(\tau_2-\tau_4)+g(\tau_3-\tau_4)\right]\right\}$$

Thus, within the 2OC approximation, the temporal behavior of the third-order ORF reflects the very same equilibrium fluctuations on the ground state surface as the linear ORF.

Numerical implementation of the expressions J^{2OC} and F^{2OC} required the use of a computer algebra system[8] to obtain the input $g(t_1)$, as outlined in the following steps:

- Using the the time evolution of the position operator from (3.12), find the *ground state* time evolution of the transition frequency operator

$$\begin{aligned} \hat{Q}_g(t) &= \cos(\omega_g t)\hat{Q} + \frac{\sin(\omega_g t)}{m\omega_g}\hat{P} \\ \hat{U}_g(t) &= \omega_e^2 Q_d \hat{Q}_g(t) + \frac{1}{2}\left(\omega_e^2 - \omega_g^2\right)\hat{Q}_g^2(t) \end{aligned} \tag{3.81}$$

[8] Wolfram Research, Inc., Mathematica, version 7.0, Champaign, IL (2009).

- Compute the transition frequency average and time correlation function

$$\begin{aligned}\langle U\rangle_g/\hbar &= \frac{1}{2\hbar}\left(\omega_e^2-\omega_g^2\right)\left[B^2(t)\langle\hat{Q}^2\rangle_g + C^2(t)\langle\hat{P}^2\rangle_g\right]\\ \langle U_g(t)\,U\rangle_g/\hbar^2 &= \left(\frac{\omega_e^2 Q_d}{\hbar}\right)^2\left[B(t)\langle\hat{Q}^2\rangle_g + C(t)\langle\hat{P}\hat{Q}\rangle_g\right]\\ &+\frac{1}{2\hbar^2}\left(\omega_e^2-\omega_g^2\right)\left\{\begin{array}{l} B^2(t)\langle\hat{Q}^4\rangle_g + C^2(t)\langle\hat{P}^2\hat{Q}^2\rangle_g\\ +B(t)C(t)\left[\langle\hat{Q}\hat{P}\hat{Q}^2\rangle_g + \langle\hat{P}\hat{Q}^3\rangle_g\right]\end{array}\right\}\end{aligned} \tag{3.82}$$

  where $B(t)\equiv\cos(\omega_g t)$ and $C(t)\equiv\sin(\omega_g t)/m\omega_g$. The temperature dependence is contained in the expectation values $\langle\ldots\rangle_g$, whose explicit expressions are given in Appendix G.

- Compute the time integrals in (3.78) (analytically) to obtain the input $g(t_1)$, and find the time-domain linear response $J^{2OC}(t_1)$ and nonlinear rephasing and nonrephasing signals $R_r(t_3,t_2,t_1), R_{nr}(t_3,t_2,t_1)$ according to (3.77) and (3.3).

Finally, it should be noted that J^{2OC} and F^{2OC} are still fully quantum-mechanical, since no semiclassical approximation has been employed. However, truncating the cumulant expansion at second order represents a rather severe approximation which can be expected to limit the accuracy of the resulting expression for the ORFs.

3.7 Alternative Second Order Cumulant Method (2OCa)

The second-order cumulant expansions in Eqs. (3.77) and (3.80) are not unique. To see this, let us consider an alternative cumulant expansion based on the following identity:

$$\exp\left[i\hat{H}_g t/\hbar\right]\exp\left[-i\hat{H}_e t/\hbar\right] = \exp_-\left[-i\int_0^t dt'\hat{U}_e(t')/\hbar\right]\ . \tag{3.83}$$

Here, $\exp_-$ corresponds to a negatively time-ordered exponential and

$$\hat{U}_e(t) = \exp\left[i\hat{H}_e t/\hbar\right]\hat{U}\exp\left[-i\hat{H}_e t/\hbar\right]\ . \tag{3.84}$$

Substituting (3.83) into (3.2) yields the following expression for the linear ORF:

$$J(t_1) = |\mu_{ge}|^2 \mathrm{Tr}\left\{ \exp_-\left[-\frac{i}{\hbar}\int_0^{t_1} dt' \hat{U}_e(t') \right] \hat{\rho}_g \right\} \equiv |\mu_{ge}|^2 \langle \exp_-\left[-\frac{i}{\hbar}\int_0^{t_1} dt' \hat{U}_e(t') \right] \rangle_g \ . \tag{3.85}$$

An alternative second-order cumulant approximation can then be obtained by performing the cumulant expansion of the right side of (3.85)

$$\begin{aligned} &\langle \exp_-\left[-\lambda\frac{i}{\hbar}\int_0^{t} dt' \hat{U}_e(t') \right] \rangle_g \\ &\quad = 1 - \lambda\frac{i}{\hbar}\int_0^{t_1} d\tau_1 \langle \hat{U}_e(\tau_1) \rangle_g - \lambda^2 \frac{1}{\hbar^2}\int_0^{t_1} d\tau_2 \int_0^{\tau_2} d\tau_1 \left\langle U_e(\tau_1) U_e(\tau_2) \right\rangle_g + \ldots \\ &\quad = 1 + \lambda C_1 + \lambda^2 \left(C_2 + \frac{1}{2} C_1^2 \right) + \ldots \end{aligned} \tag{3.86}$$

where the time ordering in the integrand of the λ^2 term is opposite to that of the (3.74). Equating powers of λ up to second order leads to

$$\begin{aligned} C_1 &= \frac{i}{\hbar}\int_0^{t_1} d\tau_1 \langle \hat{U}_e(\tau_1) \rangle_g \\ C_2 + \frac{1}{2} C_1^2 &= -\frac{1}{\hbar^2}\int_0^{t_1} d\tau_2 \int_0^{\tau_2} d\tau_1 \left\langle U_e(\tau_1) U_e(\tau_2) \right\rangle_g \end{aligned} \tag{3.87}$$

and yields the following expression for the linear ORF

$$\begin{aligned} J^{2OCa}(t_1) &= |\mu_{ge}|^2 \exp\left[-\frac{i}{\hbar}\int_0^{t_1} d\tau_1 \langle \hat{U}_e(\tau_1) \rangle_g \right. \\ &\quad \left. -\frac{1}{\hbar^2}\left\{ \int_0^{t_1} d\tau_2 \int_0^{\tau_2} d\tau_1 \langle \hat{U}_e(\tau_1) \hat{U}_e(\tau_2) \rangle_g - \frac{1}{2}\left(\int_0^{t_1} d\tau_1 \langle \hat{U}_e(\tau_1) \rangle_g \right)^2 \right\} \right] \ . \end{aligned} \tag{3.88}$$

Importantly, while the initial equilibrium state, $\hat{\rho}_g$, is governed by the ground state Hamiltonian, the dynamics of $\hat{U}_e(t)$ are governed by the excited state Hamiltonian.

It should be emphasized that although the expressions for the linear ORF in Eqs. (3.73) and (3.85) are equivalent, the corresponding second-order cumulant expansions in (3.77) and (3.88) are not. More specifically, unlike $\langle \hat{U} \rangle_g / \hbar$ and $C_g(t)/\hbar^2$ which correspond to the averaged transition frequency and fluctuations around it,

respectively, at equilibrium on the ground state surface, the quantities $\langle \hat{U}_e(\tau_1)\rangle_g$ and $\langle \hat{U}_e(\tau_1)\hat{U}_e(\tau_2)\rangle_g$ reflect the *nonequilibrium dynamics of the transition frequency on the excited state surface* and its autocorrelation. In other words, unlike the 2OC approximation, and similarly to the FB-IVR and LSC approximations, the 2OCa approximation appears to be able to account for the signature of the inherent nonequilibrium excited state dynamics on the linear ORF.

The 2OCa approximation for $F(\tau_1,\tau_2,\tau_3,\tau_4)$, and thereby the third-order ORFs, can be obtained in a similar manner:

$$F^{2OCa}(\tau_1,\tau_2,\tau_3,\tau_4) = \exp\left[C_1(\tau_1,\tau_2,\tau_3,\tau_4) + C_2(\tau_1,\tau_2,\tau_3,\tau_4)\right] \ , \tag{3.89}$$

where $C_1(\tau_1,\tau_2,\tau_3,\tau_4)$ and $C_2(\tau_1,\tau_2,\tau_3,\tau_4)$ are the first and second order cumulants, explicitly given by:

$$\begin{aligned} C_1(\tau_1,\tau_2,\tau_3,\tau_4) = \frac{i}{\hbar} \quad & \left\{ -\int_0^{\tau_1} d\tau_1' \langle \hat{U}_e\left(\tau_1'\right)\rangle_g + \int_0^{\tau_2} d\tau_2' \langle \hat{U}_e\left(\tau_2'\right)\rangle_g \right. \\ & \left. - \int_0^{\tau_3} d\tau_3' \langle \hat{U}_e\left(\tau_3'\right)\rangle_g + \int_0^{\tau_4} d\tau_4' \langle \hat{U}_e\left(\tau_4'\right)\rangle_g \right\} \end{aligned} \tag{3.90}$$

and

$$C_2(\tau_1,\tau_2,\tau_3,\tau_4) \tag{3.91}$$

$$\begin{aligned} = \ & -\frac{1}{\hbar^2}\left\{ \int_0^{\tau_1} d\tau_1' \int_0^{\tau_1'} d\tau_1'' \langle \hat{U}_e\left(\tau_1''\right)\hat{U}_e\left(\tau_1'\right)\rangle_g + \int_0^{\tau_2} d\tau_2' \int_0^{\tau_2'} d\tau_2'' \langle \hat{U}_e\left(\tau_2''\right)\hat{U}_e\left(\tau_2'\right)\rangle_g \right. \\ & + \int_0^{\tau_3} d\tau_3' \int_0^{\tau_3'} d\tau_3'' \langle \hat{U}_e\left(\tau_3''\right)\hat{U}_e\left(\tau_3'\right)\rangle_g + \int_0^{\tau_4} d\tau_4' \int_0^{\tau_4'} d\tau_4'' \langle \hat{U}_e\left(\tau_4''\right)\hat{U}_e\left(\tau_4'\right)\rangle_g \\ & + \int_0^{\tau_1} d\tau_1' \int_0^{\tau_2} d\tau_2' \langle \hat{U}_e\left(\tau_1'\right)\hat{U}_e\left(\tau_2'\right)\rangle_g - \int_0^{\tau_1} d\tau_1' \int_0^{\tau_3} d\tau_3' \langle \hat{U}_e\left(\tau_1'\right)\hat{U}_e\left(\tau_3'\right)\rangle_g \\ & + \int_0^{\tau_1} d\tau_1' \int_0^{\tau_4} d\tau_4' \langle \hat{U}_e\left(\tau_1'\right)\hat{U}_e\left(\tau_4'\right)\rangle_g + \int_0^{\tau_2} d\tau_2' \int_0^{\tau_3} d\tau_3' \langle \hat{U}_e\left(\tau_2'\right)\hat{U}_e\left(\tau_3'\right)\rangle_g \\ & \left. - \int_0^{\tau_2} d\tau_2' \int_0^{\tau_4} d\tau_4' \langle \hat{U}_e\left(\tau_2'\right)\hat{U}_e\left(\tau_4'\right)\rangle_g + \int_0^{\tau_3} d\tau_3' \int_0^{\tau_4} d\tau_4' \langle \hat{U}_e\left(\tau_3'\right)\hat{U}_e\left(\tau_4'\right)\rangle_g \right\} \\ & - \frac{1}{2} C_1^2(\tau_1,\tau_2,\tau_3,\tau_4) \end{aligned} \tag{3.92}$$

Numerical implementation of the expressions J^{2OCa} and F^{2OCa} is similar to that of J^{2OC} and F^{2OC}, only the algebra is substantially more cumbersome. The procedure is outlined as follows

- Find the *excited state* time evolution of the position operator by solving Heisenberg's equation of motion, and use it to find the time evolution of the transition frequency operator:

$$\begin{aligned} \hat{Q}_e(t) &= Q_d\left[1-\cos\left(\omega_e t\right)\right]+\cos(\omega_e t)\hat{Q}+\frac{\sin(\omega_e t)}{m\omega_e}\hat{P} \\ \hat{U}_e(t) &= \omega_e^2 Q_d \hat{Q}_e(t)+\frac{1}{2}\left(\omega_e^2-\omega_g^2\right)\hat{Q}_e^2(t) \end{aligned} \tag{3.93}$$

- Compute the transition frequency average and time correlation function

$$\left\langle U_e\left(t\right)\right\rangle_g = -\omega_e^2 Q_d A\left(t\right)+\frac{1}{2}\left(\omega_e^2-\omega_g^2\right)\left[A^2\left(t\right)+B^2\left(t\right)\left\langle\hat{Q}^2\right\rangle_g+C^2\left(\tau\right)\left\langle\hat{P}^2\right\rangle_g\right]$$

$$\begin{aligned} \left\langle U_e\left(\tau_1\right)U_e\left(\tau_2\right)\right\rangle_g &= f_1\left(\tau_1,\tau_2\right)+f_2\left(\tau_1,\tau_2\right)\left\langle\hat{Q}^2\right\rangle_g+f_3\left(\tau_1,\tau_2\right)\left\langle\hat{P}^2\right\rangle_g \\ &+f_4\left(\tau_1,\tau_2\right)\left\langle\hat{Q}\hat{P}\right\rangle_g+f_5\left(\tau_1,\tau_2\right)\left\langle\hat{P}\hat{Q}\right\rangle_g \\ &+\frac{1}{2}\left(\omega_e^2-\omega_g^2\right)\left\{\begin{array}{l} B^2\left(\tau_1\right)B^2\left(\tau_2\right)\left\langle\hat{Q}^4\right\rangle_g+C^2\left(\tau_1\right)C^2\left(\tau_2\right)\left\langle\hat{P}^2\right\rangle_g \\ +B^2\left(\tau_1\right)C^2\left(\tau_2\right)\left\langle\hat{Q}^2\hat{P}^2\right\rangle_g+C^2\left(\tau_1\right)B^2\left(\tau_2\right)\left\langle\hat{P}^2\hat{Q}^2\right\rangle_g \\ +B\left(\tau_1\right)C\left(\tau_1\right)B\left(\tau_2\right)C\left(\tau_2\right)\left[\begin{array}{l}\left\langle\hat{Q}\hat{P}\hat{Q}\hat{P}\right\rangle_g+\left\langle\hat{Q}\hat{P}^2\hat{Q}\right\rangle_g \\ +\left\langle\hat{P}\hat{Q}\hat{P}\hat{Q}\right\rangle_g+\left\langle\hat{P}\hat{Q}^2\hat{P}\right\rangle_g\end{array}\right] \\ +B^2\left(\tau_1\right)B\left(\tau_2\right)C\left(\tau_2\right)\left[\left\langle\hat{Q}^3\hat{P}\right\rangle_g+\left\langle\hat{Q}^2\hat{P}\hat{Q}\right\rangle_g\right] \\ +B\left(\tau_1\right)C\left(\tau_1\right)B^2\left(\tau_2\right)\left[\left\langle\hat{Q}\hat{P}\hat{Q}^2\right\rangle_g+\left\langle\hat{P}\hat{Q}^3\right\rangle_g\right] \\ +C^2\left(\tau_1\right)B\left(\tau_2\right)C\left(\tau_2\right)\left[\left\langle\hat{P}^2\hat{Q}\hat{P}\right\rangle_g+\left\langle\hat{P}^3\hat{Q}\right\rangle_g\right] \\ +B\left(\tau_1\right)C\left(\tau_1\right)C^2\left(\tau_2\right)\left[\left\langle\hat{Q}\hat{P}^3\right\rangle_g+\left\langle\hat{P}\hat{Q}\hat{P}^2\right\rangle_g\right] \end{array}\right\} \end{aligned} \tag{3.94}$$

where $A\left(t\right)\equiv\left[1-\cos\left(\omega_e t\right)\right]$, $B\left(t\right)\equiv\cos\left(\omega_e t\right)$ and $C\left(t\right)\equiv\sin\left(\omega_e t\right)/m\omega_e$, where the expectation values $\left\langle\ldots\right\rangle_g$ are given in Appendix G. The time-dependent

coefficients $f_1(\tau_1,\tau_2) - f_5(\tau_1,\tau_2)$ are given by

$$\begin{aligned}
f_1(\tau_1,\tau_2) &\equiv c_1^2 A^2(\tau_1) A^2(\tau_2) - c_1 c_2 A^2(\tau_1) A(\tau_2) \\
&\quad - c_1 c_2 A(\tau_1) A^2(\tau_2) + c_2^2 A(\tau_2) A(\tau_1) \\
f_2(\tau_1,\tau_2) &\equiv c_1^2 A^2(\tau_1) B^2(\tau_2) + 4c_1^2 A(\tau_1) B(\tau_1) A(\tau_2) B(\tau_2) \\
&\quad - 2c_1 c_2 A(\tau_1) B(\tau_1) B(\tau_2) + c_1^2 B^2(\tau_1) A^2(\tau_2) - c_1 c_2 A(\tau_2) B^2(\tau_1) \\
&\quad - c_1 c_2 A(\tau_1) B^2(\tau_2) + c_2^2 B(\tau_1) B(\tau_2) - 2c_1 c_2 B(\tau_1) A(\tau_2) B(\tau_2) \\
f_3(\tau_1,\tau_2) &\equiv c_1^2 A^2(\tau_1) C^2(\tau_2) + 4c_1^2 A(\tau_1) C(\tau_1) A(\tau_2) C(\tau_2) \\
&\quad - 2c_1 c_2 A(\tau_1) C(\tau_1) C(\tau_2) + c_1^2 C^2(\tau_1) A^2(\tau_2) - c_1 c_2 A(\tau_2) C^2(\tau_1) \\
&\quad - c_1 c_2 A(\tau_1) C^2(\tau_2) + c_2^2 C(\tau_1) C(\tau_2) - 2c_1 c_2 C(\tau_1) A(\tau_2) C(\tau_2) \\
f_4(\tau_1,\tau_2) &\equiv c_1^2 A^2(\tau_1) B(\tau_2) C(\tau_2) + 4c_1^2 A(\tau_1) B(\tau_1) A(\tau_2) C(\tau_2) \\
&\quad - 2c_1 c_2 A(\tau_1) B(\tau_1) C(\tau_2) + c_1^2 B(\tau_1) C(\tau_1) A^2(\tau_2) \\
&\quad - c_1 c_2 A(\tau_2) B(\tau_1) C(\tau_1) - c_1 c_2 A(\tau_1) B(\tau_2) C(\tau_2) \\
&\quad - 2c_1 c_2 B(\tau_1) A(\tau_2) C(\tau_2) + c_2^2 B(\tau_1) C(\tau_2) \\
f_5(\tau_1,\tau_2) &\equiv c_1^2 A^2(\tau_1) C(\tau_2) B(\tau_2) + 4c_1^2 A(\tau_1) C(\tau_1) A(\tau_2) B(\tau_2) \\
&\quad - 2c_1 c_2 A(\tau_1) C(\tau_1) B(\tau_2) + c_1^2 C(\tau_1) B(\tau_1) A^2(\tau_2) \\
&\quad - c_1 c_2 A(\tau_2) C(\tau_1) B(\tau_1) - c_1 c_2 A(\tau_1) C(\tau_2) B(\tau_2) \\
&\quad - 2c_1 c_2 C(\tau_1) A(\tau_2) B(\tau_2) + c_2^2 C(\tau_1) B(\tau_2)
\end{aligned} \tag{3.95}$$

where $c_1 \equiv \omega_e^2 Q_d$ and $c_2 \equiv \frac{1}{2}\left(\omega_e^2 - \omega_g^2\right)$.

- Compute the time integrals in (3.94) to find $J^{2OCa}(t_1)$ via (3.88) and $R_r(t_3,t_2,t_1), R_{nr}(t_3,t_2,t_1)$ via (3.89) and (3.3).

3.8 Results and Discussion

Exact and approximate 1D and 2D spectra were calculated for ω_e/ω_g in the range $0.5-2.0$ at $T = 0.2\hbar\omega_g/k_B$ (low temperature) and $T = 5.0\hbar\omega_g/k_B$ (high temperature)

and for different values of the horizontal displacement $Q_d/\sqrt{\hbar/\omega_g} = 0.5, 1.0, 1.5$. The 2D spectra were also calculated at different values of t_2. The electronic dephasing rate constant used in all calculations was $\Gamma = \omega_g/2.8$ and the spectra are presented so that the frequency origin is set at $\langle\omega_{eg}\rangle$, which corresponds to the average of the stochastic $\omega_{eg}(t)$.

3.8.1 Linear Spectra

The 1D spectra at $T = 0.2\hbar\omega_g/k_B$ (low temperature) and $T = 5.0\hbar\omega_g/k_B$ (high temperature) are shown in Figs. 3.3 and 3.4, respectively, for $Q_d = \sqrt{\hbar/\omega_g}$ and the following four representative values of ω_e/ω_g: $0.6, 1.0, 1.4, 1.8$.

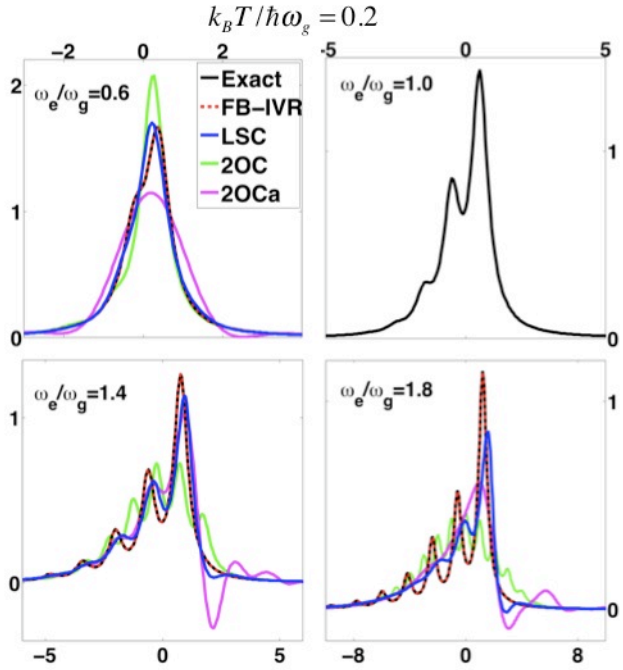

Figure 3.3: The 1D spectra at $T = 0.2\hbar\omega_g/k_B$ (low temperature) for $Q_d = \sqrt{\hbar/\omega_g}$ and the following values of ω_e/ω_g: $0.6, 1.0, 1.4, 1.8$, as obtained via an exact quantum mechanical calculation, as well as the FB-IVR, LSC, 2OC and 2OCa approximations.

As expected, the quantum-mechanically exact 1D spectra consist of peaks at the various vibronic transition frequencies. The widths of these peaks are determined by Γ and their intensities are determined by the thermal weight of the initial state

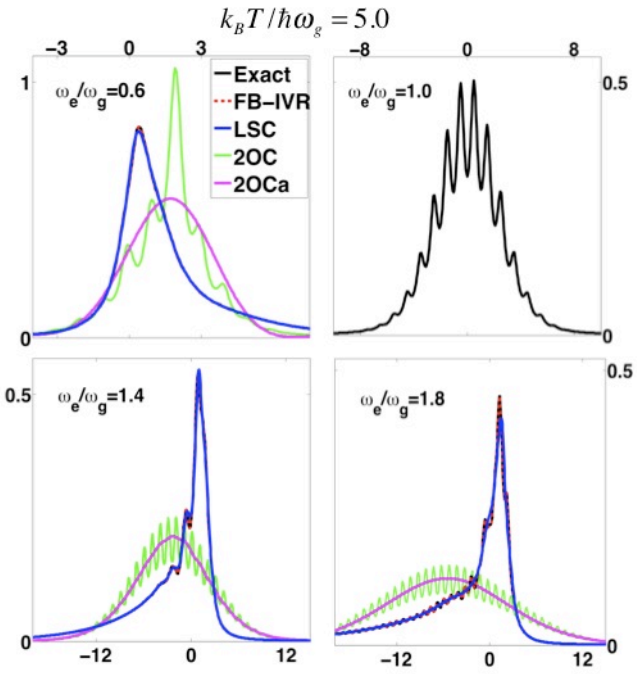

Figure 3.4: Same as Fig. 3.3 at $T = 5.0\hbar\omega_g/k_B$ (high temperature).

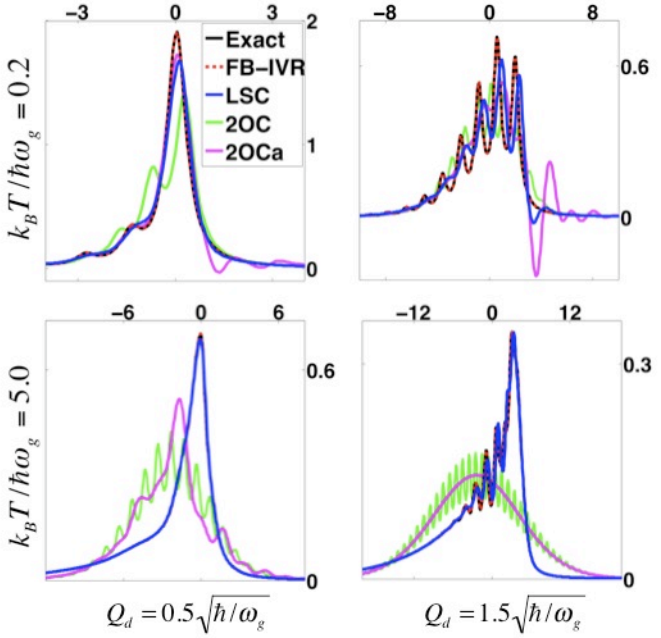

Figure 3.5: 1D spectra for $Q_d = (0.5, 1.5)\sqrt{\hbar/\omega_g}$, $\omega_e/\omega_g = 1.4$ and at $T = 0.2\hbar\omega_g/k_B$ and $T = 5.0\hbar\omega_g/k_B$,as obtained via an exact quantum mechanical calculation, as well as the FB-IVR, LSC, 2OC and 2OCa approximations.

and the corresponding products of Frank-Condon coefficients (see Eq. (3.21)). The following observations can be made based on these results:

- The 1D spectra obtained via FB-IVR were found to be in excellent agreement with the exact results throughout the entire region of parameter space considered. It should be noted that the fact that the coherent state width parameter γ was chosen to be constant (see Eq. (3.39)) implies that FB-IVR is not exact for the system considered here. More specifically, by assuming that γ is constant, FB-IVR neglects the fact that what is a coherent state on one surface corresponds to a squeezed state on the other surface. However, the corresponding changes of the width do not seem to affect the 1D spectra in a noticeable way even when ω_e and ω_g are significantly different.

- Although LSC is not as accurate as FB-IVR, it is clearly able to reproduce the main features of the 1D spectra rather well throughout a wide region of parameter space, and improves with increasing temperature. It should be noted that the agreement between the LSC and exact results depends on the choice of electronic dephasing rate constant, Γ. More specifically, the LSC approximation is known to be over-damped in comparison to the corresponding fully quantum-mechanical results, which can be attributed to the fact that it is based on purely classical all-forward dynamics and therefore lacks the ability to account for coherent quantum dynamical effects [93, 97, 131]. As a result, the LSC approach is particularly suitable for modeling spectra in cases where the physical dephasing is faster than any nonphysical dephasing caused by this over-damping. This is often the case in systems of practical interest and under ambient conditions. In order to mimic this situation, the present study used a value of Γ large enough so that the damping of the ORFs is dominated by it, rather than by the the

nonphysical dephasing inherent to the LSC approximation.

- Although the 1D spectra obtained via 2OC coincide with the exact ones when $\omega_e = \omega_g$, the agreement between them deteriorates rather rapidly once ω_e is allowed to deviate from ω_g. Importantly, the deviations are qualitative in nature in the sense that 2OC is unable to reproduce the overall asymmetry of the spectrum as well as the locations, relative intensities and widths of the peaks. These deviations reflect the two major approximations underlying 2OC, namely that the spectra reflect equilibrium ground state dynamics *and* that this equilibrium dynamics can be described by a Gaussian process.

- The 1D spectra obtained via 2OCa coincide with the exact spectra and the spectra obtained via 2OC when $\omega_e = \omega_g$. However, the 2OCa-based spectra are seen to deviate significantly from both when ω_e differs from ω_g. At low temperatures, 2OCa appears to be somewhat better at predicting the peak locations, which can be attributed to its ability to account for at least some of the spectral signature of nonequilibrium excited state dynamics on the spectra. Unfortunately, the low-temperature 2OCa-based spectra also becomes pronouncedly negative in some regions, which is clearly nonphysical. At high temperatures, the spectra obtained via 2OCa are seen to coincide with the envelopes of the spectra obtained via 2OC, but lack the fine structure of the latter, which can be attributed to over-damping generated by the nonequilibrium excited state dynamics. Finally, the fact that the accuracy of two distinctly different second-order cumulant approximations deteriorate so rapidly once we allow ω_e to differ from ω_g suggests that this type of approximation can only be expected to be reliable within a rather narrow region of parameter space.

In Fig. 3.5, we show the 1D spectra for two other values of Q_d, namely $Q_d =$

$(0.5, 1.5)\sqrt{\hbar/\omega_g}$, in the case $\omega_e/\omega_g = 1.4$ and at $T = 0.2\hbar\omega_g/k_B$ and $T = 5.0\hbar\omega_g/k_B$. It should be noted that the 1D spectra obtained via all four approximate methods coincide with the exact ones when $\omega_e = \omega_g$, regardless of the value of Q_d. However, this is not the case when $\omega_e/\omega_g \neq 1$. The 1D spectra obtained via FB-IVR are seen to be in excellent agreement with the exact ones regardless of the value of Q_d. As expected, LSC also remains accurate at high temperature regardless of the value of Q_d. Interestingly, LSC is also observed to remain rather accurate even at the lower temperature, although the level of accuracy is observed to diminish with increasing Q_d. Finally, the 1D spectra predicted by 2OC and 2OCa are seen to be significantly different from the exact ones regardless of the values of Q_d, and the deviations are seen to *increase* with temperature.

3.8.2 Nonlinear Spectra

The exact 2D spectra at $T = 0.2\hbar\omega_g/k_B$ (low temperature) and $T = 5.0\hbar\omega_g/k_B$ (high temperature)are shown in Fig. 3.6 as a function of t_2, for $Q_d = \sqrt{\hbar/\omega_g}$ and in the special case where the frequencies of the ground and excited surfaces coincide, namely $\omega_e = \omega_g$.

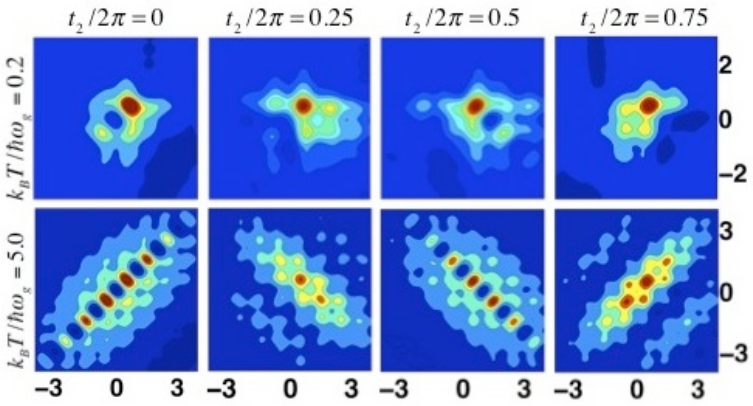

Figure 3.6: The exact 2D spectra at $T = 0.2\hbar\omega_g/k_B$ (low temperature) and $T = 5.0\hbar\omega_g/k_B$ (high temperature) as a function of t_2, for $Q_d = \sqrt{\hbar/\omega_g}$ and $\omega_e/\omega_g = 1$.

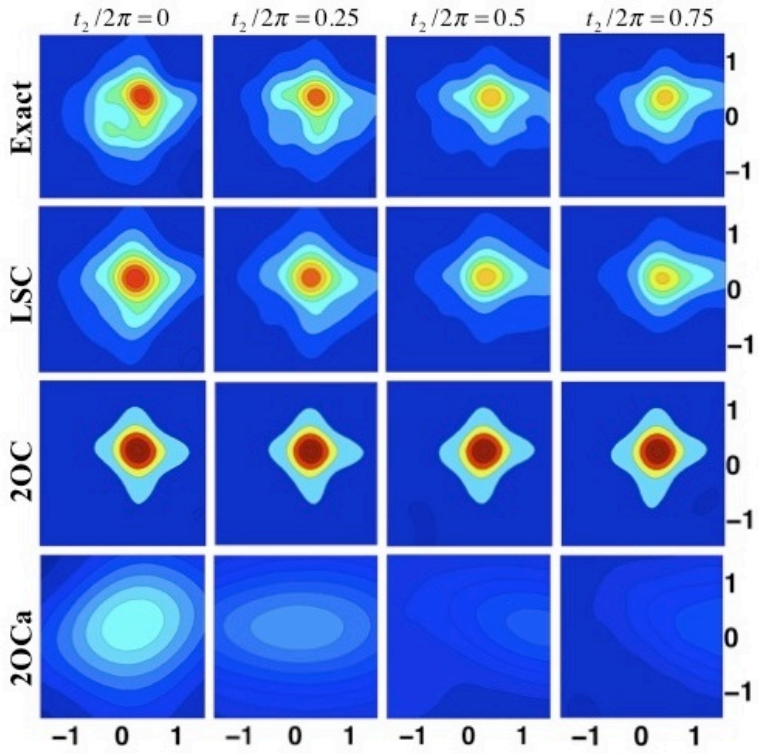

Figure 3.7: A comparison of the exact 2D spectra to the corresponding LSC, 2OC and 2OCa approximations in the case where $\omega_e/\omega_g = 0.6$ at $T = 0.2\hbar\omega_g/k_B$ (low temperature).

As expected, the 2D spectra consist of peaks at the various vibronic frequencies. The widths of these peaks are determined by Γ and their intensities are determined by the thermal weight of the initial state and the products of F-C factors (see Eq. (3.26)). The peak pattern is also seen to change as a function of t_2 as dictated by Eqs. (3.26), and the number of peaks is seen to increase with temperature, which reflects the larger number of initially populated ground vibronic states. However, the fact that the vibronic wave functions become increasingly more localized at the turning points with increasing energy implies that the corresponding F-C factors drop rapidly. As a result, the intensity of peaks that correspond to transitions between excited states tends to rapidly decrease the more excited the vibronic states are. As for the 1D spectra, the 2D spectra generated via FB-IVR, LSC, 2OC and 2OCa all coincide with the exact results when $\omega_e = \omega_g$ (see Fig. 3.6).

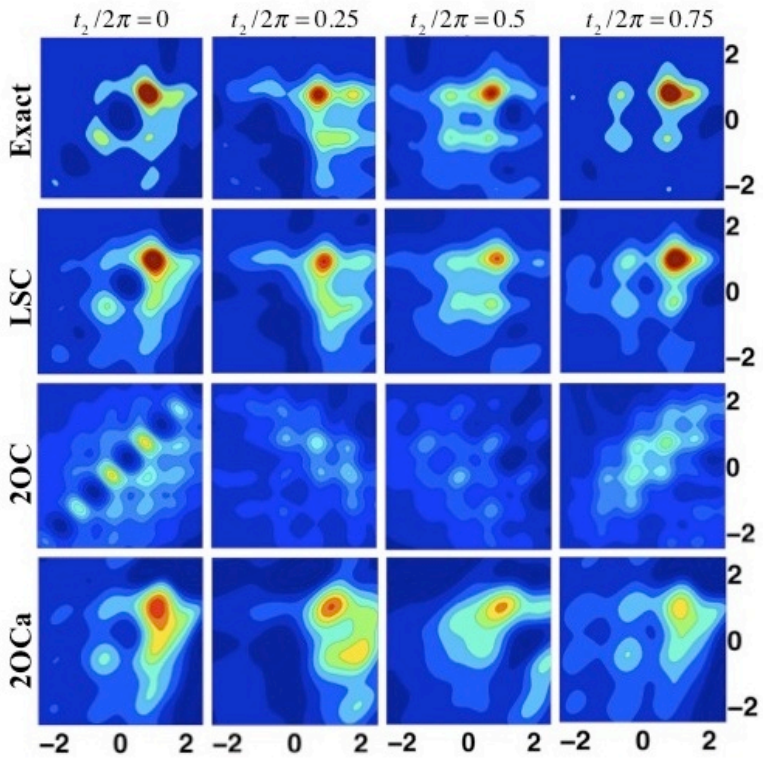

Figure 3.8: A comparison of the exact 2D spectra to the corresponding LSC, 2OC and 2OCa approximations in the case where $\omega_e/\omega_g = 1.4$ at $T = 0.2\hbar\omega_g/k_B$ (low temperature).

In Figs. 3.7-3.12, we present a comparison of the exact 2D spectra to the corresponding LSC, 2OC and 2OCa approximations in the case where $\omega_e \neq \omega_g$. More specifically, we compare 2D spectra at $T = 0.2\hbar\omega_g/k_B$ (Figs. 3.7-3.9) and $T = 5.0\hbar\omega_g/k_B$ (Figs. 3.10-3.12) for $Q_d = \sqrt{\hbar/\omega_g}$ and at various values of t_2. We have also repeated the calculation for other values of Q_d (not shown). However, we have not found new trends with respect to the Q_d dependence besides those noted in the context of the 1D spectra (see Fig. 3.5). The 2D spectra generated via FB-IVR were observed to be practically indistinguishable from the exact ones and are therefore not shown. This implies that although strictly speaking the FB-IVR approximation is not exact when $\omega_e \neq \omega_g$, the 2D spectra are essentially insensitive to the difference, at least for the model under consideration here.

Unlike the spectra generated via FB-IVR, there are visible deviations between

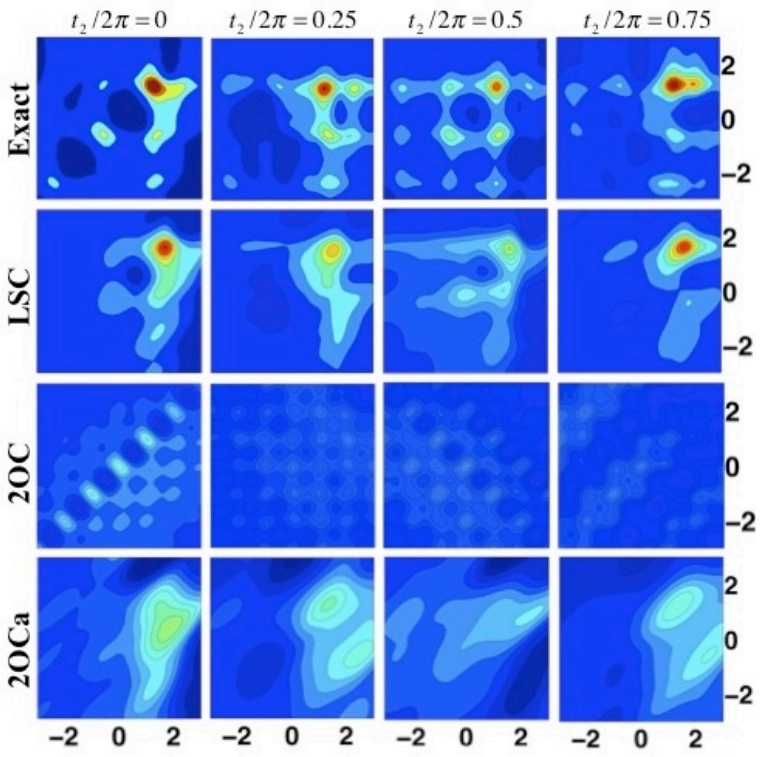

Figure 3.9: A comparison of the exact 2D spectra to the corresponding LSC, 2OC and 2OCa approximations in the case where $\omega_e/\omega_g = 1.8$ at $T = 0.2\hbar\omega_g/k_B$ (low temperature).

the exact spectra and those obtained via LSC. However, those deviations remain small throughout the region of parameter space considered, thereby testifying to the robustness of the LSC approximation. In fact, while the accuracy of the LSC approximation at the high temperature is expected in light of the classical treatment of the photo-inactive coordinate, the fact that it is also accurate at the low temperature is somewhat surprising. The latter observation can probably be attributed to the fact that all the potential energy surfaces involved are harmonic, as the presence of anharmonicities would have given rise to more pronounced quantum effects at low temperatures. It should also be noted that the accuracy of LSC is better at $\omega_e/\omega_g < 1$, compared to $\omega_e/\omega_g > 1$, since the lower frequency of the excited state surface makes it more classical.

Finally, the 2D spectra generated via 2OC and 2OCa are seen to be highly inaccu-

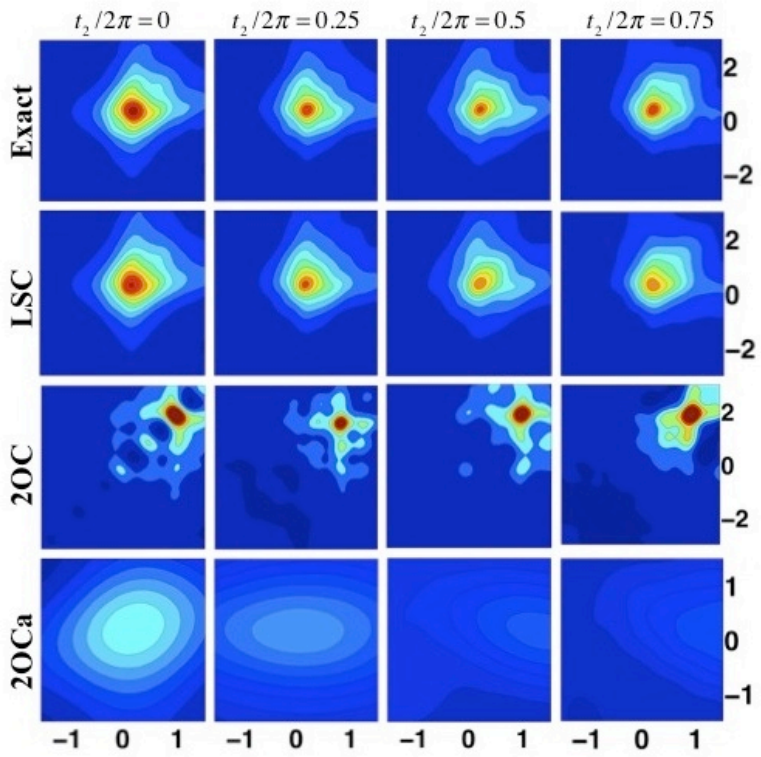

Figure 3.10: A comparison of the exact 2D spectra to the corresponding LSC, 2OC and 2OCa approximations in the case where $\omega_e/\omega_g = 0.6$ at $T = 5.0\hbar\omega_g/k_B$ (high temperature).

rate in almost every respect. More specifically, although the 2D spectra generated by both the 2OC and 2OCa approximations coincide with the exact ones when $\omega_e = \omega_g$, the agreement between the approximate and exact spectra deteriorates rather rapidly once ω_e is allowed to differ from ω_g. At the high temperature, the predictions of 2OC and 2OCa are seen to differ qualitatively from the exact results regardless of the value of ω_e/ω_g. However, at the lower temperature, 2OC actually seems to perform reasonably well for $\omega_e/\omega_g = 0.6$, while 2OCa fails. Nevertheless, the trend reverses for $\omega_e/\omega_g = 1.4$, where it is actually 2OCa which is seen to be in reasonable agreement with the exact results, while 2OC fails. This suggests the growing importance of accounting for excited state dynamics when $\omega_e > \omega_g$, at least at low temperatures. However, generally speaking, the second-order cumulant approximation, in either its 2OC or 2OCa renditions, is seen to be rather inaccurate and to lack robustness even

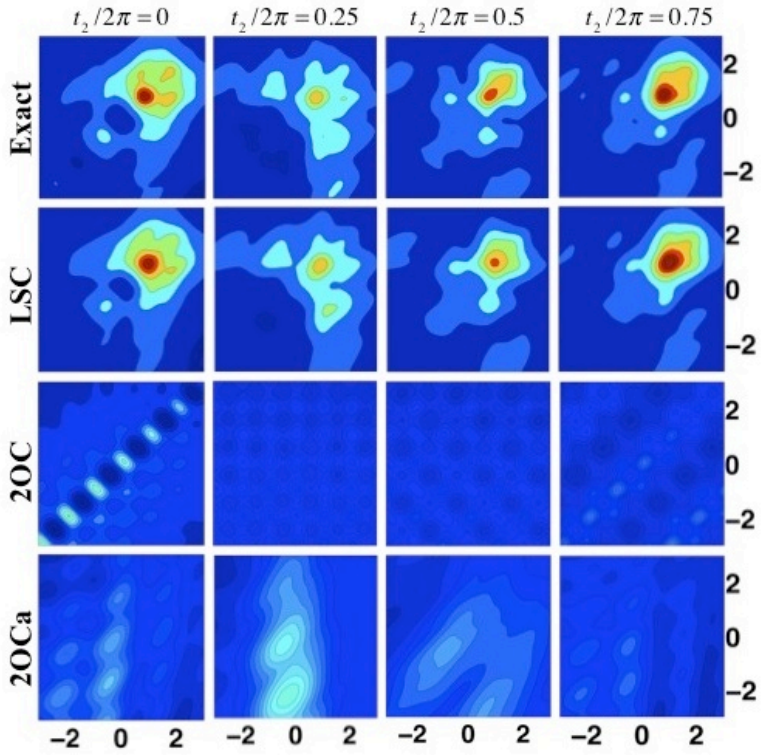

Figure 3.11: A comparison of the exact 2D spectra to the corresponding LSC, 2OC and 2OCa approximations in the case where $\omega_e/\omega_g = 1.4$ at $T = 5.0\hbar\omega_g/k_B$ (high temperature).

in the case where the potential surfaces are harmonic, provided that they do not have the same frequency.

3.9 Summary and Future Outlook

In this chapter, the accuracies of the FB-IVR, LSC, 2OC and 2OCa methods for calculating 1D and 2D spectra within the context of a benchmark model of a two-state chromophore with shifted harmonic potential surfaces were considered. It has been shown that all methods reproduce spectra that coincide with the exact ones when the frequencies of the two surfaces are the same, regardless of the temperature or relative displacement of those surfaces. As a result, a meaningful benchmark must be based on having the two surfaces correspond to different frequencies, and the accuracy consequently becomes dependent on the frequency ratio.

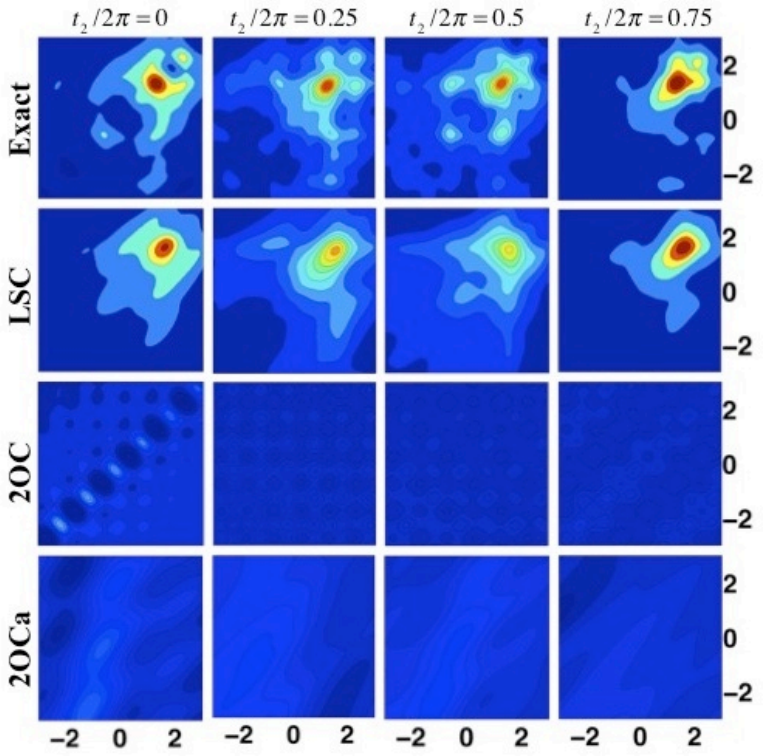

Figure 3.12: A comparison of the exact 2D spectra to the corresponding LSC, 2OC and 2OCa approximations in the case where $\omega_e/\omega_g = 1.8$ at $T = 5.0\hbar\omega_g/k_B$ (high temperature).

The spectra generated via FB-IVR were found to be in excellent agreement with the exact ones throughout the entire region of parameter space considered. Good agreement was also observed between the spectra calculated via LSC and the exact ones, provided that the exact ORFs decay on a time scale shorter than that of the nonphysical over-damping inherent to the LSC approximation. Finally, the second-order cumulant approximation, either in its standard form, 2OC, or alternative form, 2OCa, were generally found to be inaccurate and unreliable unless $\omega_e \approx \omega_g$.

Although the FB-IVR method is superior to LSC in regard to accuracy, its computational cost is also significantly higher. Thus, our results seem to point to LSC as the method of choice for modeling 2D spectra in complex systems for which an exact quantum-mechanical, or even the approximate but rather expensive FB-IVR method, may not be feasible.

CHAPTER IV

Two-dimensional Infrared Spectra for Multistate Systems

4.1 Introduction

A major challenge in establishing a general computational scheme for vibrational systems is that in order to derive information from the measured spectra, the vibrational Hamiltonian needs to be newly identified for each system, making transferability of parameters between systems impractical if not impossible [28]. As a result, many studies relied on the use of empirical fitting algorithms to extract information from measured spectra, which often emplyed models with terms whose relative importance was not well understood [31]. An alternative approach based on inputs from *ab initio* electronic structure calculations is advantageous in that is allows for the simulation and prediction of nonlinear vibrational spectra *without* having to rely on experimental input parameters [140, 141].

An attractive candidate for testing ab initio methods was dicarbonylacetylacetonato rhodium(I) (RDC), since the stretching vibrations of its two C≡O local oscillators are sufficiently separated from other abosorption bands that their nonlinear response can be measured without contributions from other modes. Measurement and analysis of the 2D spectra of this compound have led to important insight into how anharmonicity, mode−mode coupling, the tensorial nature of optical response,

and rotational relaxation affect 2DIR spectra [142–145]. *Ab initio* methods have been successful in capturing such effects [28, 146–151]. More specifically, Moran and coworkers [28] have recently produced a 2DIR spectrum of RDC by computing the 2D anharmonic potential energy surface in terms of the carbonyl stretch coordinates up to fourth-order via Density Functional Theory (DFT) and numerically diagonalizing the corresponding Hamiltonian. The aim of the work presented in this chapter was to apply such ab initio methods to study the metal carbonyl compound $Mn_2(CO)_{10}$ and its photoproducts $Mn_2(CO)_9$ and $Mn(CO)_5$. Most of the effort was spent establishing the necessary computational framework, both in terms of applying the optical response tensor (ORT) formalism and coupling it to detailed electronic structure calculations.

It should be emphasized that the results presented here were obtained as part of an ongoing collaboration between the research groups of Prof. Eitan Geva and Prof. Kevin Kubarych, both at the University of Michigan. More specifically, my role was strictly in the development and implementation of the computer codes used to manipulate the electronic structure data and compute the ORTs. Mr. Nicholas Preketes, a former undergraduate in the Geva group, and Mr. Carlos Baiz, a current graduate student in the Kubarych group, were responsible for the electronic structure calculations. Two major points regarding the initial stages of this project should be noted:

- A main focus of investigation was which normal modes to include in the calculations. i.e., only the photo active CO stretches, both the photoactive and photoinactive CO stretches, or all normal modes of the system (not only CO stretches). The initial results generated for $Mn(CO)_5$ included *only the photoactive carbonyl modes*, which resulted in *negative* diagonal anharmonic peak

shifts, a trend that was contrary to other experimental and theoretical studies. While this issue was not resolved during the timeline of my involvement with the project, later studies performed by Mr. Baiz found that the qualitatively incorrect anharmonic shifts could be traced back to neglecting the coupling between the photoactive and photoinactive CO stretching modes. The trend may be clearly seen for $Mn_2(CO)_{10}$ results in Table 4.1 (reproduced from Ref. [142]). The shifts obtained by considering only the IR active modes are highlighted in red.

- Initally, a *direct diagonalization* procedure was implemented in Matlab to diagonalize the anharmonic Hamiltonian. Since convergence of the energy levels requires a basis which is much larger than the subspace spanned by the number of modes of interest (see the end of §4.3.1), there is an inherent limitation on how many modes may be included since the matrices may become too large to be diagonalized efficiently. Thus a computational bottleneck was reached when transitioning from the study of $Mn(CO)_5$ to $Mn_2(CO)_9$, and it was around this time that my involvement in the project was finished[1]. Later work by Mr. Baiz utilized an alternative perturbation theory approach to circumvent the problem [142].

The remainder of this chapter is organized as follows. In §4.2, the general theory of ORTs is presented, where the overall response is separated into a product of vibrational and rotational contributions. In §4.3, the full ab inito procedure is outlined. First, a description of how to construct the anharmonic Hamiltonian as a Taylor series in the normal mode coordinates is presented, following by a discussion of how to compute the transition dipole moment vectors. Then, an overview of the electronic

[1]Some preliminary work was performed with implementing sparse matrix algorithms, but was never carried to completion.

structure calculations used to obtain the second, third, and fourth-order force constants is presented. In §4.4, the preliminary results obtained for the photoproduct $Mn(CO)_5$ are presented, following by discussion of future and ongoing work.

Table 4.1: **Diagonal Anharmonic Shifts. $\Delta = \omega_{0\to1} - \omega_{1\to2}$ for $Mn_2(CO)_{10}$ in cm^{-1}, as obtained using VPT2. Adapted from Ref. [142]**

mode	all modes 3rd and 4th order	all modes 3rd order only	CO modes 3rd and 4th order	IR active CO modes 3rd and 4th order	expl
1	5.2	10.2	4.3		
2	5.3	10.2	4.3		
3	6.5	12.8	5.4	-6.3	8.3
4	9.7	19.1	8.0		
5	5.5	10.3	4.5	-4.7	6.5
6	5.5	10.3	4.5	-4.7	6.5
7	3.9	7.4	3.0		
8	4.6	7.6	3.7		
9	3.2	5.3	2.5	-2.1	4.4
10	3.4	5.0	2.6		

4.2 Polarization-Selective Response: Optical Response Tensors

As introduced in ch. 2, the linear and third-order optical response functions can generally be written terms of two-point and four-point time correlation functions of the transition dipole operator. For example[2],

$$\begin{aligned} J(t_1) &= \mathrm{Tr}\left[\hat{\mu}(t_1)\,\hat{\mu}\hat{\rho}_{eq}\right] \\ R_1(t_3,t_2,t_1) &= \mathrm{Tr}\left[\hat{\mu}(t_1)\,\hat{\mu}(t_2+t_1)\,\hat{\mu}(t_3+t_2+t_1)\,\hat{\mu}(0)\,\hat{\rho}_{eq}\right] \end{aligned} \tag{4.1}$$

If only a single transition were involved and the dipole operators were scalars as in Chapter 2, the response would be characterized by *functions*. However, to describe processes involving several distinct transition dipoles, their vector nature requires consideration and leads to a response characterized by *tensors* [143, 152]. What was previously the n-order ORF becomes an $(n+1)$-rank tensor $S^{(n)}_{b_{n+1},\ldots,b_1}(t_n,\ldots,t_1)$,

[2]The remaining third-order response functions $R_2 - R_4$ have a similar structure, but differ by permutations of the time arguments.

which gives the b_{n+1}-th component of the polarization at time t in response to various combinations of the field Cartesian components, $b_n, ..., b_1$, at previous times.

For example, in the case of linear response, the optical response tensor (ORT) is of rank 2 and has nine components:

$$J_{x'x'}(t_1), J_{y'y'}(t_1), J_{z'z'}(t_1), J_{x'y'}(t_1), J_{y'z'}(t_1), J_{x'z'}(t_1), J_{y'x'}(t_1), J_{z'y'}(t_1), J_{z'x'}(t_1) \quad (4.2)$$

which correspond to the x', y' and z' components of the polarization in (linear) response to the x', y' or z' components of the driving field. Hence

$$J_{b_2,b_1}(t_1) = \mathrm{Tr}\left[\hat{\mu}_{b_2}(t_1)\,\hat{\mu}_{b_1}\hat{\rho}_{eq}\right]. \quad (4.3)$$

Similiary, the third-order ORT is of rank 4 and given by: (4.3)

$$\begin{aligned}
R_{b_4,b_3,b_2,b_1;1}(t_3,t_2,t_1) &= \mathrm{Tr}\left[\hat{\mu}_{b_2}(t_1)\,\hat{\mu}_{b_3}(t_2+t_1)\,\hat{\mu}_{b_4}(t_3+t_2+t_1)\,\hat{\mu}_{b_1}(0)\,\hat{\rho}_{eq}\right] \\
R_{b_4,b_3,b_2,b_1;2}(t_3,t_2,t_1) &= \mathrm{Tr}\left[\hat{\mu}_{b_1}(0)\,\hat{\mu}_{b_3}(t_2+t_1)\,\hat{\mu}_{b_4}(t_3+t_2+t_1)\,\hat{\mu}_{b_2}(t_1)\,\hat{\rho}_{eq}\right] \\
R_{b_4,b_3,b_2,b_1;3}(t_3,t_2,t_1) &= \mathrm{Tr}\left[\hat{\mu}_{b_1}(0)\,\hat{\mu}_{b_2}(t_1)\,\hat{\mu}_{b_4}(t_3+t_2+t_1)\,\hat{\mu}_{b_3}(t_2+t_1)\,\hat{\rho}_{eq}\right] \\
R_{b_4,b_3,b_2,b_1;4}(t_3,t_2,t_1) &= \mathrm{Tr}\left[\hat{\mu}_{b_4}(t_3+t_2+t_1)\,\hat{\mu}_{b_3}(t_2+t_1)\,\hat{\mu}_{b_2}(t_1)\,\hat{\mu}_{b_1}(0)\,\hat{\rho}_{eq}\right]
\end{aligned} \quad (4.5)$$

4.2.1 Orientational Averaging

In the above discussion, $b_1, ..., b_n = x', y', z'$ correspond to some specific choice of a coordinate system. The laboratory frame is the natural choice for the driving field and the detected signal. However, the dipole vector $\overrightarrow{\mu}$ is most easily computed in terms of a *body-fixed coordinate system*. Furthermore, unlike the laboratory system which is stationary, the body-fixed coordinate system rotates with the molecule and therefore changes over time. Denoting the body-fixed and lab frames by indices b and a, respectively, the two coordinate systems are related by a time-dependent

orthogonal transformation T [153] (see Appendix D):

$$\mu_a(t) = \sum_{b(t)} T_{a,b(t)} \mu_{b(t)}(t) \Leftrightarrow \mu_{b(t)}(t) = \sum_a T_{b(t),a} \mu_a(t) \tag{4.6}$$

where $b(t) = \{x'(t), y'(t), z'(t)\}$ correspond to the explicitly time-dependent body fixed coordinates.

The averaging procedure may be straightforwardly illustrated by applying the transformations in (4.6) to the linear response tensor in (4.3):

$$\begin{aligned} J_{a_2,a_1}(t_1) &= \mathrm{Tr}\left[\mu_{b_2}(t_1)\,\mu_{b_1}\hat{\rho}_{eq}\right] \\ &= \mathrm{Tr}\left[\sum_{b_2(t_1)} T_{a_2,b_2(t_1)}\mu_{b_2(t_1)}(t_1) \sum_{b(0)} T_{a_1,b_1(0)}\mu_{b_1}(0)\,\hat{\rho}_{eq}\right] \\ &= \sum_{b_2(t_1)}\sum_{b(0)} \langle T_{a_2,b_2(t_1)}\mu_{b_2(t_1)}(t_1)\, T_{a_1,b_1(0)}\mu_{b_1}(0)\rangle_{eq} \end{aligned} \tag{4.7}$$

The interpretation of the ORTs can be greatly simplified by separating different degrees of freedom according to relative timescales. More specifically, if the rotational motion is much slower than the vibronic dynamics then the ORT may be separated into a product of a vibrational and orientational contributions [152]. Assuming that the rotational motion may be treated *classically*[3], the decoupling of vibrational and orientational motions results in

$$J_{a_2,a_1}(t_1) = \sum_{b_2(t_1)}\sum_{b(0)} \langle T_{a_2,b_2(t_1)} T_{a_1,b_1(0)}\rangle_{eq}^{Cl} \times \langle \mu_{b_2(t_1)}(t_1)\,\mu_{b_1}(0)\rangle_{eq} \tag{4.8}$$

Thus the linear response in the lab frame and body-fixed frames are related by

$$J_{a_2,a_1}(t_1) = \sum_{b_2,b_1} Y_{b_2,b_1}^{a_2,a_1}(t_1)\, J_{b_2,b_1}(t_1) \tag{4.9}$$

where

$$Y_{b_2,b_1}^{a_2,a_1}(t_1) \equiv \langle T_{a_2,b_2(t_1)} T_{a_1,b_1(0)}\rangle_{eq}^{Cl} \tag{4.10}$$

[3]The averaging procedure described here is not contingent upon this assumption. e.g., Ref. [152] treats the orientational relaxation diffusively.

A similar analysis for the third-order response, where $j = 1, 2, 3, 4$, results in

$$R_{a_4,a_3,a_2,a_1;j}(t_3,t_2,t_1) = \sum_{b_4,b_3,b_2,b_1} Y^{a_4,a_3,a_2,a_1}_{b_4,b_3,b_2,b_1}(t_3,t_2,t_1)\, R_{b_4,b_3,b_2,b_1;j}(t_3,t_2,t_1) \quad (4.11)$$

where

$$Y^{a_4,a_3,a_2,a_1}_{b_4,b_3,b_2,b_1}(t_2,t_1) \equiv \left\langle T_{a_4,b_4(t_1+t_2+t_3)} T_{a_3,b_3(t_1+t_2)} T_{a_2,b_2(t_1)} T_{a_1,b_1(0)} \right\rangle^{Cl}_{eq}. \quad (4.12)$$

Eqns.(4.9) and (4.11) provide a convenient route to calculate the laboratory frame polarization in response to a laboratory frame driving field, starting out with an ORT which is given in terms the body-fixed coordinates. This will be particularly useful when *ab initio* electronic structure inputs are used to describe the vibrational motion, as described later in the chapter. However, the calculations require knowledge of the $(n+1)$-th rank orientational tensor $Y^{a_{n+1},\ldots,a_1}_{b_{n+1},\ldots,b_1}(t_n,\ldots,t_1)$, which in turn requires input regarding the rotational motion of the molecule. Although $J_{b_2,b_1}(t_1)$ and $R_{b_4,b_3,b_2,b_1;j}(t_3,t_2,t_1)$ are sensitive to the vibrational dynamics relative to the body-fixed coordinate system, the decoupling of the rotational and vibrational motions implies that the body-frame ORTs may be computed once and used regardless of the instantaneous molecular orientation. In other words, all the information on the rotational motion of the molecule is contained in the tensor $Y^{a_{n+1},\ldots,a_1}_{b_{n+1},\ldots,b_1}(t_n,\ldots,t_1)$ [31, 152].

4.2.2 Optical Response Tensors for a Multistate Vibrational System

To derive explicit expressions for the body-frame tensors $J_{b_2,b_1}(t_1)$ and $R_{b_4,b_3,b_2,b_1;j}(t_3,t_2,t_1)$ given in (4.3) and (4.5), we begin with the dipole moment defined in (1.12), except now there are limits on the summations. This is due to the assumption that the magnitude of the transition dipoles are appreciable only for a set of n_1 states in the first band and n_2 states in the second band:

$$\overrightarrow{\mu} = \sum_{j=0}^{n_1} [\overrightarrow{\mu}_{00,1j} |00\rangle \langle 1j| + \overrightarrow{\mu}_{1j,00} |1j\rangle \langle 00|] + \sum_{j=0}^{n_1} \sum_{k=0}^{n_2} [\overrightarrow{\mu}_{1j,2k} |1j\rangle \langle 2k| + \overrightarrow{\mu}_{2k,1j} |2k\rangle \langle 1j|] \tag{4.13}$$

In addition, we assume that $\beta\hbar\omega_{10} \gg 1$, so that the equilibrium density operator corresponds to the ground state

$$\hat{\rho}_{eq} = |00\rangle \langle 00| \tag{4.14}$$

As an illustrative example, the linear response will be considered in detail. We start by noting that all of the states described above, regardless of the band they belong to, are orthonormal eigenstates of the molecular Hamiltonian, $\hat{H}_M$, such that

$$\begin{aligned} \langle 00|00\rangle = 1; \langle 1j_1|1j_2\rangle &= \delta_{j_1,j_2}; \langle 2k_1|2k_2\rangle = \delta_{k_1,k_2} \\ \langle 00|1j\rangle = \langle 00|2k\rangle &= \langle 1j|2k\rangle = 0 \\ e^{\pm i\hat{H}t/\hbar} |1j\rangle = e^{\pm i\varepsilon_{1j}t/\hbar} |1j\rangle \quad &; \quad e^{\pm i\hat{H}t/\hbar} |2k\rangle = e^{\pm i\varepsilon_{2k}t/\hbar} |2k\rangle \end{aligned} \tag{4.15}$$

With the above considerations, along with the fact that (see (4.13)),

$$\mu_{b_1} \hat{\rho}_{eq} = \sum_{j_1=0}^{n_1} \mu_{1j_1,00,b_1} |1j_1\rangle \langle 00|, \tag{4.16}$$

the linear response in the body-fixed frame becomes

$$
\begin{aligned}
J_{b_2,b_1}(t_1) &= Tr\left[\mu_{b_2}(t_1)\,\mu_{b_1}\hat{\rho}_{eq}\right] = Tr\left[e^{iHt_1/\hbar}\mu_{b_2}e^{-iHt_1/\hbar}\mu_{b_1}\hat{\rho}_{eq}\right] \qquad (4.17)\\
&= Tr\left\{ e^{iHt_1/\hbar}\left[\begin{array}{l}\sum_{j_2=0}^{n_1}\left[\mu_{00,1j_2,a_2}\left|00\right\rangle\left\langle 1j_2\right| + \mu_{1j_2,00,a_2}\left|1j_2\right\rangle\left\langle 00\right|\right]\\ +\sum_{j_2=0}^{n_1}\sum_{k_2=0}^{n_2}\left[\mu_{1j_2k_2,a_2}\left|1j_2\right\rangle\left\langle 2k_2\right| + \mu_{2k_21j_2,a_2}\left|2k_2\right\rangle\left\langle 1j_2\right|\right]\end{array}\right] e^{-iHt_1/\hbar} \right.\\
&\qquad \left. \times\sum_{j_1=0}^{n_1}\mu_{1j_1,00,b_1}\left|1j_1\right\rangle\left\langle 00\right| \right\}\\
&= Tr\left\{ \begin{array}{l}\sum_{j_1,j_2=0}^{n_1}\mu_{00,1j_2,b_2}\mu_{1j_1,00,b_1}\left|00\right\rangle\left\langle 1j_2\right|\,1j_1\rangle\left\langle 00\right| e^{-i\varepsilon_{1j}t_1/\hbar}\\ +\sum_{j_1,j_2=0}^{n_1}\sum_{k_2=0}^{n_2}\mu_{2k_21j_2,b_2}\mu_{1j_1,00,b_1}e^{i\varepsilon_{2k}t_1/\hbar}\left|2k_2\right\rangle\left\langle 1j_2\right|\,1j_1\rangle\left\langle 00\right|\end{array} \right\}\\
&= \sum_{j_1=0}^{n_1}\mu_{00,1j_2,b_2}\mu_{1j_1,00,b_1}e^{-i\varepsilon_{1j}t_1/\hbar}
\end{aligned}
$$

Thus according to (4.9), the linear response in the lab frame is

$$
J_{a_2,a_1}(t_1) = \sum_{b_2,b_1} Y_{b_2,b_1}^{a_2,a_1}(t_1)\sum_{j_1=0}^{n_1}\mu_{00,1j_2,b_2}\mu_{1j_1,00,b_1}e^{-i\varepsilon_{1j}t_1/\hbar} \qquad (4.18)
$$

A similar procedure leads to the third-order ORTs in the body-fixed frame

$$
\begin{aligned}
&R_{b_4,b_3,b_2,b_1;1}(t_3,t_2,t_1)\\
&= \sum_{j_1,j_2=0}^{n_1}\mu_{00,1j_2,b_2}\mu_{1j_2,00,b_3}\mu_{00,1j_1,b_4}\mu_{1j_1,00,b_1}e^{i\left(\varepsilon_{1j_2}-\varepsilon_{1j_1}\right)t_2/\hbar}e^{-i\varepsilon_{1j_1}(t_1+t_3)/\hbar} \qquad (4.19)\\
&+ \sum_{j_1,j_2=0}^{n_1}\sum_{k=0}^{n_2}\mu_{00,1j_2,b_2}\mu_{1j_1,00,b_1}\mu_{1j_22k,b_3}\mu_{2k,1j_1,b_4}e^{-i\varepsilon_{1j_1}t_1/\hbar}e^{i\left(\varepsilon_{1j_2}-\varepsilon_{1j_1}\right)t_2/\hbar}e^{i\left(\varepsilon_{2k}-\varepsilon_{1j_1}\right)t_3/\hbar}\\
&\equiv R^{(1)}_{b_4,b_3,b_2,b_1;1}(t_3,t_2,t_1) + R^{(2)}_{b_4,b_3,b_2,b_1;1}(t_3,t_2,t_1)
\end{aligned}
$$

$$
\begin{aligned}
&R_{b_4,b_3,b_2,b_1;2}\left(t_3,t_2,t_1\right)\\
&=\sum_{j_1,j_2=0}^{n_1}\mu_{00,1j_1,b_1}\mu_{1j_2,00,b_2}\mu_{1j_1,00,b_3}\mu_{00,1j_2,b_4}e^{i\varepsilon_{1j_1}t_1/\hbar+i\left(\varepsilon_{1j_1}-\varepsilon_{1j_2}\right)t_2/\hbar}e^{-i\varepsilon_{1j_2}t_3/\hbar}\\
&+\sum_{j_1,j_2=0}^{n_1}\sum_{k=0}^{n_2}\mu_{00,1j_1,b_1}\mu_{1j_2,00,b_2}\mu_{1j_1,2k,b_3}\mu_{2k,1j_2,b_4}e^{i\varepsilon_{1j_1}(t_2+t_1)/\hbar}e^{i\varepsilon_{2k_3}t_3/\hbar}e^{-i\varepsilon_{1j_2}(t_3+t_2)/\hbar}\\
&\equiv R^{(1)}_{b_4,b_3,b_2,b_1;2}\left(t_3,t_2,t_1\right)+R^{(2)}_{b_4,b_3,b_2,b_1;2}\left(t_3,t_2,t_1\right)
\end{aligned}
\tag{4.20}
$$

$$
\begin{aligned}
&R_{b_4,b_3,b_2,b_1;3}\left(t_3,t_2,t_1\right)\\
&=\sum_{j_1,j_2=0}^{n_1}\mu_{00,1j_1,b_1}\mu_{1j_1,00,b_2}\mu_{1j_2,00,b_3}\mu_{00,1j_2,b_4}e^{i\varepsilon_{1j_1}t_1/\hbar-i\varepsilon_{1j_2}t_3/\hbar}\\
&+\sum_{j_1,j_2=0}^{n_1}\sum_{k=0}^{n_2}\mu_{00,1j_1,b_1}\mu_{1j_1,2k,b_2}\mu_{1j_2,00,b_3}\mu_{2k,1j_2,a_4}e^{i\varepsilon_{1j_1}t_1/\hbar+i\varepsilon_{2k}t_2/\hbar+i\left(\varepsilon_{2k}-\varepsilon_{1j_2}\right)t_3/\hbar}\\
&\equiv R^{(1)}_{b_4,b_3,b_2,b_1;3}\left(t_3,t_2,t_1\right)+R^{(2)}_{b_4,b_3,b_2,b_1;3}\left(t_3,t_2,t_1\right)
\end{aligned}
\tag{4.21}
$$

$$
\begin{aligned}
&R_{b_4,b_3,b_2,b_1;4}\left(t_3,t_2,t_1\right)\\
&=\sum_{j_1,j_2=0}^{n_1}\mu_{1j_1,00,b_1}\mu_{00,1j_1,b_2}\mu_{1j_2,00,b_3}\mu_{00,1j_2,b_4}e^{-i\varepsilon_{1j_2}t_3/\hbar-i\varepsilon_{1j_1}t_1/\hbar}\\
&+\sum_{j_1,j_2=0}^{n_1}\sum_{k=0}^{n_2}\mu_{1j_1,00,b_1}\mu_{2k,1j_1,b_2}\mu_{1j_2,2k,b_3}\mu_{00,1j_2,b_4}e^{-i\varepsilon_{1j_2}t_3/\hbar-i\varepsilon_{2k}t_2/\hbar-i\varepsilon_{1j_1}t_1/\hbar}\\
&\equiv R^{(1)}_{b_4,b_3,b_2,b_1;4}\left(t_3,t_2,t_1\right)+R^{(2)}_{b_4,b_3,b_2,b_1;4}\left(t_3,t_2,t_1\right)
\end{aligned}
\tag{4.22}
$$

The ORTs in the lab frame are then given by (4.11) for $j=1,2,3,4$

$$
R_{a_4,a_3,a_2,a_1;j}\left(t_3,t_2,t_1\right)=\sum_{b_4,b_3,b_2,b_1}Y^{a_4,a_3,a_2,a_1}_{b_4,b_3,b_2,b_1}\left(t_3,t_2,t_1\right)\left[R^{(1)}_{b_4,b_3,b_2,b_1;j}\left(t_3,t_2,t_1\right)+R^{(2)}_{b_4,b_3,b_2,b_1;j}\left(t_3,t_2,t_1\right)\right],
\tag{4.23}
$$

and the rephasing and nonrephasing signals by

$$
\begin{aligned}
R_{a_4,a_3,a_2,a_1;nr} &= R^{(1)}_{a_4,a_3,a_2,a_1;1}+R^{(1)}_{a_4,a_3,a_2,a_1;4}-\left[R^{(2)}_{a_4,a_3,a_2,a_1;2}\right]^*\\
R_{a_4,a_3,a_2,a_1;r} &= R^{(1)}_{a_4,a_3,a_2,a_1;2}+R^{(1)}_{a_4,a_3,a_2,a_1;3\cdot}-\left[R^{(2)}_{a_4,a_3,a_2,a_1;1}\right]^*
\end{aligned}
\tag{4.24}
$$

It should be noted that the the the rephasing and nonrephasing signals are similar in form to (3.3), *except* for the appearance of the complex conjugate terms. The extra contribution is due to the fact that the model in (1.11) contains a third band of states, whereas the model in chapter 2 considered only two electronic states (if a third state were added, it would be analogous to the third band and the signals in chapter 2 would also contain the extra contributions).

Finally, as in the exact solutions for the two-state model in §3.3, the ORTs are *purely oscillatory*. As a result, a pure dephasing rate constant Γ is introduced in a similar manner (see the discussion following Eqn. (3.26)), only in chapter 2 it was interpreted as electronic dephasing, and in the present case it is meant to represent vibrational dephasing. Thus

$$R_{a_4,a_3,a_2,a_1;j} \rightarrow \exp[-\Gamma(t_1+t_3)]R_{a_4,a_3,a_2,a_1;j} \tag{4.25}$$

4.3 *ab initio* 2DIR Spectra

In this section, the procedure for calculating the nonlinear ORTs using *ab initio* electronic structure inputs is outlined. First, §4.3.1 presents a method for constructing the *ab initio* anharmonic potential energy surfaces that define the molecular Hamiltonian, H_M [28]. The energy levels of the H_M serve as direct input to the ORTs in (4.24), whereas its eigenvectors serve as indirect input by way of the transition dipole moment vectors. Second, §4.3.2 derives an expression for the transition dipole vectors, where quantities obtainable from electronic structure calculations appear explicitly. (4.25)

4.3.1 Field-free Anharmonic Hamiltonian in Normal Coordinates

In general, the basis of harmonic oscillator Fock states $\{|m_1, m_2, \ldots, m_n\rangle\}$ is characterized by the total number of quanta contained in n normal modes, where m_j

denotes the number of quanta in the j-th mode. If the basis is restricted to the subspace spanned by a few normal modes with nearby frequencies, it may be conveniently divided into bands according to the total number of quanta:

- The ground state $|0, ..., 0\rangle$
- A "singly-excited" band of n states, each containing a single quanta $\{|1, ..., 0\rangle, ..., |0, ..., 1\rangle\}$
- A "doubly-excited" band of $n(n+1)/2$ states containing two total quanta, $\{|2, ..., 0\rangle, ..., |0, ..., 2\rangle, ..., |1, 1, ..., 0\rangle, ..., |0, ..., 1, 1\rangle\}$
- etc.

In what follows, this basis will be referred to as the "harmonic basis", and the aim here is to express the field-free multistate Hamiltonian of (1.11) in a such a basis.

For a system of N nuclei, the field-free Hamiltonian in the body-fixed coordinate system may be generally written as:

$$H = \sum_{i=1}^{3N} \frac{p_i^2}{2} + U(q_1, ..., q_{3N}) = \frac{1}{2}\vec{p} \cdot \vec{p} + U(\vec{q}) \tag{4.27}$$

where, $\vec{q} = (q_1, ..., q_{3N})$ and $\vec{p} = (p_1, ..., p_{3N})$. If the potential energy is expanded in a Taylor series around the equilibrium nuclear configuration, $\vec{q} = \vec{0}$, the zero-order term may be dropped without loss of generality, and the first order terms vanish $(\partial U/\partial q_i)_{\vec{q}=\vec{0}} = 0$ since $\vec{q} = \vec{0}$ corresponds to a minimum of the potential energy surface. Hence:

$$U(q_1, ..., q_{3N}) \approx \frac{1}{2!}\sum_{i,j=1}^{3N} U_{ij}^{(2)} q_i q_j + \frac{1}{3!}\sum_{i,j,k=1}^{3N} U_{ijk}^{(3)} q_i q_j q_k + \frac{1}{4!}\sum_{i,j,k,l=1}^{3N} U_{ijkl}^{(4)} q_i q_j q_k q_l + \tag{4.28}$$

where

$$U_{ij}^{(2)} \equiv \left(\frac{\partial^2 U}{\partial q_i \partial q_j}\right)_{\vec{q}=\vec{0}}, U_{ijk}^{(3)} \equiv \left(\frac{\partial^3 U}{\partial q_i \partial q_j \partial q_k}\right)_{\vec{q}=\vec{0}}, U_{ijkl}^{(4)} \equiv \left(\frac{\partial^4 U}{\partial q_i \partial q_j \partial q_k \partial q_l}\right)_{\vec{q}=\vec{0}} \tag{4.29}$$

are the second-, third-, and fourth-order force constants. The transformation to normal coordinates may be outlined in the following steps:

- Express the second order term in matrix form

$$\frac{1}{2!}\sum_{i=1}^{3N}\sum_{j=1}^{3N}U_{ij}^{(2)}q_iq_j=\frac{1}{2}\vec{q}^{T}\mathbf{U}^{(2)}\vec{q}=\frac{1}{2}\left(q_1,q_2,...,q_{3N}\right)\begin{pmatrix}U_{11}^{(2)} & U_{12}^{(2)} & \cdots & U_{1,3N}^{(2)}\\ U_{21}^{(2)} & U_{22}^{(2)} & \cdots & U_{2,3N}^{(2)}\\ \vdots & \vdots & \ddots & \vdots\\ U_{3N,1}^{(2)} & U_{3N,2}^{(2)} & \cdots & U_{3N,3N}^{(2)}\end{pmatrix}\begin{pmatrix}q_1\\ q_2\\ \vdots\\ q_{3N}\end{pmatrix} \tag{4.30}$$

  and identify $\mathbf{U}^{(2)}$ as the Hessian matrix

- Find the orthogonal matrix $\mathbf{A}$ that diagonalizes the Hessian, and the corresponding eigenvalues λ_j

$$\mathbf{A}^{-1}\mathbf{U}\mathbf{A}=\begin{pmatrix}\lambda_1 & \cdots & 0\\ \vdots & \ddots & \vdots\\ 0 & \cdots & \lambda_{3N}\end{pmatrix} \tag{4.31}$$

- Use the matrix $\mathbf{A}$ to find the normal mode coordinates

$$\begin{aligned}\frac{1}{2}\vec{q}^{T}\mathbf{U}^{(2)}\vec{q} &= \frac{1}{2}\left(\mathbf{A}^{-1}\vec{q}\right)^{T}\left(\mathbf{A}^{-1}\mathbf{U}^{(2)}\mathbf{A}\right)\left(\mathbf{A}^{-1}\vec{q}\right)=\frac{1}{2}\sum_{k=1}^{3N-6}\lambda_kQ_k^2 \qquad (4.32)\\ Q_k &= \sum_{j=1}^{3N}A_{kj}^{-1}q_j=\sum_{j=1}^{3N}A_{jk}^{*}q_j;\end{aligned}$$

  and normal mode momenta

$$\begin{aligned}\frac{1}{2}\vec{p}\cdot\vec{p} &= \frac{1}{2}\left(\mathbf{A}^{-1}\vec{p}\right)\cdot\left(\mathbf{A}^{-1}\vec{p}\right)=\frac{1}{2}\vec{P}\cdot\vec{P} \qquad (4.33)\\ P_k &= \sum_{j=1}^{3N}A_{kj}^{-1}p_j=\sum_{j=1}^{3N}A_{jk}^{*}p_j\end{aligned}$$

The $3N-6$ (or $3N-5$ in the case of linear molecules) upper limit of the sum in the last term of (4.32) is because 6 (or 5 in the case of linear molecules) of the components of $\mathbf{A}^{-1}\vec{q}$ would correspond to the center of mass and rotational coordinates. However, these coordinates are stationary in the body-fixed coordinate

system, and are therefore associated with zero eigenvalues. We conveniently assume that the $\lambda_{3N-5} = ... = \lambda_{3N} = 0$ correspond to those degrees of freedom.

The anharmonic terms can also be cast in terms of the normal mode coordinates:

$$\hat{H} = \sum_{i=1}^{3N-6} \frac{1}{2}\left(P_i^2 + \omega_i^2 Q_i^2\right) + \frac{1}{3!}\sum_{i,j,k=1}^{3N-6} \phi_{ijk} Q_i Q_j Q_k + \frac{1}{4!}\sum_{i,j,k,l=1}^{3N-6} \phi_{ijkl} Q_i Q_j Q_k Q_l + \dots \tag{4.34}$$

where $\lambda_k \equiv \omega_k^2$, and

$$\phi_{ijk} \equiv \left(\frac{\partial^3 U}{\partial Q_i \partial Q_j \partial Q_k}\right)_{\vec{Q}=\vec{0}}, \phi_{ijkl} \equiv \left(\frac{\partial^4 U}{\partial Q_i \partial Q_j \partial Q_k \partial Q_l}\right)_{\vec{Q}=\vec{0}}. \tag{4.35}$$

The eigenfunctions and eigenvalues of the harmonic part of the Hamiltonian,

$$H_{har} = \sum_{i=1}^{3N-6} \frac{1}{2}\left(P_i^2 + \omega_i^2 Q_i^2\right) \tag{4.36}$$

are given by:

$$\begin{aligned} |\mathbf{n}\rangle &= |n_1, n_2, ..., n_{3N-6}\rangle \\ \hbar\Omega_{\mathbf{n}} &= n_1\hbar\omega_1 + n_2\hbar\omega_2 + ... + n_{3N-6}\hbar\omega_{3N-6} \end{aligned} \tag{4.37}$$

where $n_1, n_2, ..., n_{3N-6} = 0, 1, 2, 3, \dots$.

The numerical computation of the anharmonic Hamiltonian is facilitated by first transforming it to second quantized normal ordered form, and writing the result in the harmonic basis defined by (4.37). Using the bosonic creation and annhilation operators,

$$\begin{aligned} Q_k &= \sqrt{\frac{\hbar}{2m_k\omega_k}}\left(\hat{a}_k + \hat{a}_k^\dagger\right) \\ P_k &= -i\sqrt{\frac{m_k\hbar\omega_k}{2}}\left(\hat{a}_k - \hat{a}_k^\dagger\right) \end{aligned} \tag{4.38}$$

leads to

$$\hat{H} = \hat{H}_{har} + \sum_{i,j,k=1}^{N_{mode}} U_{ijk} \left[\hat{a}_i \hat{a}_j \hat{a}_k + 3\hat{a}_i^\dagger \hat{a}_j^\dagger \hat{a}_k + 3\hat{a}_i^\dagger \hat{a}_j \hat{a}_k + \hat{a}_i^\dagger \hat{a}_j^\dagger \hat{a}_k^\dagger + 3\left(\hat{a}_i + \hat{a}_i^\dagger\right)\delta_{j,k} \right] + \sum_{i,j,k,l=1}^{N_{mode}} U_{ijkl} \left[\hat{a}_i \hat{a}_j \hat{a}_k \hat{a}_l + 4\hat{a}_i^\dagger \hat{a}_j^\dagger \hat{a}_k^\dagger \hat{a}_l + 6\hat{a}_i^\dagger \hat{a}_j^\dagger \hat{a}_k \hat{a}_l + 4\hat{a}_i^\dagger \hat{a}_j \hat{a}_k \hat{a}_l + \hat{a}_i^\dagger \hat{a}_j^\dagger \hat{a}_k^\dagger \hat{a}_l^\dagger + 6\left(\hat{a}_i \hat{a}_j + \hat{a}_i^\dagger \hat{a}_j^\dagger + 2\hat{a}_i^\dagger \hat{a}_j\right) \right] \tag{4.39}$$

where the summation limits $3N - 6$ have been replaced by N_{mode}, where N_{mode} is the number of modes explicitly accounted for in the computations[4]. In the above, $H_{har} = \sum_k \left(\hat{a}_k^\dagger \hat{a}_k + 1/2\right) \hbar\omega_k$ and

$$\widetilde{\phi}_{ijk} \equiv \frac{\phi_{ijk}}{3!\sqrt{2\omega_i 2\omega_j 2\omega_k}} \ , \ \widetilde{\phi}_{ijkl} \equiv \frac{\phi_{ijkl}}{4!\sqrt{2\omega_i 2\omega_j 2\omega_k 2\omega_l}}. \tag{4.40}$$

The second-order force constants, and hence the normal mode frequencies $\{\omega_k\}$, are obtained directly from the electronic structure Hessian calculations, while the third- and fourth-order force constants are calculated as described in §4.3.3. Once these inputs are known, the matrix representation of $\hat{H}$ in the harmonic basis is easily constructed using creation and annihilation operators

$$\begin{pmatrix} \langle \mathbf{n}_a | H | \mathbf{n}_a \rangle & \langle \mathbf{n}_a | H | \mathbf{n}_b \rangle & \cdots & \cdots \\ \langle \mathbf{n}_b | H | \mathbf{n}_a \rangle & \langle \mathbf{n}_b | H | \mathbf{n}_b \rangle & \cdots & \cdots \\ \vdots & \vdots & \ddots & \\ \vdots & \vdots & & \ddots \end{pmatrix} \begin{pmatrix} C_{j\mathbf{n}_a} \\ C_{j\mathbf{n}_b} \\ \vdots \\ \vdots \end{pmatrix} = E_j \begin{pmatrix} C_{j\mathbf{n}_a} \\ C_{j\mathbf{n}_b} \\ \vdots \\ \vdots \end{pmatrix} \tag{4.41}$$

Diagonalization then leads to the anharmonic energy levels, and corresponding eigenfunctions as linear combinations of the harmonic basis states,

$$|E_j\rangle = \sum_{\mathbf{n}} C_{j,\mathbf{n}} |\mathbf{n}\rangle . \tag{4.42}$$

[4]Chosen as the number of photoactive modes in the preliminary work presented in this chapter.

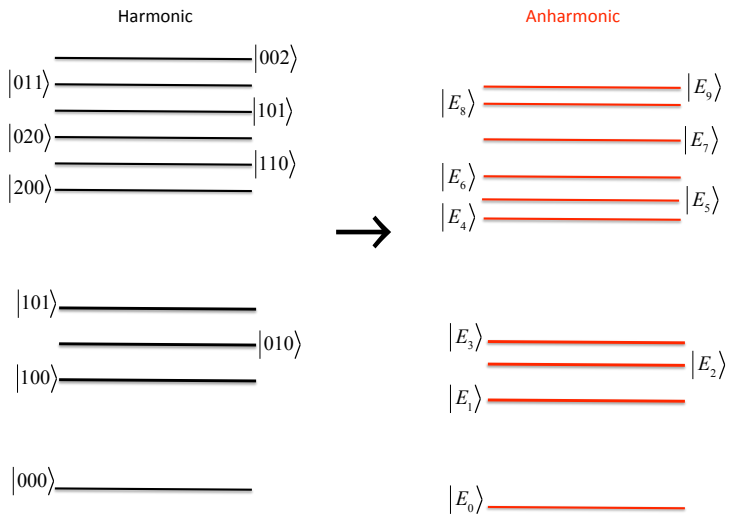

Figure 4.1: Schematic energy level structure for a three-mode system consisting of a ground state, a band of singly-occupied states, and a band of doubly-occupied states. The harmonic basis states $\{|n_1, n_2, n_3\rangle\}$ from (4.37) are show on the left, which the anharmonic basis states $\{|E_k\rangle\}$ from (4.42) are show on the right. The anharmonicity is assumed to not disrupt the gross band structure.

Since the anharmonic terms are usually relatively small, the energy levels of the anharmonic Hamiltonian retain a similar band structure (Figure 4.1 illustrates a three-mode example). Typically, only the first three bands of the anharmonic Hamiltonian contribute to the third-order signal. However, in terms of numerical diagonalization, the energies of excited vibrational states do not converge with this minimal set of basis states, since stabilization of the singly- and doubly-excited bands requires coupling with higher states in higher bands [28]. Consequently, the number of basis states used in the numerical calculations was enlarged until convergence of the singly- and doubly-excited energies was achieved. For example, the minimal number of basis states needed for the the three mode system discussed later in this chapter was 10, but the number required for convergence was 364.

4.3.2 Field-Matter Interaction: Polarized Transition Dipoles

In this section, an expression for the matrix elements of the vector transition dipole moments in the basis of molecular eigenstates, in terms of electronic structure

inputs.

For a neutral molecule consisting of N_e electrons and N_n nuclei, $\sum_{\alpha=1}^{N_n} \zeta_\alpha = N_e$, where ζ_α is the atomic number of the α-th nucleus, and for electronic and nuclear position operators $\vec{r} = (\vec{r}_1, ..., \vec{r}_{N_e})$ and $\vec{R} = \left(\vec{R}_1, ..., \vec{R}_{N_n}\right)$, respectively, the overall dipole moment operator is given by:

$$\overrightarrow{\mu}\left(\vec{r}, \vec{R}\right) = \overrightarrow{\mu}_e\left(\vec{r}\right) + \overrightarrow{\mu}_n\left(\vec{R}\right). \tag{4.43}$$

Here, $\overrightarrow{\mu}_e\left(\vec{r}\right) = -\sum_{j=1}^{N_e} e\vec{r}_j$ and $\sum_{\alpha=1}^{N_n} \zeta_\alpha e\vec{R}_\alpha$ are the electronic and nuclear contributions, respectively. Within the Born-Oppenheimer approximation, the stationary wave functions of the molecule are of the following form:

$$\psi_{s,\sigma}\left(\vec{r}, \vec{R}\right) = \varphi_s\left(\vec{r}; \vec{R}\right) \chi_{s,\sigma}\left(\vec{R}\right) \tag{4.44}$$

where $\varphi_s\left(\vec{r}; \vec{R}\right)$ is the s-th electronic wave function, which is parametrically dependent on $\vec{R}$, and $\chi_{s,\sigma}\left(\vec{R}\right)$ is the σ-th nuclear wave function associated with the s-th electronic state. The matrix elements of the overall dipole moment operator in the stationary state representation are given by:

$$\begin{aligned}\left\langle \psi_{s,\sigma'} \right| \vec{\mu} \left| \psi_{s,\sigma} \right\rangle = & \int d\vec{R} \chi^*_{s,\sigma'}\left(\vec{R}\right) \chi_{s,\sigma}\left(\vec{R}\right) \int d\vec{r} \varphi^*_s\left(\vec{r}; \vec{R}\right) \overrightarrow{\mu}_e(\overrightarrow{r}) \varphi_s\left(\vec{r}; \vec{R}\right) \\ & + \int d\vec{R} \chi^*_{s,\sigma'}\left(\vec{R}\right) \overrightarrow{\mu}_n(\overrightarrow{R}) \chi_{s,\sigma}\left(\vec{R}\right)\end{aligned} \tag{4.45}$$

In the Condon approximation, one neglects the parametric dependence of $\varphi_s\left(\vec{r}; \vec{R}\right)$ on $\vec{R}$ by assuming $\varphi_s\left(\vec{r}; \vec{R}\right) \rightarrow \varphi_s\left(\vec{r}; \vec{R}_0\right) \equiv \varphi_{s,0}\left(\vec{r}\right)$ (i.e., the nuclear configuration is fixed as far as the electronic motions are concerned). Then, using the orthogonality of the nuclear wavefunctions,

$$\left\langle \psi_{s,\sigma'} \right| \vec{\mu} \left| \psi_{s,\sigma} \right\rangle = \left\langle \varphi_{s,0} \right| \mu_e\left(\vec{r}\right) \left| \varphi_{s,0} \right\rangle \delta_{\sigma,\sigma'} + \left\langle \chi_{s,\sigma'} \right| \mu_n\left(\overrightarrow{R}\right) \left| \chi_{s,\sigma} \right\rangle. \tag{4.46}$$

The diagonal matrix elements correspond to the permanent dipole in a given vibrational state, which is responsible for the Stark Shift of the energy levels. However,

since this term is diagonal, it cannot induce transitions between the adiabatic states, and will be assumed to be zero in this work. This assumption is true for a symmetrical molecule such as $Mn_2(CO)_{10}$, and amounts to ignoring the Stark shift in the case of asymmetrical molecules.

If $\vec{R}_\alpha$ is rewritten in the form $\vec{R}_\alpha = \vec{R}_{\alpha 0} + \vec{\delta}_\alpha$, where $\vec{R}_{\alpha 0}$ is the equilibrium configuration and $\vec{\delta}_\alpha$ is the deviation from it, then the off-diagonal elements become

$$\begin{aligned}\langle \psi_{s,\sigma'} | \vec{\mu} | \psi_{s,\sigma} \rangle &= \langle \chi_{s,\sigma'} | \overrightarrow{\mu}_n | \chi_{s,\sigma} \rangle \\ &= \sum_{\alpha=1}^{N_n} \zeta_\alpha e \left[\vec{R}_{0\alpha} \langle \chi_{s,\sigma'} | \chi_{s,\sigma} \rangle + \langle \chi_{s,\sigma'} | \vec{\delta}_\alpha | \chi_{s,\sigma} \rangle \right] \\ &= \sum_{\alpha=1}^{N_n} \zeta_\alpha e \langle \chi_{s,\sigma'} | \vec{\delta}_\alpha | \chi_{s,\sigma} \rangle\end{aligned} \tag{4.47}$$

It should be noted that the transition dipole moment in(4.47) does not include any information on the electronic density. The charges on each atom therefore correspond to the bare nuclear charges, rather than the effective charges. This is a result of the Condon approximation, which assumes that the electronic density does not change when the nuclear positions deviate from their equilibrium configuration. The deviation may be defined as

$$\vec{\delta}_\alpha = \begin{pmatrix} X_\alpha \\ Y_\alpha \\ Z_\alpha \end{pmatrix} = \frac{1}{\sqrt{M_\alpha}} \begin{pmatrix} q_{3\alpha-2} \\ q_{3\alpha-1} \\ q_{3\alpha} \end{pmatrix} \tag{4.48}$$

where $X_\alpha, Y_\alpha, Z_\alpha$ are the Cartesian coordinates, and $q_{3\alpha-2} = \sqrt{M_1} X_1, q_{3\alpha-1} = \sqrt{M_1} Y_1, q_{3\alpha} = \sqrt{M_1} Z_1, ...$ are the corresponding mass-weighted coordinates.

By assuming that s corresponds to the ground electronic state, and the nuclear states $|\chi_{s,\sigma}\rangle$ correspond to the eigenstates $|E_\sigma\rangle$ in (4.42), the dipole matrix elements

become

$$\langle \psi_{s,\sigma'} | \, \vec{\mu} \, | \psi_{s,\sigma} \rangle = \begin{pmatrix} \langle \psi_{s,\sigma'} | \, \mu_x \, | \psi_{s,\sigma} \rangle \\ \langle \psi_{s,\sigma'} | \, \mu_y \, | \psi_{s,\sigma} \rangle \\ \langle \psi_{s,\sigma'} | \, \mu_z \, | \psi_{s,\sigma} \rangle \end{pmatrix} = \sum_{\alpha=1}^{N_n} \frac{\zeta_\alpha e}{\sqrt{M_\alpha}} \begin{pmatrix} \langle E_{\sigma'} | \, q_{3\alpha-2} \, | E_\sigma \rangle \\ \langle E_{\sigma'} | \, q_{3\alpha-1} \, | E_\sigma \rangle \\ \langle E_{\sigma'} | \, q_{3\alpha} \, | E_\sigma \rangle \end{pmatrix}. \quad (4.49)$$

Eqn. (4.49) is the main result of this subsection, where the matrix elements $\langle E_{\sigma'} | \, q_l \, | E_\sigma \rangle$ are easily evaluated using creation and annihilation operators

$$\begin{aligned} \langle E_{\sigma'} | \, q_l \, | E_\sigma \rangle &= \sum_{k=1}^{3N_n} A_{lk} \langle E_{\sigma'} | \, Q_k \, | E_\sigma \rangle \quad (4.50) \\ &= \sum_{k=1}^{3N_n-6} \sum_{\mathbf{n},\mathbf{n}'} A_{lk} C^*_{\sigma',\mathbf{n}'} C_{\sigma,\mathbf{n}} \sqrt{\frac{\hbar}{2\omega_k}} \left[\sqrt{n'_k} \delta \left(n'_k - 1, n_k \right) + \sqrt{n'_k + 1} \delta \left(n'_k + 1, n_k \right) \right], \end{aligned}$$

where $C_{\sigma,\mathbf{n}} = \langle \mathbf{n} | E_\sigma \rangle$, and quantities in red indicate electronic structure inputs.

4.3.3 Electronic Structure Inputs

Geometry optimization and normal mode analysis for $Mn(CO)_5$ was done at the B3LYP[154–157]/LanL2DZ[158–160] level of theory using the quantum chemistry software package Q-Chem 3.1 [161]. The normal mode analysis allowed for the determination of the partial charges ζ_α, reduced masses M_α, normal mode frequencies ω_k and corresponding eigenvectors of the Hessian matrix $\mathbf{A}$, all of which serve as inputs for the transition dipole vectors in (4.49).

Third-order force constants, ϕ_{ijk}, and semidiagonal fourth-order force constants, ϕ_{ijkk} were calculated in terms of the normal-mode coordinates via a finite displacement method [162, 163]. Off-diagonal fourth-order force constants of the type ϕ_{ijkl} have been observed to lead to very small shifts of the energy levels ($\sim$cm$^-$1) and are therefore neglected [164]. More specifically, the second derivatives of the potential energy with respect to the normal mode coordinates $\phi_{ij} = \partial^2 U / \partial Q_i \partial Q_j$ were calculated at the equilibrium geometry as well as at geometries slightly displaced

relative to it. We obtained the displaced configurations by shifting the atoms relative to their equilibrium positions along all 3N-6 normal-mode coordinates in the positive and negative directions. For a given displacement ΔQ_k along the kth mode coordinate, the third-order force constant is given by

$$\phi_{ijk} = \left(\frac{\partial^3 U}{\partial Q_i \partial Q_j \partial Q_k} \right)_{\vec{Q}=\vec{0}} = \frac{\phi_{ij}^{+} - \phi_{ij}^{-}}{2\Delta Q_k} \tag{4.51}$$

where ϕ_{ij}^{+} and ϕ_{ij}^{-} represent the second-order force constants at the positively and negatively displaced geometries, respectively. Similarly, the semidiagonal fourth-order force constants are given by

$$\phi_{ijkk} = \left(\frac{\partial^4 U}{\partial Q_i \partial Q_j \partial Q_k \partial Q_k} \right)_{\vec{Q}=\vec{0}} = \frac{\phi_{ij}^{+} + \phi_{ij}^{-} - 2\phi_{ij}^{0}}{(2\Delta Q_k)^2} \tag{4.52}$$

where $\phi_{ij}^{0} \equiv \phi_{ii}^{0}\delta_{i,j}$. The third- and fourth-order force constants obtained in this manner, along with the normal mode frequencies ω_k, serve as inputs to the anharmonic Hamiltonian in (4.39).

The overall computational scheme may be summarized as follows:

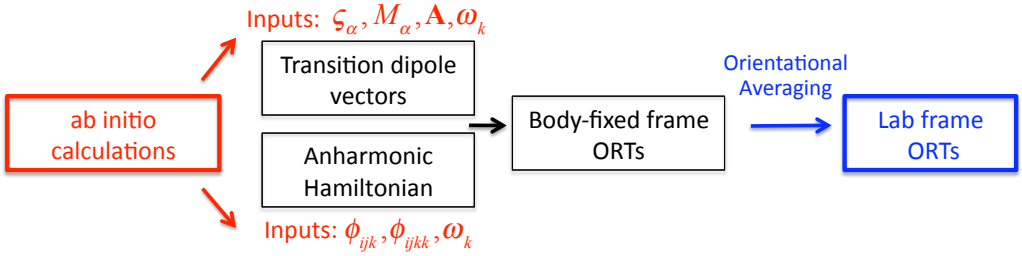

Figure 4.2: A summary of the computational scheme used for the ORTs in (4.24).

4.4 Application to Metal Carbonyl Compound $Mn(CO)_5$

As mentioned in the chapter Introduction, the ultimate aim of this work was to apply the *ab initio* procedure to the compound $Mn_2(CO)_{10}$, whose structure, along with those of its photoproducts, are shown in Figure 4.3. As a first application,

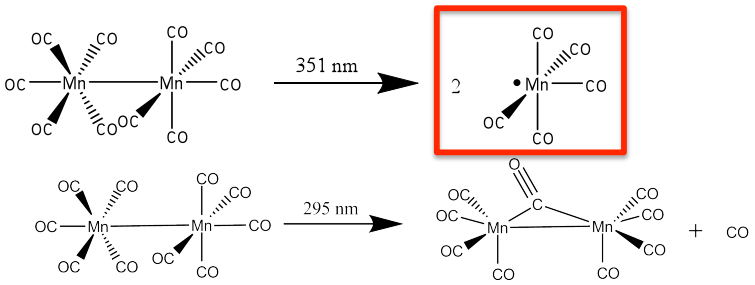

Figure 4.3: Photodissociation of $Mn_2(CO)_{10}$ into its photoproducts $Mn(CO)_5$ and $Mn_2(CO)_9$. The highlighted $Mn(CO)_5$ structure is the focus of this section.

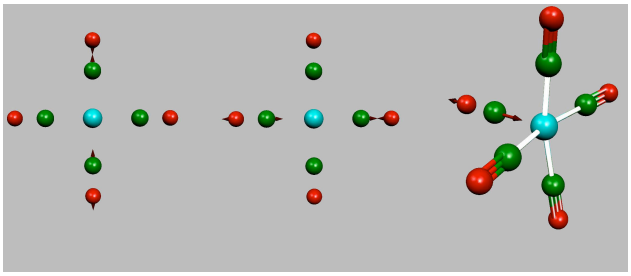

Figure 4.4: The three photoactive CO modes of $Mn(CO)_5$. The Mn atom is shown in light blue, while the C and O atoms are in green and red, respectively.

we applied the photoproduct $Mn(CO)_5$. Although this system consists of five CO stretching modes, three photoactive and two photoinactive, *the results presented here only account for the three photoactive modes*. A schematic of the vibrations of these three modes are shown in Figure 4.4.

4.4.1 Preliminary Results and Discussion

The procedure for calculating the vector transition dipole moment outlined in §4.3.2 was general in that Eqn. (4.49) involved matrix elements between *anharmonic* basis states, $\langle E_{\sigma'}| q_l |E_\sigma\rangle$. As a first approximation, we instead chose to calculate the dipoles in *harmonic* basis using $\langle \mathbf{n}'| q_l |\mathbf{n}\rangle$, which is expected to be a reasonable approximation provided the anharmonicities are relatively small. When applied to $Mn(CO)_5$, this resulted in transition dipoles that were either along the z direction, *or* in the $xy-$plane. Figure 4.5 shows the anharmonic energy levels and all possible

transitions between the three bands: the ground state, the three singly-excited states, and the six doubly-excited states[5].

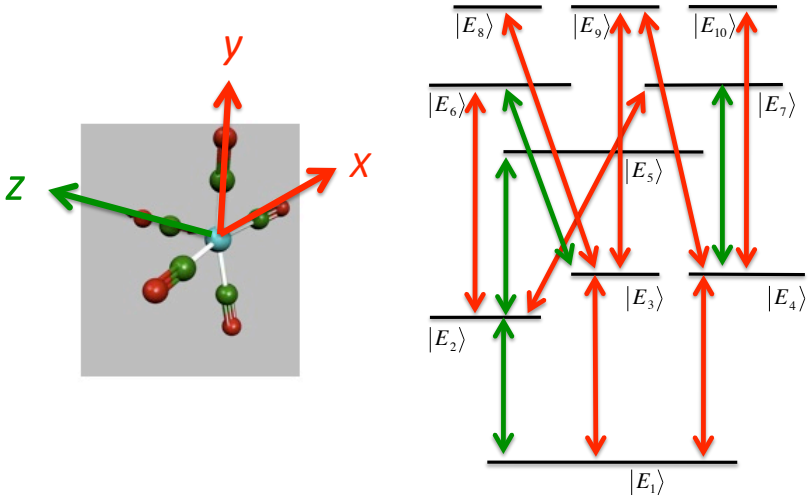

Figure 4.5: Directionality of transition dipole moments in $Mn(CO)_5$. The left panel defines the coordinate axes, with the z axis along the terminal CO group, and the x and y axes near the equitorial CO groups (the equitorial groups are not exactly at 90 degrees to the terminal group). The right panel shows

Figure 4.6 shows the absolute value rephasing spectrum, computed according to (4.24), and is the main result of this section. As indicated in the Figure, the allowed transitions may be correlated with the various peaks in the spectrum, as expected. However, the most important feature of is that *the anharmonic shift of the main diagonal peak is upward*, contrary to what other studies and found and to what was expected. This is a direct consequence of neglecting the coupling between the photoactive and photoinactive CO modes, as noted in the introduction. The same trend is seen in studies on $Mn_2(CO)_{10}$, where ignoring the photoinactive modes[6] results in negative diagonal anharmonic peak shifts (see the red highlighted portion of Table 4.1 in the Introduction).

Although the preliminary results presented here were qualitatively incorrect due to

[5]The number of possible transitions depends on the number of modes included.
[6]In the case of $Mn_2(CO)_{10}$, four of the ten total CO modes are photoactive.

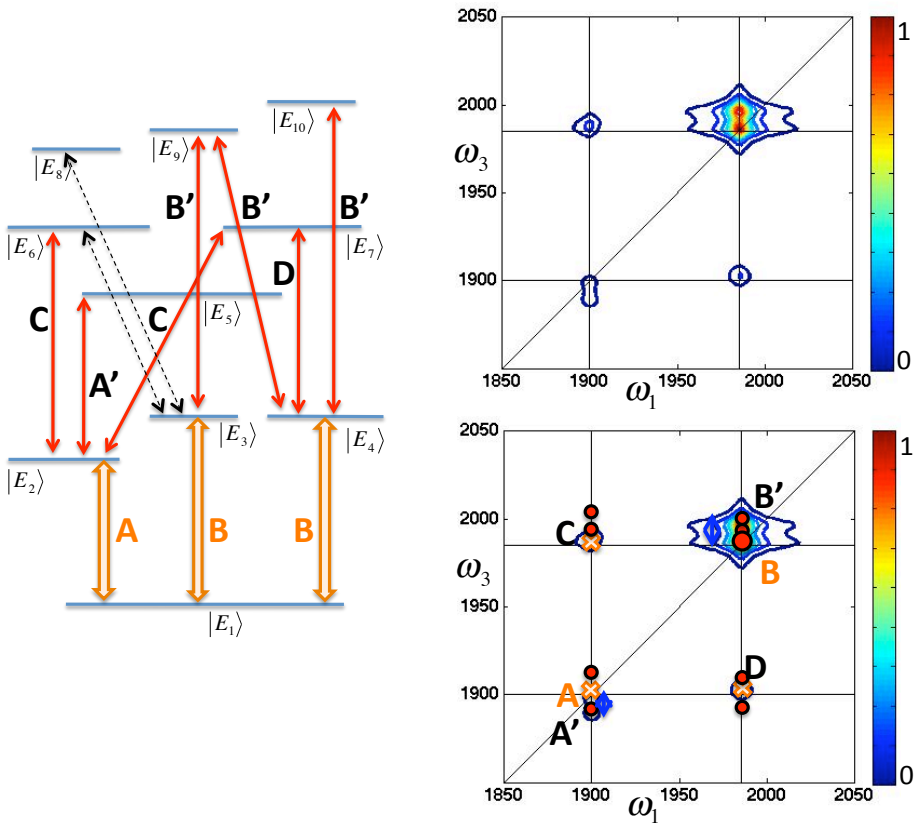

Figure 4.6: Allowed transitions (left) between anharmonic energy levels $\{|E_j\rangle\}$ and lab frame spectrum (right) for $Mn(CO)_5$. In the left panel, orange arrows indicate fundamental transitions, red and dashed black arrows indicate allowed and forbidden transitions, respectively, between states in the singly- and doubly-excited bands. The top right figure is the absolute value rephasing spectrum in the $zzzz$ polarization direction, and a dephasing rate constant of $3cm^{-1}$. The bottom right figure is the same, where the labels indicate which allowed transitions contribute to each peak.

the neglect of the photoinactive modes, the framework established was an important first step toward the computation of more accurate spectra, and was foundational to the later work performed by others in the collaboration.

CHAPTER V

Summary

Chapter 2 focuses on the use of linear chirp to control population transfer between two electronic states, and how control is affected by electronic dephasing. The motivation originates from several experimental studies performed in liquid solution. Although electronic dephasing is expected to be ultrafast and therefore non-negligible on the experimental time scale, the interpretation of such experiments is usually based on dephasing-free models. This chapter discusses the mechanism underlying the control process, and the dephasing is modeled as a Gaussian-Markovian stochastic process. An analysis of the sensitivity of the population transfer to the sign of the linear chirp as a function of the amplitude and correlation time of the frequency fluctuations is provided, along with the details of the simulation techniques used. The key result is that some level of control may be achieved even in the presence of relatively large frequency fluctuations, provided their correlation time is comparable to or shorter than the pulse width in the time domain. Importantly, the results suggest that the choice of methanol as a solvent in the actual experiment played an important role in its success, since the rapid librations in this liquid lead to a particularly short correlation time. Thus, the results reported in this chapter suggest the interesting and rather surprising prediction that the same control strategy will

not be as successful if an aprotic solvent would have been used.

Chapter 3 aims at benchmarking different quantum dynamics methods used for calculating one- and two-dimensional optical spectra. The analysis was performed in the context of a benchmark model that consists of a two-state chromophore with shifted harmonic potential surfaces that differ in frequency. The exact one- and two-dimensional spectra for this system were calculated and compared to spectra calculated via the following approximate methods: (1) The semiclassical forward-backward initial-value representation (FB-IVR) method; (2) The linearized semiclassical (LSC) method; (3) The standard second-order cumulant approximation which is based on the ground-state equilibrium frequency-frequency correlation function (2OC); (4) An alternative second-order cumulant approximation which is able to account for nonequilibrium dynamics on the excited-state potential surface (2OCa). It is shown that all four approximate methods reproduce the exact results when the frequencies of the ground and excited harmonic surfaces are identical, which corresponds to a popular benchmark model. However, by allowing for the ground and excited surfaces to differ in frequency one can obtain a more meaningful benchmark model for which none of the four approximate methods is exact. To the best of my knowledge, the results reported in this chapter represent the first ever comparison of one- and two- dimensional spectra calculated via the above-mentioned approximate methods to the corresponding exact spectra. The accuracy and robustness of the methods are assessed by comparing the spectra as a function of the following parameters: (1) The ratio of excited-state to ground-state frequencies; (2) Temperature; (3) The horizontal displacement of the excited-state potential relative to the ground-state potential; (4) The waiting time between the coherence periods in the case of two-dimensional spectra. The FB-IVR method was found to predict spectra which are

practically indistinguishable from the exact ones over a wide region of parameter space. The LSC method was found to predict spectra which are in good agreement with the exact ones over the same region of parameter space. However, the rather popular 2OC and 2OCa approximations were found to be highly inaccurate unless the frequencies of the ground and excited states were very similar. The significance of these results lies in the fact that this is the first meaningful benchmark study of its kind. The observations discredit the popular approach which is based on the 2OC approximation and give credence to the use of the LSC method for modeling spectra in complex systems, where exact or even FB-IVR-based calculations are prohibitively expensive.

Chapter 4 presents my contribution to a collaborative project that involved an undergraduate student (NickPreketes) and a graduate student from the group of Prof. Kevin Kubarych (CarlosBaiz). The goal of this still ongoing project has been the development of theoretical and computational tools for modeling two-dimensional infrared spectra of polyatomic molecules. My role in this collaboration was to establish the necessary theoretical and computational framework, and subsequently compute the spectra based on *ab initio* input provided by the collaborators. The development was carried out in the context of the molecules $Mn_2(CO)_{10}$ and its photoproducts $Mn(CO)_5$ and $Mn_2(CO)_9$, which were studied by the Kubarych lab. As it turns out, calculating the spectra of these molecules using a nonperturbative approach proved to be prohibitively expensive, and it was therefore necessary to limit the calculation to reduced models. Unfortunately, these reduced models proved to be too oversimplified, and consequently yielded nonphysical results. Later work by Mr. Baiz was able to circumvent this problem by using a perturbative approach. Nevertheless, the methodology presented in this chapter was foundational to the development of the

project and to the work performed by other members in the collaboration after my involvement with the project ceased.

APPENDICES

APPENDIX A

Matrix Exponentials as a Matrix Products

This appendix shows how to rewrite a matrix exponential, such as that appearing in the quantum mechanical propagator, as a product of matrices which is easier to implement numerically. The fact that the algebra differs iin the two cases discussed below is a result of different matrix representations of the matrix in the exponent.

A.1 Exponential of a 2×2 Block-Structured Hermitian Matrix

This section derives an expression for the time evolution operator $\exp\left[-i\hat{H}t/\hbar\right]$ within the grid (spatial) representation. In §2.4.1 from the main text, the propagator for a two-electronic-state system is expressed as a product of matrix exponentials. Here, we focus on the potential energy part of the propagator, where the following matrix appears in the exponent:

$$\begin{aligned} M &\equiv \begin{pmatrix} \hat{V}_g & -\hat{W} \\ -\hat{W}^* & \hat{V}_e \end{pmatrix} \\ &= \hat{V}_g \otimes |g\rangle\langle g| + \hat{V}_e \otimes |e\rangle\langle e| - \hat{W} \otimes |g\rangle\langle e| - \hat{W}^* \otimes |e\rangle\langle g| \end{aligned} \tag{A.1}$$

It should be noted that each of the operators appearing in the four "blocks" of M are *diagonal* in a position representation, which leads to algebraic manipulations analogous to those of a 2×2 matrix of numbers.

We begin by noting that the three Pauli matrices plus the identity matrix $\hat{1}$ form a basis for the Hilbert space of all 2×2 matrices, and for convenience we rewrite them in the notation of the electronic state basis $\{|g\rangle, |e\rangle\}$ as

$$\begin{aligned}
\hat{\sigma}_x &= \begin{pmatrix} 0 & 1 \\ 1 & 0 \end{pmatrix} = |g\rangle\langle e| + |e\rangle\langle g| \\
i\hat{\sigma}_y &= \begin{pmatrix} 0 & 1 \\ -1 & 0 \end{pmatrix} = |g\rangle\langle e| - |e\rangle\langle g| \\
\hat{\sigma}_z &= \begin{pmatrix} 1 & 0 \\ 0 & -1 \end{pmatrix} = |g\rangle\langle g| - |e\rangle\langle e| \\
\hat{1} &= \begin{pmatrix} 1 & 0 \\ 0 & 1 \end{pmatrix} = |g\rangle\langle g| + |e\rangle\langle e| . \qquad \text{(A.2)}
\end{aligned}$$

Expressed in this basis, M becomes

$$M = \frac{\hat{V}_g + \hat{V}_e}{2}\hat{1} - \Re\{W\}\hat{\sigma}_x + \Im\{W\}\hat{\sigma}_y + \frac{\hat{V}_g - \hat{V}_e}{2}\hat{\sigma}_z \qquad \text{(A.3)}$$

and finding the propagator amounts to finding the matrix exponential

$$\begin{aligned}
\exp\left[-iMt/\hbar\right] &= \exp\left[-it\left(\hat{V}_g + \hat{V}_e\right)/4\hbar\right]\hat{1}\exp\left[-it\left(\Re\{W\}\hat{\sigma}_x + \Im\{W\}\hat{\sigma}_y + \frac{\hat{V}_g - \hat{V}_e}{2}\hat{\sigma}_z\right)/2\hbar\right] \\
&\equiv \exp\left[-it\left(\hat{V}_g + \hat{V}_e\right)/4\hbar\right]\hat{1}\exp\left[-itM'/2\hbar\right] \qquad \text{(A.4)}
\end{aligned}$$

We then interpret M' as a psuedo-vector in this space,

$$M' \equiv M_x\hat{\sigma}_x + M_y\hat{\sigma}_y + M_z\hat{\sigma}_z = r\tilde{\sigma_z} \qquad \text{(A.5)}$$

where $\tilde{\sigma_z}$ defines a rotated coordinate system whose z-axis points in the direction of M'. The magnitude and direction of M' are then easily found from A.3 and A.5 as

$$r = \frac{1}{2}\sqrt{\left(\hat{V}_g + \hat{V}_e\right)^2 + 4|W|^2} \qquad \text{(A.6)}$$

$$\tilde{\sigma_z} = \frac{M'}{r} = -\frac{\Re\{W\}}{r}\hat{\sigma}_x + \frac{\Im\{W\}}{r}\hat{\sigma}_y + \frac{\left(\hat{V}_g + \hat{V}_e\right)}{2r}\hat{\sigma}_z \tag{A.7}$$

Using the definitions in J.1, this leads to a matrix expression for second factor in A.4,

$$\begin{aligned} \exp\left[-itM'/2\hbar\right] &= \hat{1}\cos\beta - i\tilde{\sigma_z}\sin\beta \\ &= \begin{pmatrix} \cos\beta + i\frac{\hat{V}_e - \hat{V}_g}{2r}\sin\beta & i\frac{\sin\beta}{r}\left(\Re W + i\Im W\right) \\ i\frac{\sin\beta}{r}\left(\Re W - i\Im W\right) & \cos\beta - i\frac{\hat{V}_e - \hat{V}_g}{2r}\sin\beta \end{pmatrix} \end{aligned} \tag{A.8}$$

and the full propagator is obtained from A.4 as:

$$\begin{aligned} \exp\left[-iMt\right] &= \exp\left[-it\left(\hat{V}_g + \hat{V}_e\right)/4\hbar\right]\hat{1} \\ &\times \begin{pmatrix} \cos\beta + i\frac{\hat{V}_e - \hat{V}_g}{2r}\sin\beta & i\frac{\sin\beta}{r}W \\ i\frac{\sin\beta}{r}W^* & \cos\beta - i\frac{\hat{V}_e - \hat{V}_g}{2r}\sin\beta \end{pmatrix} \end{aligned} \tag{A.9}$$

A.2 Exponential of a General Hermitian Matrix

If $\hat{H}$ is a Hermitian matrix such that $\hat{H}^\dagger = \hat{H}$, then it may be diagonalized by a unitary transformation $\mathcal{U}$ as

$$\hat{\mathcal{U}}\hat{H}\hat{\mathcal{U}}^\dagger = \hat{D} \tag{A.10}$$

where the columns of $\hat{\mathcal{U}}$ are the eigenvectors of $\hat{H}$ and $\hat{D}$ is a diagonal matrix whose diagonal elements are the eigenvalues $\{\lambda_n\}$ of $\hat{H}$. A matrix exponential of the form $\exp\left[-it\hat{H}/\hbar\right]$ may be rewritten by using the property $\hat{\mathcal{U}}\hat{\mathcal{U}}^\dagger$ repeatedly:

$$\begin{aligned} \exp\left[-i\frac{t}{\hbar}\hat{H}\right] &= \hat{\mathcal{U}}\hat{\mathcal{U}}^\dagger \exp\left[-i\frac{t}{\hbar}\hat{H}\right]\hat{\mathcal{U}}\hat{\mathcal{U}}^\dagger \\ &= \hat{\mathcal{U}}\hat{\mathcal{U}}^\dagger\{\hat{1} - \frac{idt}{\hbar}\hat{H} + \frac{1}{2}\left(\frac{idt}{\hbar}\right)^2\hat{H}^2 + \ldots\}\hat{\mathcal{U}}\hat{\mathcal{U}}^\dagger \\ &= \hat{\mathcal{U}}\exp\left[-i\frac{t}{\hbar}\left(\hat{\mathcal{U}}^\dagger\hat{H}\hat{\mathcal{U}}\right)\right]\hat{\mathcal{U}}^\dagger = \hat{\mathcal{U}}\exp\left[-i\frac{t}{\hbar}\hat{D}\right]\hat{\mathcal{U}}^\dagger \end{aligned} \tag{A.11}$$

where the last line follows from (A.10). Then, exploiting the fact that $\hat{D}$ is diagonal leads to

$$\begin{aligned} \exp\left[-i\frac{t}{\hbar}\hat{H}\right] &= \hat{\mathcal{U}}\exp\left[-i\frac{t}{\hbar}\begin{pmatrix}\lambda_1 & & 0\\ & \lambda_2 & \\ 0 & & \ddots\end{pmatrix}\right]\hat{\mathcal{U}}^\dagger \\ &= \hat{\mathcal{U}}\begin{pmatrix}\lambda_1 & & 0\\ & \lambda_2 & \\ 0 & & \ddots\end{pmatrix}\hat{\mathcal{U}}^\dagger \end{aligned} \tag{A.12}$$

APPENDIX B

Transformation of the Hamiltonian to a Rotating Frame

In solving quantum dynamics problems numerically, it is often convenient to transform the Hamiltonian in the Schrödinger picture $\hat{H}_S$ to an arbitrary but judiciously chosen rotating frame where the problem becomes easier to solve. The procedure for finding the Hamiltonian in the rotated from, $\tilde{H}$, is outlined below.

The dynamical equation satisfied by the wave function $|\Psi_S\rangle$ in the Schrödinger picture is

$$i\hbar\frac{\partial\,|\Psi_S\rangle}{\partial t} = \hat{H}_S\,|\Psi_S\rangle \tag{B.1}$$

and the tranformation to the rotating frame may be defined by way of a unitary operator

$$\hat{\mathcal{U}} = \exp\left[-\frac{i}{\hbar}\hat{\mathcal{O}}t\right] \tag{B.2}$$

where $\hat{\mathcal{O}}$ is any Hermitian operator. The wave function is transformed to the rotating frame by

$$|\tilde{\Psi}\rangle = \hat{\mathcal{U}}\,|\Psi\rangle \tag{B.3}$$

This transformation can be used along with (B.1) to find the Hamiltonian in the rotated frame $\tilde{H}$

$$\begin{aligned} i\hbar\frac{\partial\left|\Psi_S\right\rangle}{\partial t} &= i\hbar\frac{\partial}{\partial t}\left(\hat{\mathcal{U}}^\dagger\left|\Psi\right\rangle\right) = i\hbar\left(\frac{\partial}{\partial t}\hat{\mathcal{U}}^\dagger\right)\left|\Psi\right\rangle + i\hbar\hat{\mathcal{U}}^\dagger\frac{\partial}{\partial t}\left(\left|\Psi\right\rangle\right) \\ &= -\hat{\mathcal{O}}\hat{\mathcal{U}}^\dagger\left|\Psi\right\rangle + \hat{\mathcal{U}}^\dagger\hat{H}_S\left|\Psi\right\rangle \\ &= \left(-\hat{\mathcal{O}} + \hat{\mathcal{U}}^\dagger\hat{H}_S\hat{\mathcal{U}}\right)\left(\hat{\mathcal{U}}^\dagger\left|\Psi\right\rangle\right) \end{aligned} \tag{B.4}$$

where the last equality follows from the unitarity of the transformation, $\hat{\mathcal{U}}\hat{\mathcal{U}}^\dagger = \hat{1}$. Thus the equation of motion for the wave function in the rotated frame is

$$i\hbar\frac{\partial\left|\tilde{\Psi}\right\rangle}{\partial t} = \tilde{H}\left|\tilde{\Psi}\right\rangle \tag{B.5}$$

where

$$\tilde{H} = \hat{\mathcal{U}}^\dagger\hat{H}_S\hat{\mathcal{U}} - \hat{\mathcal{O}} \tag{B.6}$$

APPENDIX C

Franck-Condon Coefficients for Shifted Harmonic Oscillator Model

ground state

$$\widehat{H}_g \left|n\right\rangle = \left(n + 1/2\right) \hbar\omega \left|n\right\rangle \tag{C.1}$$

The vibrational eigenstates of $\widehat{H_e}$ are then given by:

$$\exp\left(-\frac{i}{\hbar}\hat{p}x_0\right)\left|n\right\rangle \tag{C.2}$$

Proof:

$$\begin{aligned}
\left\langle x\right| \exp\left(-\frac{i}{\hbar}\hat{p}x_0\right)\left|n\right\rangle &= \int dp \exp\left(-\frac{i}{\hbar}px_0\right)\left\langle x|p\right\rangle \left\langle p|x\right\rangle \\
&= \int dp \exp\left(-\frac{i}{\hbar}px_0\right)\frac{1}{\sqrt{2\pi\hbar}}\left(\frac{i}{\hbar}px\right)\widetilde{\psi}_n\left(p\right) \\
&= \frac{1}{\sqrt{2\pi\hbar}}\int dp \exp\left(\frac{i}{\hbar}p\left(x - x_0\right)\right)\widetilde{\psi}_n\left(p\right) \\
&= \psi_n\left(x - x_0\right)
\end{aligned} \tag{C.3}$$

The FC coefficient is then given by:

$$\begin{aligned}
S_{n.n'} &= \left\langle n'_g|n_e\right\rangle = \left\langle n'\right| \exp\left(-\frac{i}{\hbar}\hat{p}x_0\right)\left|n\right\rangle \\
&= \frac{1}{\sqrt{n!}}\frac{1}{\sqrt{n'!}}\left\langle 0\right| \hat{a}^{n'} \exp\left(-\frac{i}{\hbar}\hat{p}x_0\right)\left(\hat{a}^{\dagger}\right)^n\left|0\right\rangle \\
&= \frac{1}{\sqrt{n!}}\frac{1}{\sqrt{n'!}}\left\langle 0\right| \hat{a}^{n'} \exp\left[\xi_0\left(\hat{a}^{\dagger} - \hat{a}\right)\right]\left(\hat{a}^{\dagger}\right)^n\left|0\right\rangle
\end{aligned} \tag{C.4}$$

where $\xi_0 \equiv \sqrt{\frac{m\omega}{2\hbar}} x_0$ and the last equality follows from $\hat{p} = i\sqrt{\frac{m\omega}{2\hbar}}\left(\hat{a}^\dagger - \hat{a}\right)$.

Further, the exponent in (C.4) may be rewritten according to the Baker-Hausdorff theorem,

$$\exp\left(\hat{A}+\hat{B}\right) = \exp\left(\hat{A}\right)\exp\left(\hat{B}\right)\exp\left(-\frac{1}{2}\left[\hat{A},\hat{B}\right]\right) \tag{C.5}$$

$$\text{for} \quad \left[\hat{A},\left[\hat{A},\hat{B}\right]\right] = \left[\hat{B},\left[\hat{A},\hat{B}\right]\right] = 0 \tag{C.6}$$

which leads to

$$\begin{aligned} S_{n.n'} &= \frac{1}{\sqrt{n!}}\frac{1}{\sqrt{n'!}}\exp\left(\frac{\xi_0^2}{2}\right)\langle 0|\,\hat{a}^{n'}\exp\left(-\xi_0\hat{a}\right)\exp\left(\xi_0\hat{a}^\dagger\right)\left(\hat{a}^\dagger\right)^n|0\rangle \\ &= \frac{1}{\sqrt{n!}}\frac{1}{\sqrt{n'!}}\exp\left(\frac{\xi_0^2}{2}\right)\left[\frac{d^{n'+n}}{d\eta^{n'}d\lambda^n}\langle 0|\exp\left(\eta\hat{a}\right)\exp\left(\lambda\hat{a}^\dagger\right)|0\rangle\right]_{\eta=-\xi_0,\lambda=\xi_0} \end{aligned} \tag{C.7}$$

Next consider

$$\begin{aligned} \langle 0|\exp\left(\eta\hat{a}\right)\exp\left(\lambda\hat{a}^\dagger\right)|0\rangle &= \exp\left(\lambda\eta\right)\langle 0|\exp\left(\lambda\hat{a}^\dagger\right)\exp\left(\eta\hat{a}\right)|0\rangle \\ &= \exp\left(\lambda n\right) \end{aligned} \tag{C.8}$$

Where we have used $a|0\rangle = \langle 0|\,a^\dagger = 0$ and $\exp\left(\hat{A}\right)\exp\left(\hat{B}\right) = \exp\left(\hat{B}\right)\exp\left(\hat{A}\right)\exp\left(\left[\hat{A},\hat{B}\right]\right)$

Hence,

$$\frac{d^{n'+n}}{d\eta^{n'}d\lambda^n}\langle 0|\exp\left(\eta\right)\exp\left(\lambda^\dagger\right)|0\rangle = \frac{d^{n'+n}}{d\eta^{n'}d\lambda^n}\exp\left(\lambda\eta\right) = \frac{d^n}{d\lambda^n}\lambda^{n'}\exp\left(\lambda\eta\right) \tag{C.9}$$

As a final simplification, we may apply the Leibnitz rule

$$\left(f\cdot g\right)^{(n)} = \sum_{k=0}^{n}\begin{pmatrix} n \\ k \end{pmatrix} f^{(k)}g^{(n-k)} \tag{C.10}$$

to find

$$\begin{aligned} \frac{d^n}{d\lambda^n}\lambda^{n'}\exp\left(\lambda\eta\right) &= \left[\lambda^{n'}\exp\left(\lambda\eta\right)\right]^{(n)} = \sum_{k=0}^{n}\begin{pmatrix} n \\ k \end{pmatrix}\left(\lambda^{n'}\right)^{(k)}\eta^{n-k}\exp\left(\lambda\eta\right) \\ &\rightarrow \exp\left(-\xi_0^2\right)\sum_{k=0}^{n}\begin{pmatrix} n \\ k \end{pmatrix}\left(-\xi_0\right)^{n-k}\left(\lambda^{n'}\right)^{(k)} \end{aligned} \tag{C.11}$$

Thus final form is

$$S_{n.n'} = \frac{1}{\sqrt{n!}} \frac{1}{\sqrt{n'!}} \exp\left(-\frac{\xi_0^2}{2}\right) \left[\sum_{k=0}^{n} \begin{pmatrix} n \\ k \end{pmatrix} (-\xi_0)^{n-k} \frac{d^k}{d\lambda^k} \left(\lambda^{n'}\right)\right]_{\lambda=\xi_0} \tag{C.12}$$

APPENDIX D

Calculation of Orientational Tensor Elements

The transformation between the stationary laboratory coordinate system, $\{x, y, z\}$, and time-dependent body-fixed coordinate system $\{x'(t), y'(t), z'(t)\}$ is conveniently given in terms of explicitly time dependent Euler angles $\Omega_t = \{\alpha_t, \beta_t, \gamma_t\}$ [153]:

$$
\begin{aligned}
T_{x,x'} &= \cos\gamma_t \cos\beta_t \cos\alpha_t - \sin\gamma_t \sin\alpha_t \qquad \text{(D.1)}\\
T_{x,y'} &= -\sin\gamma_t \cos\beta_t \cos\alpha_t - \cos\gamma_t \sin\alpha_t\\
T_{x,z'} &= \sin\beta_t \cos\alpha_t\\
T_{y,x'} &= \cos\gamma_t \cos\beta_t \sin\alpha_t + \sin\gamma_t \cos\alpha_t\\
T_{y,y'} &= -\sin\gamma_t \cos\beta_t \sin\alpha_t + \cos\gamma_t \cos\alpha_t\\
T_{y,z'} &= \sin\beta_t \sin\alpha_t\\
T_{z,x'} &= -\cos\gamma_t \sin\beta_t\\
T_{z,y'} &= \sin\gamma_t \sin\beta_t\\
T_{z,z'} &= \cos\beta_t
\end{aligned}
$$

The orientational tensors can be computed in different ways:

- Numerically, by simulating the rotational motion. For example, one can compute the tensor elements by following the motion of a body-fixed coordinate

system throughout a molecular dynamics simulation or a stochastic simulation.

- Analytically, by assuming that the rotational motion is governed by a simple diffusion equation. For example, for linear response:

$$\begin{aligned} Y_{b_2,b_1}^{a_2,a_1}(t_1) &= \left\langle T_{a_2,b_2(t_1)} T_{a_1,b_1(0)} \right\rangle_{eq} = \left\langle T_{a_2,b_2}\left[\Omega(t_1)\right] T_{a_1,b_1}\left[\Omega(0)\right] \right\rangle_{eq} \\ &= \int d\Omega_0 P_{eq}(\Omega_0)\, G(\Omega_1, t_1|\Omega_0, 0)\, T_{a_1,b_1}[\Omega_0]\, T_{a_2,b_2}[\Omega_1] \\ &\equiv \int_0^{2\pi} d\alpha_0 \int_0^{2\pi} d\gamma_0 \int_0^{\pi} d\beta_0 \sin\beta_0 \frac{1}{8\pi^2} G(\Omega_1, t_1|\Omega_0, 0)\, T_{a_1,b_1}[\Omega_0]\, T_{a_2,b_2}[\Omega_1] \end{aligned} \tag{D.2}$$

If the conditional probability $G(\Omega_1, t_1|\Omega_0, 0)$ is known explicitly (e.g, see [152]) one can compute those integrals.

APPENDIX E

Time-Evolution Operator for a Time-Dependent Hamiltonian

The time evolution of the state vector $|\psi(t)\rangle$ is dictated by the time-dependent Schrödinger equation:

$$i\hbar\frac{d}{dt}|\psi(t)\rangle = \widehat{H}(t)|\psi(t)\rangle \tag{E.1}$$

where $\widehat{H}(t)$ is the Hamiltonian operator, which must be hermitian and may or may not be explicitly time-dependent. The time evolution operator is defined as the unitary (norm-preserving) transformation between the state vector at time t_0 to that at time t as $|\psi(t)\rangle = \widehat{U}(t,t_0)|\psi(t,t_0)\rangle$, and upon substitution into (E.1) leads to

$$i\hbar\frac{d}{dt}\widehat{U}(t,t_0)|\psi(t_0)\rangle = \widehat{H}(t)\widehat{U}(t,t_0)|\psi(t_0)\rangle \tag{E.2}$$

Using the fact that this equation must hold for any initial state $|\psi(t_0)\rangle$ leads to an equation of motion for the time evolution operator:

$$i\hbar\frac{d}{dt}\widehat{U}(t,t_0) = \widehat{H}(t)\widehat{U}(t,t_0) \tag{E.3}$$

Using the fact that $\widehat{U}(t_0, t_0) = \hat{I}$, the solution to this equation yields

$$\widehat{U}(t, t_0) = \widehat{I} - \frac{i}{\hbar} \int_{t_0}^{t} dt_1 \widehat{H}(t_1) \widehat{U}(t_1, t_0) \tag{E.4}$$

By repeatedly substituting the left side into the integrand on the right side, Eq. (E.4) may be solved iteratively to give

$$\begin{aligned} \widehat{U}(t, t_0) &= \widehat{I} + \sum_{n=1}^{\infty} \left(-\frac{i}{\hbar} \right)^n \int_{t_0}^{t} dt_n \int_{t_0}^{t_n} dt_{n-1} \cdots \int_{t_0}^{t_2} dt_1 \widehat{H}(t_n) \widehat{H}(t_{n-1}) \cdots \widehat{H}(t_1) \\ &\equiv \exp_+ \left[-\frac{i}{\hbar} \int_{t_0}^{t} dt_1 \widehat{H}(t_1) \right] \end{aligned} \tag{E.5}$$

Following a similar procedure, it may also be shown that $\widehat{U}^{\dagger}(t, t_0) = \exp_- \left[\frac{i}{\hbar} \int_{t_0}^{t} dt_1 \widehat{H}(t_1) \right]$. Although (E.5) is the most general form of the time evolution operator, the following two special cases of interest. First, if $\widehat{H}$ is independent of time, the time-ordering is inconsequential and

$$\widehat{U}(t, t_0) = \exp \left[-\frac{i}{\hbar} \widehat{H}(t - t_0) \right] \tag{E.6}$$

Second, if $\widehat{H}(t)$ but commutes with itself at different times, $\left[\widehat{H}(t_1), \widehat{H}(t_2) \right] = 0$, then

$$\widehat{U}(t, t_0) = \exp \left[-\frac{i}{\hbar} \int_{t_0}^{t} dt' \widehat{H}(t') \right] \tag{E.7}$$

APPENDIX F

Second Order Cumulant Expansions

Consider $\varphi(\lambda) = \langle \exp(i\lambda x) \rangle$, where x is a random variable and λ is a book-keeping parameter to be set to 1 at the end of the derivation. We assume $\varphi(\lambda)$ may be written as the exponential of an analytic function $\psi(\lambda)$, so that

$$\begin{aligned} \varphi(\lambda) &= \exp[\psi(\lambda)] \equiv \exp\left[\psi^{(1)}\lambda + \psi^{(2)}\lambda^2 + ...\right] \\ &= 1 + \left[\psi^{(1)}\lambda + \psi^{(2)}\lambda^2 + ...\right] + \frac{1}{2!}\left[\psi^{(1)}\lambda + \psi^{(2)}\lambda^2 + ...\right]^2 + ... \\ &= 1 + \psi^{(1)}\lambda + \left[\psi^{(2)} + \frac{1}{2}\left(\psi^{(1)}\right)^2\right]\lambda^2 + ... \end{aligned} \tag{F.1}$$

where it should be noted that $\varphi(\lambda = 0) = 1$ implies that $\psi^{(0)} = 0$. At the same time, the fact that $\left[d^n\varphi/d\lambda^n\right]_{\lambda=0} = i^n \langle x^n \rangle$ implies that

$$\varphi(\lambda) = \sum_{n=0}^{\infty} \frac{i^n \langle x^n \rangle}{n!}\lambda^n = 1 + i\langle x \rangle \lambda - \frac{1}{2}\langle x^2 \rangle \lambda^2 + ... \tag{F.2}$$

Explicit expressions for $\psi^{(n)}$ can be obtained by comparing (F.1) and (F.2), order by order:

$$\begin{aligned} \psi^{(1)} &= i\langle x \rangle \\ \psi^{(2)} &+ \frac{1}{2}\left(\psi^{(1)}\right)^2 = -\frac{1}{2}\langle x^2 \rangle \Rightarrow \psi^{(2)} = -\frac{1}{2}\left(\langle x^2 \rangle - \langle x \rangle^2\right) \\ &\vdots \end{aligned} \tag{F.3}$$

Hence

$$\langle \exp(ix) \rangle = \exp\left[i\langle x \rangle - \frac{1}{2}\left(\langle x^2 \rangle - \langle x \rangle^2\right) + ...\right] \tag{F.4}$$

APPENDIX G

Harmonic Oscillator Thermal Expectation Values

To derive expressions for the thermal expectation values that appear in the 2OC and 2OCa approximations, we first express the position and momentum operators in terms of creation and annihilation operators as $\hat{a}, \hat{a}^\dagger$

$$\hat{Q} = \sqrt{\frac{\hbar}{2m\omega_g}}\left(\hat{a} + \hat{a}^\dagger\right) \quad ; \quad \hat{P} = -i\sqrt{\frac{m\hbar\omega_g}{2}}\left(\hat{a} - \hat{a}^\dagger\right) \tag{G.1}$$

By using the standard relations for the action of the creation and annihilation operators on the harmonic oscillator stationary states $\{|n\rangle\}$, $\hat{a}^\dagger|n\rangle = \sqrt{n+1}\,|n+1\rangle$ and $\hat{a}\,|n\rangle = \sqrt{n}\,|n-1\rangle$ we may express the expectation values appearing in the cumulant approximations in terms of $\langle\hat{N}\rangle$ and $\langle\hat{N}^2\rangle$.

$$\left\langle\hat{N}\right\rangle = \frac{1}{e^{\beta\hbar\omega_g} - 1} \quad ; \quad \left\langle\hat{N}^2\right\rangle = \frac{e^{\beta\hbar\omega_g} + 1}{\left(e^{\beta\hbar\omega_g} - 1\right)^2} \tag{G.2}$$

Thus the quadratic terms are

$$\begin{aligned} \langle\hat{Q}^2\rangle &= \frac{\hbar}{2m\omega_g}\left(2\langle\hat{N}\rangle + 1\right); \left\langle\hat{P}^2\right\rangle = \frac{m\omega_g\hbar}{2}\left(2\langle\hat{N}\rangle + 1\right) \\ \langle\hat{Q}\hat{P}\rangle &= \frac{i\hbar}{2}; \langle\hat{P}\hat{Q}\rangle = -\frac{i\hbar}{2} \end{aligned} \tag{G.3}$$

and the quartic terms are

$$
\begin{aligned}
\left\langle \hat{Q}^4 \right\rangle &= \left(\frac{\hbar}{2m\omega_g}\right)^2 3\left(2\langle \hat{N}^2\rangle + 2\langle \hat{N}\rangle + 1\right) \qquad \text{(G.4)}\\
\left\langle \hat{P}^4 \right\rangle &= \left(\frac{m\omega_g\hbar}{2}\right)^2 3\left(2\langle \hat{N}\rangle^2 + 2\langle \hat{N}\rangle + 1\right)\\
\left\langle \hat{Q}^2\hat{P}^2 \right\rangle &= \left\langle \hat{P}^2\hat{Q}^2 \right\rangle = \frac{\hbar^2}{4}\left(2\langle \hat{N}^2\rangle + 2\langle \hat{N}\rangle - 1\right)\\
\left\langle \hat{Q}\hat{P}\hat{Q}\hat{P} \right\rangle &= \left\langle \hat{P}\hat{Q}\hat{P}\hat{Q} \right\rangle = \frac{\hbar^2}{4}\left(2\langle \hat{N}^2\rangle + 2\langle \hat{N}\rangle + 1\right)\\
\left\langle \hat{Q}\hat{P}^2\hat{Q} \right\rangle &= \left\langle \hat{P}\hat{Q}^2\hat{P} \right\rangle = \frac{\hbar^2}{4}\left(2\langle \hat{N}^2\rangle + 2\langle \hat{N}\rangle + 3\right)\\
\left\langle \hat{Q}^3\hat{P} \right\rangle &= i\frac{3\hbar^2}{4m\omega_g}\left(2\langle \hat{N}\rangle + 1\right)\\
\left\langle \hat{P}^3\hat{Q} \right\rangle &= -i\frac{3m\omega_g\hbar^2}{4}\left(2\langle \hat{N}\rangle + 1\right)\\
\left\langle \hat{P}\hat{Q}^3 \right\rangle &= -i\frac{3\hbar^2}{4m\omega_g}\left(2\langle \hat{N}\rangle + 1\right)\\
\left\langle \hat{Q}\hat{P}^3 \right\rangle &= i\frac{3m\omega_g\hbar^2}{4}\left(2\langle \hat{N}\rangle + 1\right)\\
\left\langle \hat{Q}^2\hat{P}\hat{Q} \right\rangle &= i\frac{\hbar^2}{4m\omega_g}\left(2\langle \hat{N}\rangle + 1\right)\\
\left\langle \hat{P}^2\hat{Q}\hat{P} \right\rangle &= -i\frac{m\omega_g\hbar^2}{4}\left(2\langle \hat{N}\rangle + 1\right)\\
\left\langle \hat{Q}\hat{P}\hat{Q}^2 \right\rangle &= -i\frac{\hbar^2}{4m\omega_g}\left(2\langle \hat{N}\rangle + 1\right)\\
\left\langle \hat{P}\hat{Q}\hat{P}^2 \right\rangle &= i\frac{m\omega_g\hbar^2}{4}\left(2\langle \hat{N}\rangle + 1\right)
\end{aligned}
$$

APPENDIX H

Linear response in the same-frequency case

In this appendix,we show that FB-IVR, LSC, 2OC and 2OCa all reproduce the exact 1D spectra when $\omega_e = \omega_g \equiv \omega$. We start out by noting that in this case, the transition frequency is linear in $\hat{Q}$ (see Eqn. (3.11)): $\hat{U} = \hbar\omega_{eg}^v + \sqrt{2S}\hbar\omega\hat{Q} \equiv \hbar\omega_{eg}^v + \delta\hat{U}$, where $\omega_{eg}^v = \omega_{eg} + \omega S$ is the vertical transition frequency, $\delta\hat{U} \equiv \sqrt{2S}\hbar\omega\hat{Q}$ is the fluctuation relative to it, and $S \equiv \omega Q_d^2/2\hbar$ is the Huang-Rhys factor. In the Heisenberg picture, $\delta\hat{U}_{g/e}(t) = \sqrt{2S}\hbar\omega\hat{Q}_{g/e}(t)$, where $\hat{Q}_{g/e}(t)$ is obtained by solving the Heisenberg equations for the position operator on the ground and excited potential surfaces:

$$\hat{Q}_g(t) = \hat{Q}\cos(\omega t) + \frac{\hat{P}}{\omega}\sin(\omega t) \ , \tag{H.1}$$

$$\hat{Q}_e(t) = Q_d + (\hat{Q} - Q_d)\cos(\omega t) + \frac{\hat{P}}{\omega}\sin(\omega t) \ . \tag{H.2}$$

As is well known, the 2OC approximation reproduces the exact result when $\omega_e = \omega_g$:[84]

$$\begin{aligned} J(t_1) &= J^{2OC}(t_1) \\ &= |\mu_{ge}|^2 \exp\left\{-i\omega_{eg}^v t_1 - S\left[\coth\left(\frac{\beta\hbar\omega}{2}\right)(1-\cos(\omega t_1)) + i\left(\sin(\omega t_1) - \omega t_1\right)\right]\right\} \ . \end{aligned} \tag{H.3}$$

However, it can also be shown that, in this case, $J^{2OCa}(t_1)$ also coincides with $J^{2OC}(t_1)$, and hence the exact result. To this end, it can be easily verified that

$$\langle\delta\hat{U}_e(t)\rangle_g = -2\hbar\omega S[1-\cos(\omega t)] \tag{H.4}$$

and

$$\begin{aligned}\langle\delta\hat{U}_e(t')\delta\hat{U}_e(t'')\rangle_g &= 2S\hbar^2\omega^2\left\{2S[1-\cos(\omega t')-\cos(\omega t'')+\cos(\omega t')\cos(\omega t'')]\right.\\ &+\frac{1}{2}\coth\left(\frac{\beta\hbar\omega}{2}\right)[\cos(\omega t')\cos(\omega t'')+\sin(\omega t')\sin(\omega t'')]\\ &\left.+\frac{i}{2}[\cos(\omega t')\sin(\omega t'')-\sin(\omega t')\cos(\omega t'')]\right\}\ . \qquad \text{(H.5)}\end{aligned}$$

Upon substitution of Eqs. (H.4) and (H.5) into Eq. (3.88), performing the integrals explicitly and rearranging, one finds that $J^{2OCa}(t_1)$ indeed reduces to Eq. (H.4).

The FB-IVR approximation is exact when $\omega_e = \omega_g$ since the two surfaces share the same set of coherent states. More specifically, starting with a coherent wave packet on the ground state potential surface guarantees that it will remain coherent even after hopping to the excited state potential energy surface, thereby reproducing the exact result.

Although less obvious, the LSC approximation also turns out to be exact when $\omega_e = \omega_g$. This can be verified explicitly by substituting the well known expression for the Wigner distribution that corresponds to thermal equilibrium on the ground state harmonic potential surface [165],

$$\rho_{g,W}(Q_0,P_0) = \frac{1}{\pi\hbar}\tanh\left(\frac{\beta\hbar\omega}{2}\right)\exp\left\{-\frac{2}{\hbar\omega}\tanh\left(\frac{\beta\hbar\omega}{2}\right)\left[\frac{P_0^2}{2}+\frac{1}{2}\omega^2Q_0^2\right]\right\}\ , \quad \text{(H.6)}$$

into Eq. (3.54), and solving for Q_τ on the average potential energy surface, $V_{ge}(Q) = \frac{1}{2}\omega^2\left(Q-Q_d/2\right)^2 + \text{const.}$, so that

$$\int_0^{t_1} d\tau\delta U(Q_\tau) = -Q_dQ_0\omega\sin(\omega t_1) - Q_dP_0\left[1-\cos(\omega t_1)\right] + S\left[\omega t_1 - \sin(\omega t_1)\right]\ . \quad \text{(H.7)}$$

Substitution of Eqs. (H.6) and (H.7) into Eq. (3.54) followed by explicit integration over Q_0 and P_0 is then found to reproduce the exact $J(t_1)$, Eq. (H.4), thereby implying that the linearization of the forward-backward action is exact when $\omega_e = \omega_g$.

Finally, although the derivation is significantly more cumbersome, it can be similarly shown that, in the case $\omega_e = \omega_g$, FB-IVR, LSC, 2OC and 2OCa all reproduce the exact third-order ORFs, $\{R_1, R_2, R_3, R_4\}$, that underly the 2D spectra. It should also be pointed out that FB-IVR, LSC, 2OC still produce the exact linear and nonlinear ORFs when the model is extended to include an arbitrary number of independent harmonic photo-inactive modes (which is equivalent to the popular Brownian oscillator model[84]).

APPENDIX I

The Linearized Semiclassical Approximation (LSC)

Consider the following general non-adiabatic two-time correlation function:

$$C_{AB}(t) = \mathrm{Tr}_n(\hat{A}e^{i\hat{H}_e t/\hbar}\hat{B}e^{-i\hat{H}_g t/\hbar}). \tag{I.1}$$

The correlation function in Eq. (**??**) is obviously of this type, with $\hat{A} = \hat{V}_{ge}e^{-\beta\hat{H}_e}/Z_e$ and $\hat{B} = \hat{V}_{eg}$. For the sake of simplicity, the direct linearization approximation will be derived below for the case of a single particle of mass m, which moves in 1D.

The *exact* path integral expression for $C_{AB}(t)$ is given by

$$\begin{aligned} C_{AB}(t) &= \left(\frac{m}{2\pi\hbar\epsilon}\right)^N \int dx_0^+ \cdots \int dx_N^+ \int dx_0^- \cdots \int dx_N^- \langle x_0^+|\hat{A}|x_0^-\rangle \\ &\quad \langle x_N^-|\hat{B}|x_N^+\rangle e^{i(S_N^+ - S_N^-)/\hbar} \, . \end{aligned} \tag{I.2}$$

Here,

$$\begin{aligned} S_N^+ &= \sum_{j=0}^{N-1} \epsilon \left[\frac{1}{2}m\left(\frac{x_{j+1}^+ - x_j^+}{\epsilon}\right)^2 - V_g(x_j^+)\right] \, , \\ S_N^- &= \sum_{j=0}^{N-1} \epsilon \left[\frac{1}{2}m\left(\frac{x_{j+1}^- - x_j^-}{\epsilon}\right)^2 - V_e(x_j^-)\right] \, , \end{aligned} \tag{I.3}$$

are the forward and backward actions, respectively, and $\{0, \epsilon, 2\epsilon, \ldots, N\epsilon = t\}$ corresponds to the discretized time (the limit $N \to \infty$ will be imposed at a later stage).

The linearization approximation is based on the assumption that the most important contributions to the path integral in Eq. (I.2) come from forward and backward

trajectories which are infinitesimally close to each other. Thus, one may expand the FB action, $S_N^+ - S_N^-$, to first order with respect to the difference between the forward and backward trajectories. [110, 111, 121–127] To this end, we change the integration variables in Eq. (I.2) from $x_0^+, \ldots, x_N^+, x_0^-, \ldots, x_N^-$ into $y_0, \ldots, y_N, z_0, \ldots, z_N$, such that

$$y_j = \frac{1}{2}(x_j^+ + x_j^-) \ , \ z_j = x_j^+ - x_j^- \ . \tag{I.4}$$

The linearization approximation is then introduced by expanding the FB action, $S_N^+ - S_N^-$, to first order in $z_0, \ldots, z_N$. This yields:

$$\begin{aligned} S_N^+ - S_N^- &\approx \epsilon \sum_{j=0}^{N-1} \left[\frac{m}{\epsilon^2}(y_{j+1} - y_j)(z_{j+1} - z_j) - V'_{av}(y_j) z_j + U(y_j) \right] \\ &= \epsilon \sum_{j=1}^{N-1} z_j \left[\frac{m}{\epsilon^2}(2y_j - y_{j-1} - y_{j+1}) - V'_{av}(y_j) + U(y_j) \right] \\ &\quad + \epsilon z_0 \left[-\frac{m}{\epsilon^2}(y_1 - y_0) - V'_{av}(y_0) + U(y_0) \right] + \epsilon z_N \frac{m}{\epsilon^2}(y_N - y_{N-1}) \ , \end{aligned} \tag{I.5}$$

where,

$$V_{av}(y) = \frac{1}{2}\left[V_g(y) + V_e(y) \right] \tag{I.6}$$

is the arithmetic average of the ground and excited electronic potential surfaces, and

$$U(y) = V_e(y) - V_g(y) \tag{I.7}$$

is the difference between them.

Following the linearization, one can perform the integration over $z_1, \ldots, z_{N-1}$ explicitly, by using the following identity:

$$\int dz_j e^{-i\epsilon \left[\frac{m}{\epsilon^2}(y_{j+1} - 2y_j + y_{j+1}) + V'_{av}(y_j) \right] z_j / \hbar} = \frac{2\pi\hbar}{\epsilon} \delta \left[\frac{m}{\epsilon^2}(y_{j+1} - 2y_j + y_{j+1}) + V'_{av}(y_j) \right] \ . \tag{I.8}$$

It should also be noted that in the limit $N \to \infty$ ($\epsilon \to 0$),

$$\begin{aligned} \epsilon z_0 \left[-\frac{m}{\epsilon^2}(y_1 - y_0) - V'_{av}(y_0) \right] &\to -z_0 p_0 \ , \\ \epsilon z_N \frac{m}{\epsilon^2}(y_N - y_{N-1}) &\to z_N p_N \ , \end{aligned} \tag{I.9}$$

where $p_0/m = \lim_{\epsilon\to 0}(y_1 - y_0)/\epsilon$ and $p_N/m = \lim_{\epsilon\to 0}(y_N - y_{N-1})/\epsilon$. Changing the integration variables $y_1, \ldots, y_{N-1}$ into $f_1, \ldots, f_{N-1}$, such that

$$f_j = \frac{m}{\epsilon^2}(y_{j+1} - 2y_j + y_{j-1}) + V'_{av}(y_j) \ , \tag{I.10}$$

and explicitly integrating over $f_1, \ldots, f_{N-1}$, then leads to the following approximation:

$$\begin{aligned} C_{AB}(t) \approx \frac{1}{2\pi\hbar} \int dy_0 \int dy_t \int dz_0 \int dz_t \left| \frac{\partial p_0}{\partial y_t} \right| \langle y_0 + z_0/2 | \hat{A} | y_0 - z_0/2 \rangle \\ \langle y_t - z_t/2 | \hat{B} | y_t + z_t/2 \rangle e^{-ip_0 z_0/\hbar} e^{ip_t z_t/\hbar} e^{i\int_0^t d\tau U(\tau)} \ . \end{aligned} \tag{I.11}$$

It should be noted that in arriving to Eq. (I.11), we have explicitly incorporated the limit $N \to \infty$ ($\epsilon \to 0$), such that $y_N \to y_t$, $z_N \to z_t$ and $\epsilon \sum_{j=0}^{N-1} U(y_j) \to \int_0^t d\tau U(\tau)$, and made use of the following identity[115]

$$\lim_{N\to\infty} \frac{1}{\epsilon} \left(\frac{m}{\epsilon^2} \right)^{N-1} \left| \frac{\partial y}{\partial f} \right| = \frac{1}{m} \left| \frac{\partial p_0}{\partial y_t} \right| \tag{I.12}$$

($|\partial y/\partial f|$ is the determinant of the $(N-1)\times(N-1)$ matrix whose (i,j)-th element is $\partial y_i/\partial f_j$). It should also be noted that $y_t = y_t(y_0, p_0)$ in Eq. (I.11) follows a classical trajectory which is dictated by the averaged potential (Cf. Eq. (I.8)) :

$$f_j = \frac{m}{\epsilon^2}(y_{j+1} - 2y_j + y_{j+1}) + V'_{av}(y_j) = 0 \stackrel{N\to\infty}{\longrightarrow} m\frac{d^2}{dt^2} y(t) = -V'_{av}[y(t)] \ . \tag{I.13}$$

Finally, changing the integration variable y_t into p_0, we arrive at the following *direct linearization (DL)* approximation:

$$C_{AB}(t) \approx C^{DL}_{AB}(t) = (2\pi\hbar)^{-1} \int dy_0 \int dp_0 A_W(y_0, p_0) B_W(y_t, p_t) e^{i\int_0^t d\tau U(\tau)/\hbar} \ , \tag{I.14}$$

where

$$A_W(q,p) = \int d\Delta e^{-ip\Delta/\hbar} \langle q + \Delta/2 | \hat{A} | q - \Delta/2 \rangle \tag{I.15}$$

is the Wigner transform, and $y_t = y_t(y_0, p_0)$ and $p_t = p_t(y_0, p_0)$ follow a classical trajectory which is dictated by the averaged potential

The DL approximation in Eq. (I.14) can be straightforwardly extended to the case of a multi-dimensional system:

$$C_{AB}(t) \approx C_{AB}^{DL}(t) = (2\pi\hbar)^{-N_n} \int \mathbf{dQ_0} \int \mathbf{dP_0} A_W(\mathbf{Q_0}, \mathbf{P_0}) B_W(\mathbf{Q_t}, \mathbf{P_t}) e^{i \int_0^t d\tau U(\tau)/\hbar} , \tag{I.16}$$

APPENDIX J

Liouville Space Algebra for the Exact Linear ORF

This appendix derives the expression for the exact linear response function for the shifted harmonic oscillator model, using Liouville space algebra, and will make use of the following identities [81]

$$|m,n\rangle\rangle = |m\rangle\langle n| \tag{J.1}$$

$$\sum_{m,n} |m,n\rangle\rangle\langle\langle m,n| = 1 \tag{J.2}$$

$$|A\rangle\rangle = \sum_{m,n} |m,n\rangle\rangle A_{m,n} = \sum_{m,n} |m,n\rangle\rangle\langle\langle m,n|A\rangle\rangle \tag{J.3}$$

$$\langle\langle A|B\rangle\rangle = Tr\left(A^{\dagger}B\right) \tag{J.4}$$

$$\langle\langle m,n|m',n'\rangle\rangle = \delta_{m,m'}\delta_{n,n'} \tag{J.5}$$

where A and B are Hilbert space operators, and the action of a superoperator $\mathbf{O}$ on a Liouville space ket corresponds to a commutator of the Hilbert space operator

$$\mathbf{O}\,|A\rangle\rangle \leftrightarrow [O,A]\,. \tag{J.6}$$

The linear response may be derived from the following expression

$$\langle\langle\hat{V}|\,\mathbf{G}\,(t_1)\,\mathbf{V}\,|\hat{\rho}_{eq}\rangle\rangle = \sum_{j,k,m,n} \langle\langle\hat{V}|m,n\rangle\rangle\langle\langle m,n|\,\mathbf{G}\,(t_1)\,|j,k\rangle\rangle\langle\langle j,k|\,\mathbf{V}\,|\hat{\rho}_{eq}\rangle\rangle,$$

(J.7)

where the transition dipole operator has the form

$$\hat{V} = \sum_{j \neq k} V_{jk} \left| j \right\rangle \left\langle k \right|, \tag{J.8}$$

and below each of the factors appearing on the right side will be computed separately. Using the fact that $V_{jk}^{*} = V_{kj}$ and $Tr\left(\ldots\right) = \sum_{k} \left\langle k \right| \ldots \left| k \right\rangle$, the first factor is easily found by

$$\begin{aligned} \left\langle \left\langle \hat{V} | m, n \right\rangle \right\rangle &\overset{(J.2)}{=} Tr\left(\hat{V}^{\dagger} \left| m \right\rangle \left\langle n \right| \right) = Tr\left(\sum_{j \neq k} V_{jk}^{*} \left| k \right\rangle \left\langle j | m \right\rangle \left\langle n \right| \right) \\ &= Tr\left(\sum_{k} V_{mk}^{*} \left| k \right\rangle \left\langle n \right| \right) = \sum_{k,l} V_{mk}^{*} \delta_{l,k} \delta_{n,l} = V_{nm} \end{aligned} \tag{J.9}$$

To find the second factor, we assume that the $\{\left| k \right\rangle\}$ are eigenstates of the Hamiltonian H, so that $H \left| k \right\rangle = \varepsilon_{k} \left| k \right\rangle$ and

$$\begin{aligned} \left[H, \left| k \right\rangle \left\langle j \right| \right] &= \left[\sum_{l} \varepsilon_{l} \left| l \right\rangle \left\langle l \right|, \left| j \right\rangle \left\langle k \right| \right] \\ &= \sum_{l} \varepsilon_{l} (\left| l \right\rangle \left\langle k \right| \delta_{l,j} - \left| j \right\rangle \left\langle l \right| \delta_{k,l}) = \hbar \omega_{j,k} \end{aligned} \tag{J.10}$$

where $\omega_{j,k} \equiv \varepsilon_{j} - \varepsilon_{k}$ is the transition frequency. Further, using the definition of the field-free Green's function superoperator, $\mathbf{G}\left(t_{1}\right) = \Theta(t_{1}) \exp\left(-i\mathbf{L}t_{1}\right)$, leads to

$$\begin{aligned} \left\langle \left\langle m, n \right| \mathbf{G}\left(t_{1}\right) \left| j, k \right\rangle \right\rangle &= \left\langle \left\langle m, n \right| \left\{ 1 - \frac{1}{\hbar} i t_{1} \mathbf{L} + \frac{1}{2\hbar^{2}} \left(i t_{1} \right)^{2} \mathbf{L}^{2} + \ldots \right\} \left| j, k \right\rangle \right\rangle \\ &\overset{(J.6)}{=} \left\langle \left\langle m, n \right| \left\{ 1 - i t_{1} \omega_{j,k} + \frac{1}{2} \left(i t_{1} \right)^{2} \omega_{j,k}^{2} + \ldots \right\} \left| j, k \right\rangle \right\rangle \\ &= \exp\left(-i\omega_{j,k} t_{1}\right) \left\langle \left\langle m, n | j, k \right\rangle \right\rangle \overset{(J.5)}{=} \exp\left(-i\omega_{j,k} t_{1}\right) \delta_{m,j} \delta_{n,k}. \end{aligned} \tag{J.11}$$

The first step in computing the last factor is to write the density operator as

$$\left| \hat{\rho}_{eq} \right\rangle \rangle \overset{(J.3)}{=} \sum_{m,n} \left\langle m \right| \frac{e^{-\beta H}}{Z} \left| n \right\rangle \left| m \right\rangle \left\langle n \right| = \sum_{m} \frac{e^{-\beta \varepsilon_{m}}}{Z} \left| m \right\rangle \left\langle m \right|, \tag{J.12}$$

so that

$$\begin{aligned}
\mathbf{V}\left|\hat{\rho}_{eq}\right\rangle\rangle \overset{(J.6)}{\leftrightarrow} \left[\hat{V},\hat{\rho}_{eq}\right] &= \left[\sum_{j'\neq k'} V_{j'k'}\left|j'\right\rangle\left\langle k'\right|, \sum_{m}\frac{e^{-\beta\varepsilon_m}}{Z}\left|m\right\rangle\left\langle m\right|\right] \qquad \text{(J.13)}\\
&= \sum_{j'\neq k',m} V_{j'k'}\frac{e^{-\beta\varepsilon_m}}{Z}\left(\left|j'\right\rangle\left\langle m\right|\delta_{k',m} - \left|m\right\rangle\left\langle k'\right|\delta_{m,j'}\right)\\
&\overset{(J.3)}{=} \sum_{j'\neq m} V_{j'm}\frac{e^{-\beta\varepsilon_m}}{Z}\left|j',m\right\rangle\rangle - \sum_{k'\neq m} V_{mk'}\frac{e^{-\beta\varepsilon_m}}{Z}\left|m,k'\right\rangle\rangle.
\end{aligned}$$

Finally,

$$\begin{aligned}
\langle\langle j,k|\,\mathbf{V}\left|\hat{\rho}_{eq}\right\rangle\rangle &= \sum_{j'\neq m} V_{j'm}\frac{e^{-\beta\varepsilon_m}}{Z}\langle\langle j,k|j',m\rangle\rangle - \sum_{k'\neq m} V_{mk'}\frac{e^{-\beta\varepsilon_m}}{Z}\langle\langle j,k|m,k'\rangle\rangle\\
&\overset{(J.5)}{=} \sum_{j'\neq m} V_{j'm}\frac{e^{-\beta\varepsilon_m}}{Z}\delta_{j,j'}\delta_{k,m} - \sum_{k'\neq m} V_{mk'}\frac{e^{-\beta\varepsilon_m}}{Z}\delta_{j,m}\delta_{k,k'}\\
&= \sum_{m}\frac{e^{-\beta\varepsilon_m}}{Z}\left(V_{jm}\delta_{k,m} - V_{mk}\delta_{j,m}\right) \qquad \text{(J.14)}
\end{aligned}$$

BIBLIOGRAPHY

BIBLIOGRAPHY

[1] A. Assion and T. Baumert and M. Bergt and T. Brixner and B. Kiefer and V. Seyfried and M. Strehle and G. Gerber. Control of chemical reactions by feedback-optimized phase-shaped femtosecond laser pulses. *Science*, 282:5390, 1998.

[2] W.S. Warren and H. Rabitz and M. Dahleh. Coherent control of quantum dynamics: The dream is alive. *Science*, 259:1581, 1992.

[3] R.J. Gordon and S.A. Rice. Active control of the dynamics of atoms and molecules. *Annu. Rev. Phys. Chem.*, 48:601, 1997.

[4] K. Ohmori. Wave-Packet and Coherent Control Dynamics. *Annu. Rev. Phys. Chem.*, 60:487, 2009.

[5] M. Shapiro and P. Brumer. Laser control of product quantum state populations in unimolecular reactions. *J. Chem. Phys.*, 84:4103, 1986.

[6] M. Shapiro, J.W. Hepburn, and P. Brumer. Simplified laser control of unimolecular reactions: simultaneous (ω_1, ω_3) excitation. *Chem. Phys. Lett.*, 149:451, 1986.

[7] D.J. Tannor and R. Kosloff and S.A. Rice. Coherent pulse sequence induced control of selectivity of reactions: exact quantum mechanical calculations. *J. Chem. Phys.*, '85:5805, 1986.

[8] R. Kosloff and S.A. Rice and P. Gaspard and S. Tersigni and D.J. Tannor. Wavepacket dancing: Achieving chemical selectivity by shaping light pulses. *Chem. Phys.*, 139:201, 1989.

[9] T. Baumert and M. Grosser and R. Thalweiser and G. Gerber. Femtosecond time-resolved molecular multiphoton ionization: The Na_2 system. *Phys. Rev. Lett.*, 67:3653, 1991.

[10] E.D. Potter and J.L. Herek and S. Pederson and Q. Liu and A.H. Zewail. Femtosecond laser control of a chemical reaction. *Nature*, 355:66, 1992.

[11] A. Shnitman and I. Sofer and I. Golub and A. Yogev and and M. Shapiro and Z. Chen and P. Brumer. Experimental Observation of Laser Control: Electronic Branching in the Photodissociation of Na_2 . *Phys. Rev. Lett.*, 76:2886, 1996.

[12] L.C. Zhu and V. Kleiman and X.N. Li and S.-P. Lu and K. Trentelman and R.J. Gordon. Coherent laser control of the product distribution obtained in the photoexcitation of HI. *Science*, 270:77, 1995.

[13] R.S. Judson and H. Rabitz. Teaching lasers to control molecules. *Phys. Rev. Lett.*, 68:1500, 1993.

[14] A.P. Peirce and M.A. Dahleh and H. Rabitz. Optimal control of quantum-mechanical systems: Existence, numerical approximation, and applications. *Phys. Rev. A*, 37:4950, 1988.

[15] W. Jakubetz and J. Manz and H.-J. Schreier. Theory of optimal laser pulses for selective transitions between molecular eigenstates. *Chem. Phys. Lett.*, 165:100, 1990.

[16] B.K. Dey. Coherent optimal control of multiphoton molecular excitation. *J. Phys. B: At. Mol. Opt.*, 34:2189, 2001.

[17] D.E. Goldberg. *Genetic algorithms in search, optimization, and machine learning.* Addison-Wesley, Reading, MA, 1989.

[18] S. Shi and A. Woody, and H. Rabitz. Optimal control of selective vibrational excitation in harmonic linear chain molecules. *J. Chem. Phys.*, 88:6870, 1988.

[19] Y.J. Yan and R.E. Gillilan and R.M. Whitnell and K.R. Wilson and S. Mukamel. Optical control of molecular dynamics: Liouville-space theory. *J. Phys. Chem.*, 97:2320, 1993.

[20] J. Cao, C.J. Bardeen, and K.R. Wilson. Molecular π pulses: population inversion with positively chirped short pulses. *J. Chem. Phys.*, 113:1898, 2000.

[21] M.A. Dugan and J.X. Tull and W.S. Warren. High-resolution acousto-optic shaping of unamplified and amplified femtosecond laser pulses. *J. Opt. Soc. Am. B*, 14:2348, 1997.

[22] H. Kawashima and MM. Wefers and K.A. Nelson. Femtosecond pulse shaping, multiple-pulse spectroscopy, and optical control. *Annu. Rev. Phys. Chem.*, 46:627, 1995.

[23] Q. Shi and E. Geva. Stimulated Raman adiabatic passage in the presence of dephasing. *J. Chem. Phys.*, 119:11773, 2003.

[24] E.M. Grumstrup, S.-H. Shim, M.A. Montgomery, N.H. Damrauer, and M.T. Zanni. Facile collection of two-dimensional electronic spectra using femtosecond pulse-shaping technology. *Opt. Exp.*, 15:16681, 2007.

[25] M. Cho. Coherent two-dimensional optical spectroscopy. *Chem. Rev.*, 108:1331, 2008.

[26] J. Zheng, K. Kwak, and M. Fayer. Ultrafast 2D IR vibrational echo spectroscopy. *Acc. Chem. Res.*, 40:75, 2007.

[27] S. Mukamel. Multidimensional femtosecond correlation spectroscopies of electronic and vibrational excitations. *Annu. Rev. Phys. Chem.*, 51:691, 2000.

[28] A. M. Moran, J. Dreyer, and S. Mukamel. Ab initio simulation of the two-dimensional vibrational spectrum of dicarbonylacetylacetonato rhodium(i). *J. Chem. Phys.*, 118:1347, 2003.

[29] S. Mukamel and eds. R.Hochstrasser. Special issue on multidimensional spectroscopies. *Chem. Phys.*, 266:135, 2001.

[30] Y. Tanimura and S. Mukamel. Two?dimensional femtosecond vibrational spectroscopy of liquids. *J. Chem. Phys.*, 99:9496, 1993.

[31] O. Golonzka, M. Khalil, N. Demirdöven, and A. Tokmakoff. Coupling and orientation between anharmonic vibrations characterized with two-dimensional infrared vibrational echo spectroscopy. *J. Chem. Phys.*, 115:10814, 2001.

[32] Special issue on multidimensional spectroscopies. *Chem. Phys.*, 266:135, 2001.

[33] Multidimensional ultrafast spectroscopy special feature. *Proc. Natl. Acad. Sci. USA*, 104: 14189, 2007.

[34] K. A. Merchant, D. E. Thompson, and M. D. Fayer. Two-dimensional time-frequency ultrafast infrared vibrational echo spectroscopy. *Phys. Rev. Lett.*, 86:3899, 2001.

[35] M. T. Zanni, M. C. Asplund, and R. M. Hochstrasser. Two-dimensional heterodyned and stimulated infrared photon echoes of N-methylacetamide-D. *J. Chem. Phys.*, 114:4579, 2001.

[36] F. Ding and and M.T. Zanni P. Mukherjee. Passively correcting phase drift in two-dimensional infrared spectroscopy. *Opt. Lett.*, 31:2918, 2006.

[37] G.D. Goodno, G. Dadusc, and R.J D. Miller. Ultrafast heterodyne-detected transient-grating spectroscopy using diffractive optics. *J. Opt. Soc. Am. B*, 15:1791, 1998.

[38] T. Brixner, T. Mancal, I.V. Stiopkin, and G.R. Fleming. Phase-stabilized two-dimensional electronic spectroscopy. *J. Chem. Phys.*, 121:4221, 2004.

[39] L. Lepetit and M. Joffre. Two-dimensional nonlinear optics using Fourier-transform spectral interferometry. *Opt. Lett.*, 21:564, 1996.

[40] A. Nemeth, F. Milota, J. Sperling, D. Abramavicius, S. Mukamel, and H.F. Kauffmann. Tracing exciton dynamics in molecular nanotubes with 2D electronic spectroscopy. *Chem. Phys. Lett.*, 469:130, 2009.

[41] B.M. Garraway and Kalle-Antti Suominen. Wave-packet dynamics: new physics and chemistry in femto-time. *Rep. Prog. Phys.*, 58:365, 1995.

[42] Q. Shi and E. Geva. A comparison between different semiclassical approximations for optical response functions in nonpolar liquid solution II.: The signature of excited state dynamics on two-dimensional spectra. *J. Chem. Phys.*, 129:124505, 2008.

[43] J. Somlói and A. Lörincz. Two-electron-state molecule in strong electric fields. *Phys. Rev. A*, 43:2397, 1991.

[44] C.J. Bardeen, Q. Wang, and C.V. Shank. Femtosecond chirped pulse excitation of vibrational wave packets in LD690 and bacteriorhodopsin. *J. Phys. Chem. A*, 102:2759, 1998.

[45] G. Cerullo, C.J. Bardeen, Q. Wang, and C.V. Shank. High-power femtosecond chirped pulse excitation of molecules in solution. *Chem. Phys. Lett.*, 262:362, 1996.

[46] V.S. Malinovsky and J.L. Krause. Efficiency and robustness of coherent population transfer with intense, chirped laser pulses. *Phys. Rev. A*, 63:043415–1, 2001.

[47] O. Nahmias, O. Bismuth, O. Shoshana, and S. Ruhman. Tracking excited state dynamics with coherent control: automated limiting of population transfer in LDS750. *J. Phys. Chem. A*, 109:8246, 2005.

[48] A.C. Florean, E.C. Carroll, K.G. Spears, R.J. Sension, and P.H. Bucksbaum. Optical control of excited-state vibrational coherences of a molecule in solution: the influence of the excitation pulse spectrum and phase in LD690. *J. Phys. Chem. B*, 110:20023, 2006.

[49] S. Ruhman and R. Kosloff. Application of chirped ultrashort pulses for generating large-amplitude ground-state vibrational coherence: a computer simulation. *J. Opt. Soc. Am. B*, 7:1748, 1990.

[50] C.J. Bardeen and Q. Wang and C.V. Shank. Selective excitation of vibrational wave packet motion using chirped pulses. *Phys. Rev. Lett.*, 75:3410, 1995.

[51] B.D. Fainberg. Nonperturbative analytic approach to the interaction of intense ultrashort chirped pulses with molecules in solution: Picture of "moving" potentials. *J. Chem. Phys.*, 109:4523, 1998.

[52] K. Mishima and M. Hayashi and J.T. Lin and K. Yamashita and S.H. Lin. A numerical study on vibronic and vibrational dynamics generated by chirped laser pulses in the presence of relaxation processes. *Chem. Phys. Lett.*, 309:279, 1999.

[53] B.D. Fainberg and V.A. Gorbunov. Coherent population transfer in molecules coupled with a dissipative environment by an intense ultrashort chirped pulse. *J. Chem. Phys.*, 117:7222, 2002.

[54] M.Demirplak and S.A. Rice. Optical control of molecular dynamics in a liquid. *J. Chem. Phys.*, 116:8028, 2002.

[55] R. Kosloff. Time-dependent quantum-mechanical methods for molecular dynamics. *J. Phys. Chem.*, 92:2087, 1988.

[56] D. Gottlieb and S.A. Orszag. *Numerical analysis of spectral methods: Theory and applications*. SIAM, Philadelphia, USA, 1977.

[57] E.T. Whittaker. On the functions which are represented by the expansions of the interpolation theory. *Proc. R. Soc. Edinburgh*, 35:181, 1915.

[58] H. Nyquist. Certain topics in telegraph transmission theory. *Trans. AIEE*, 47:617, 1928.

[59] C.E. Shannon. A mathematical theory of communication. *Proc. IRE*, 37:10, 1949.

[60] J.W. Cooley and J.W. Tukey. An algorithm for the machine calculation of complex Fourier series. *Math. Comput.*, 19:287, 1965.

[61] C.J. Temperton. Self-sorting mixed-radix fast Fourier transforms. *J. Comput. Phys.*, 52:1, 1983.

[62] H.J. Nussbaumer. *Fast Fourier transform and convolution algorithms*. Springer Verlag, Berlin, Germany, 1982.

[63] K.F. Everitt and J.L. Skinner. Molecular theory of three-pulse photon echoes for solutes in non-polar fluids. *Chem. Phys.*, 266:197, 2001.

[64] R. Kubo. *Fluctuation, relaxation and resonance in magnetic systems*. Oliver and Boyd, London, UK, 1962.

[65] G.E. Uhlenbeck and L.S. Ornstein. On the theory of the Brownian motion. *Phys. Rev.*, 36: 823, 1930.

[66] J. Luczka. Non-Markovian stochastic processes: Colored noise. *Chaos*, 15:026107, 2005.

[67] R.F. Fox and I.R. Gatland and R. Roy and G. Vemuri. Fast, accurate algorithm for numerical simulation of exponentially correlated noise. *Phys. Rev. A*, 38:5938, 1998.

[68] L. Bartosch. Generation of colored noise. *Int. J. Mod. Phys. C*, 12:851, 2001.

[69] J.L. Doob. *Stochastic Processes*. Wiley, New York, 1953.

[70] M. Rigo and F. Mota-Furtado and P.F. O'Mahony. Continuous stochastic Schrödinger equations and localization. *J. Phys. A: Math. Gen.*, 30:7557, 1997.

[71] D.E. Makarov and H. Metiu. Quantum dynamics with dissipation: A treatment of dephasing in the stochastic Schrödinger equation. *J. Chem. Phys.*, 111:10126, 1999.

[72] W.T. Strunz. The Brownian motion stochastic Schrödinger equation. *Chem. Phys.*, 268:237, 2001.

[73] J.S. Melinger, S.R. Gandhi, A. Hariharan, D. Goswami, and W.S. Warren. Adiabatic population transfer with frequency-swept laser pulses. *J. Chem. Phys.*, 101:6439, 1994.

[74] M. Shapiro and P. Brumer. The equivalence of unimolecular decay product yields in pulsed and cw laser excitation. *J. Chem. Phys.*, 84:540, 1986.

[75] K. Misawa and T. Kobayashi. Wave-packet dynamics in a cyanine dye molecule excited with femtosecond chirped pulses. *J. Chem. Phys.*, 113:7546, 2000.

[76] B. Amstrup and A. Lörincz and S.A. Rice. Population inversion in a multilevel system: a model study. *J. Phys. Chem.*, 97:6175, 1993.

[77] H.M. Sevian and J.L. Skinner. A molecular theory of inhomogeneous broadening, including the correlation between different transitions, in liquids and glasses. *Theor. Chem. Acc.*, 82: 29, 1992.

[78] J.R. Schmidt and N. Sundlass and J.L. Skinner. Line shapes and photon echoes within a generalized Kubo model. *Chem. Phys. Lett.*, 378:559, 2003.

[79] C.J. Bardeen and C.V. Shank. Ultrafast dynamics of the solvent-solute interaction measured by femtosecond four-wave mixing: LD690 in n- alcohols. *Chem. Phys. Lett.*, 226:310, 1994.

[80] T. Fonseca, B.M. Ladanyi. Breakdown of linear response for solvation dynamics in methanol. *J. Phys. Chem.*, 95:2116, 1991.

[81] S. Mukamel. *Principles of Nonlinear Optical Spectroscopy.* Oxford University Press, New York, 1995.

[82] J.G. Saven and J.L. Skinner. A molecular theory of the line shape: Inhomogeneous and homogeneous electronic spectra of dilute chromophores in nonpolar fluids. *J. Chem. Phys.*, 99:4391, 1993.

[83] R. Kubo. A Stochastic Theory of Line Shape. *Adv. Chem. Phys.*, 15:101, 1969.

[84] S. Mukamel. *Principles of Nonlinear Optical Spectroscopy.* Oxford, New York, 1995.

[85] D. M. Jonas. Two-dimensional femtosecond spectroscopy. *Annu. Rev. Phys. Chem.*, 54:425, 2003.

[86] M. Khalil, N. Demirodoven, and A. Tokmakoff. Coherent 2D IR spectroscopy: Molecular structure and dynamics in solution. *J. Phys. Chem. A*, 107:5258, 2003.

[87] S. Mukamel. On the semiclassical calculation of molecular absorption and fluorescence spectra. *J. Chem. Phys.*, 77:173, 1982.

[88] N. E. Shemetulskis and R. F. Loring. Semiclassical theory of the photon echo: Application to polar fluids. *J. Chem. Phys.*, 97:1217, 1992.

[89] J. G. Saven and J. L. Skinner. A molecular theory of the line shape: Inhomogeneous and homogeneous electronic spectra of dilute chromophores in nonpolar fluids. *J. Chem. Phys.*, 99(6):4391, 1993.

[90] M. D. Stephens, J. G. Saven, and J. L. Skinner. Molecular theory of electronic spectroscopy in nonpolar fluids: Ultrafast solvation dynamics and absorption and emission line shapes. *J. Chem. Phys.*, 106:2129, 1997.

[91] Q. Shi and E. Geva. A comparison between different semiclassical approximations for optical response functions in nonpolar liquid solutions. *J. Chem. Phys.*, 122:064506, 2005.

[92] B. J. Ka and E. Geva. A nonperturbative calculation of nonlinear spectroscopic signals in liquid solution. *J. Chem. Phys.*, 125:214501, 2006.

[93] W. H. Miller. Including quantum effects in the dynamics of complex (i.e. large) molecular systems. *J. Chem. Phys.*, 125:132305, 2006.

[94] Q. Shi and E. Geva. A relationship between semiclassical and centroid correlation functions. *J. Chem. Phys.*, 118:8173, 2003.

[95] Q. Shi and E. Geva. A semiclassical theory of vibrational energy relaxation in the condensed phase. *J. Phys. Chem. A*, 107:9059, 2003.

[96] Q. Shi and E. Geva. Vibrational energy relaxation in liquid oxygen from a semiclassical molecular dynamics simulation. *J. Phys. Chem. A*, 107:9070, 2003.

[97] Q. Shi and E. Geva. Nonradiative electronic relaxation rate constants from approximations based on linearizing the path-integral forward-backward action. *J. Phys. Chem. A*, 108:6109, 2004.

[98] K. Thompson and N. Makri. Influence functionals with semiclassical propagators in combined forward-backward time. *J. Chem. Phys.*, 110:1343, 1999.

[99] O. Kühn and N. Makri. Forward-backward semiclassical calculation of spectral line shapes: I_2 in a rare gas cluster. *J. Phys. Chem. A*, 103:9487, 1999.

[100] X. Sun and W. H. Miller. Forward-backward initial value representation for semiclassical time correlation functions. *J. Chem. Phys.*, 110:6635, 1999.

[101] M. A. Sepúlveda and S. Mukamel. Semiclassical theory of molecular nonlinear optical polarization. *J. Chem. Phys.*, 102:9327, 1995.

[102] C. F. Spencer and R. F. Loring. Dephasing of a solvated two-level system: A semiclassical approach for parallel computing. *J. Chem. Phys.*, 105:6596, 1996.

[103] M. Ovchinnikov, V. A. Apkarian, and G. A. Voth. Semiclassical molecular dynamics computation of spontaneous light emission in the condensed phase: Resonance Raman spectra. *J. Chem. Phys.*, 184:7130, 2001.

[104] J. R. Schmidt, S. A. Corcelli, and J. L. Skinner. Pronounced non-Condon effects in the ultrafast infrared spectroscopy of water. *J. Chem. Phys.*, 123:044513, 2005.

[105] M. Khalil, N. Demirodoven, and A. Tokmakoff. Obtaining absorptive line shapes in two-dimensional infrared vibrational correlation spectra. *J. Phys. Chem. A*, 107:5258, 2003.

[106] M. F. Herman and E. Kluk. A semiclassical justification for the use of non-spreading wave packets in dynamics calculations. *Chem. Phys.*, 91:27, 1984.

[107] E. Kluk, M. F. Herman, and H. L. Davis. Comparison of the propagation of semiclassical frozen gaussian wave functions with quantum propagation for a highly excited anharmonic oscillator. *J. Chem. Phys.*, 84:326, 1986.

[108] A. R. Walton and D. E. Manolopoulos. A new semiclassical initial value method for Franck-Condon spectra. *Mol. Phys.*, 87:961, 1996.

[109] M. L. Brewer, J. S. Hulme, and D. E. Manolopoulos. Semiclassical dynamics in up to 15 coupled vibrational degrees of freedom. *J. Chem. Phys.*, 106:4832, 1997.

[110] H. Wang, X. Sun, and W. H. Miller. Semiclassical approximations for the calculation of thermal rate constants for chemical reactions in complex molecular systems. *J. Chem. Phys.*, 108:9726, 1998.

[111] X. Sun, H. Wang, and W. H. Miller. On the semiclassical description of quantum coherence in thermal rate constants. *J. Chem. Phys.*, 109:4190, 1998.

[112] J. S. Shao and N. Makri. Forward-backward semiclassical dynamics without prefactors. *J. Phys. Chem. A*, 103:7753, 1999.

[113] K. G. Kay. Numerical study of semiclassical initial value methods for dynamics. *J. Chem. Phys.*, 100:4432, 1994.

[114] Yl Elran and K. G. Kay. Semiclassical ivr treatment of reactive collisions. *J. Chem. Phys.*, 116:10577, 2002.

[115] L. S. Schulman. *Techniques and applications of path integration*. Wiley, New York, 1981.

[116] J. A. Poulsen, G Nyman, and P. J. Rossky. Practical evaluation of condensed phase quantum correlation functions: A Feynman-Kleinert variational linearized path integral method. *J. Chem. Phys.*, 119:12179, 2003.

[117] Q. Shi and E. Geva. A semiclassical generalized quantum master equation for an arbitrary system-bath coupling. *J. Chem. Phys.*, 120:10647, 2004.

[118] B. J. Ka, Q. Shi, and E. Geva. Vibrational energy relaxation rates via the linearized semiclassical approximations: Applications to neat diatomic liquids and atomic-diatomic liquid mixtures. *J. Phys. Chem. A*, 109:5527, 2005.

[119] B. J. Ka and E. Geva. Vibrational energy relaxation of polyatomic molecules in liquid solution via the linearized semiclassical method. *J. Phys. Chem. A*, 110:9555, 2006.

[120] B. D. Bursulaya and H. J. Kim. Effects of solute electronic structure variation on photon echo spectroscopy. *J. Phys. Chem.*, 100:16451, 1996.

[121] E. Pollak and J. Liao. A new quantum transition state theory. *J. Chem. Phys.*, 108:2733, 1998.

[122] X. Sun and W. H. Miller. Mixed semiclassical-classical approaches to the dynamics of complex molecular systems. *J. Chem. Phys.*, 106:916, 1997.

[123] X. Sun, H. Wang, and W. H. Miller. Semiclassical theory of electronically nonadiabatic dynamics: Results of a linearized approximation to the initial value representation. *J. Chem. Phys.*, 109:7064, 1998.

[124] H. Wang, X. Song, D. Chandler, and W. H. Miller. Semiclassical study of electronically nonadiabatic dynamics in the condensed phase: Spin-boson problem with debye spectral density. *J. Chem. Phys.*, 110:4828, 1999.

[125] W. H. Miller. Generalization of the linearized approximation to the semiclassical initial value representation for reactive flux correlation functions. *J. Phys. Chem. A*, 103:9384, 1999.

[126] J. S. Shao, J. L. Liao, and E. Pollak. Quantum transition state theory: Perturbation expansion. *J. Chem. Phys.*, 108:9711, 1998.

[127] J. L. Liao and E. Pollak. Quantum transition state theory for dissipative systems. *Chem. Phys.*, 268:295, 2001.

[128] E. Wigner. On the quantum correction for thermodynamic equilibrium. *Phys. Rev.*, 40:749, 1932.

[129] C. Schütte. Partial Wigner transforms and the quantum-classical Liouville equation. *Konard-Zuse-Zentrum für informationstechnik Berlin*, pages Preprint SC 99–10, June 1999.

[130] S. A. Pentidis and R. F. Loring. Calculation of the photon echo with mixed-state propagation. *Chem. Phys. Lett.*, 287:217, 1998.

[131] S. A. Egorov, E. Rabani, and B. J. Berne. Vibronic spectra in condensed matter: A comparison of exact quantum mechanical and various semiclassical treatments for harmonic baths. *J. Chem. Phys.*, 108:1407, 1998.

[132] G. Hanna and E. Geva. Multi-dimensional spectra via the mixed quantum-classical Liouville method: Signatures of nonequilibrium dynamics. *J. Phys. Chem. B*, submitted.

[133] A. Donoso and C. C. Martens. Semiclassical multistate Liouville dynamics in the adiabatic representation. *J. Chem. Phys.*, 112:3980, 2000.

[134] M. Santer, U. Manthe, and G. Stock. Quantum-classical Liouville description of multidimensional nonadiabatic molecular dynamics. *J. Chem. Phys.*, 114:2001, 2001.

[135] R. Kapral and G. Ciccotti. Mixed quantum classical dynamics. *J. Chem. Phys.*, 110:8919, 1999.

[136] S. Nielsen, R. Kapral, and G. Ciccotti. Mixed quantum classical surface hopping dynamics. *J. Chem. Phys.*, 112:6543, 2000.

[137] C. Wan and J. Schofield. Mixed quantum-classical molecular dynamics: Aspects of multithreads algorithms. *J. Chem. Phys.*, 113:7047, 2000.

[138] C. Wan and J. Schofield. Exact and asymptotic solutions of the mixed quantum-classical Liouville equation. *J. Chem. Phys.*, 112:4447, 2000.

[139] R. Kapral. Progress in the theory of mixed-quantum classical dynamics. *Annu. Rev. Phys. Chem.*, 57:129, 2006.

[140] S. Tretiak, W.M. Zhang, V. Chernyak, and S. Mukamel. Excitonic couplings and electronic coherence in bridged naphthalene dimers. *Proc. Natl. Acad. Sci. USA*, 96:13003, 1999.

[141] S. Tretiak, C. Middleton, V. Chernyak, and S. Mukamel. Exciton Hamiltonian for the bacteriochlorophyll system in the LH2 antenna complex of purple bacteria. *J. Phys. Chem. B*, 104:4519, 2000.

[142] C.R. Baiz, P.L. McRobbie, N.K. Preketes, K.J. Kubarych, and E. Geva. Two-dimensional infrared spectroscopy of dimanganese decacarbonyl and its photoproducts: An ab-inito study. *J. Phys. Chem. A*, 113:9617, 2009.

[143] J. Sung and R. J. Silbey. Four-wave mixing spectroscopy for a multi-level system. *J. Chem. Phys.*, 115:9266, 2001.

[144] A. Tokmakoff. Orientational correlation functions and polarization selectivity for nonlinear spectroscopy of isotropic media. I Third order. *J. Chem. Phys.*, 105:1, 1996.

[145] R. M. Hochstrasser. Two-dimensional IR spectroscopy: polarization anisotropy effects. *Chem. Phys.*, 266:273, 2001.

[146] K. Heyne, N. Huse, J. Dreyer, E. T. J. Nibbering, T. Elsaesser, and S. Mukamel. Coherent low-frequency motions of hydrogen bonded acetic acid dimers in the liquid phase. *J. Chem. Phys.*, 121:902, 2004.

[147] T. Hayashi and S. Mukamel. Multidimensional infrared signatures of intramolecular hydrogen bonding in Malonaldehyde. *J. Phys. Chem. A*, 107:9113, 2003.

[148] T. Hayashi, W. Zhuang, and S. Mukamel. Electrostatic DFT map for the complete vibrational Amide band of NMA. *J. Phys. Chem. A*, 109:9747, 2005.

[149] J. Dreyer. Density functional theory simulations of two-dimensional infrared spectra for hydrogen-bonded acetic acid dimers. *J. Quantum Chem.*, 104:782, 2005.

[150] K. Park, M. Cho, S. Hahn, and D. Kim. Two-dimensional vibrational spectroscopy. II. Ab initio calculation of the coherent 2D infrared response function of $CHCl_3$ and comparison with the 2D Raman response function. *J. Chem. Phys.*, 111:4131, 1999.

[151] t. Ab initio-based all-mode two-dimensional infrared spectroscopy of a sugar molecule. *J. Phys. Chem. B*, 111:9193, 2007.

[152] O. Golonzka and A. Tokmakoff. Polarization-selective third-order spectroscopy of coupled vibronic states. *J. Chem. Phys.*, 115:297, 2001.

[153] G. Arfken. *Mathematical Methods for Physicists*. Academic-Press, 1985. Chapter 17.

[154] A. D. Becke. Density-functional thermochemistry. III. The role of exact exchange. *J. Chem. Phys.*, 98:5648, 1993.

[155] C. Lee, W. Yang, and R. G. Parr. Development of the Colle-Salvetti correlation-energy formula into a functional of the electron density. *Phys. Rev. B*, 37:785, 1988.

[156] B. Miehlich, A. Savin, H. Stoll, and H. Preuss. Results obtained with the correlation energy density functionals of becke and lee, yang and parr. *Chem. Phys. Lett.*, 157:200, 1989.

[157] R. H. Hertwig and W. Koch. On the parameterization of the local correlation functional. What is Becke-3-LYP? *Chem. Phys. Lett.*, 268:345, 1997.

[158] P. Jeffrey Hay and Willard R. Wadt. Ab initio effective core potentials for molecular calculations. potentials for the transition metal atoms sc to hg. *J. Chem. Phys.*, 82(1):270–283, 1985. doi: 10.1063/1.448799. URL `http://link.aip.org/link/?JCP/82/270/1`.

[159] Willard R. Wadt and P. Jeffrey Hay. Ab initio effective core potentials for molecular calculations. potentials for main group elements na to bi. *J. Chem. Phys.*, 82(1):284–298, 1985. doi: 10.1063/1.448800. URL `http://link.aip.org/link/?JCP/82/284/1`.

[160] P. Jeffrey Hay and Willard R. Wadt. Ab initio effective core potentials for molecular calculations. potentials for k to au including the outermost core orbitals. *J. Chem. Phys.*, 82(1): 299–310, 1985. doi: 10.1063/1.448975. URL `http://link.aip.org/link/?JCP/82/299/1`.

[161] Yihan Shao et al. *Phys. Chem. Chem. Phys.*, 8:3172–1391, 2006.

[162] W. Schneider and W. Thiel. Anharmonic force fields from analytic second derivatives: Method and application to methyl bromide. *Chem. Phys. Lett.*, 157:367, 1989.

[163] S. Dressler and W. Thiel. Anharmonic force fields from density functional theory. *Chem. Phys. Lett.*, 273:71, 1997.

[164] C. Lin, A. Gilbert, and P. Gill. Calculating molecular vibrational spectra beyond the harmonic approximation. *Theor. chim. Acta*, 120:23, 2008.

[165] M. Hillery, R. F. O'Connell, M. O. Scully, and E. P. Wigner. Distribution functions in physics: Fundamentals. *Phys. Rep.*, 106(3):121, 1984.